T2R2 東京科学大学 リサーチリポジトリ
Science Tokyo Research Repository

論文 / 著書情報
Article / Book Information

題目(和文)	
Title(English)	A Study of Low-Speed High-Torque Swirling Actuators Driven by Electromagnetic Radial Force with Integrated Speed Reducers
著者(和文)	陳 凌宇
Author(English)	Lingyu Chen
出典(和文)	学位:博士(工学), 学位授与機関:東京工業大学, 報告番号:甲第12367号, 授与年月日:2023年3月26日, 学位の種別:課程博士, 審査員:千葉 明,藤田 英明,萩原 誠,竹内 希,清田 恭平,河邊 賢一,小坂 卓
Citation(English)	Degree:Doctor (Engineering), Conferring organization: Tokyo Institute of Technology, Report number:甲第12367号, Conferred date:2023/3/26, Degree Type:Course doctor, Examiner:,,,,,,
学位種別(和文)	博士論文
Type(English)	Doctoral Thesis

Powered by T2R2 (Science Tokyo Research Repository)

A Study of Low-Speed High-Torque Swirling Actuators Driven by Electromagnetic Radial Force with Integrated Speed Reducers

A DISSERTATION SUBMITTED TO THE DEPARTMENT
OF ELECTRICAL AND ELECTRONIC ENGINEERING
AND THE COMMITTEE ON GRADUATE STUDIES OF
TOKYO INSTITUTE OF TECHNOLOGY IN PARTIAL
FULFILLMENT OF THE REQUIREMENTS FOR THE
DEGREE OF DOCTOR OF ENGINEERING

Supervisor: Professor Akira Chiba

By
Lingyu Chen

December 2022

Abstract

Low-speed high-torque electric machines are widely used in turbines, traction motors, robotic applications, etc. This thesis proposes a novel low-speed high-torque swirling actuator. It generates the electromagnetic radial force in the electromagnetic part, which causes a circular motion with a small radius. Involute-type mechanical gears are integrated to convert the circular motion to low-speed rotation and output the mechanical torque. The transmission ratio is essentially high with the principle similar to cycloidal drives. The developed swirling actuator has a 12-slot inner stator, a 12-pole swirler with surface-mounted permanent magnets and an outer rotor. The electromagnetic radial force and torque are verified by analytical, 3-D finite element analysis and experiments. The first prototype achieves a peak torque density of 27 Nm/L with a small volume of 0.16 L. After enhancing the electromagnetic radial force and redesigning the gears, the peak torque density of the swirling actuator is improved to 64 Nm/L.

Acknowledgments

First, I want to thank Prof. Akira Chiba, who is my supervisor in Tokyo Institute of Technology, for the continuous guidance in the research and the financial support. I also want to thank Prof. Yusuke Fujii, who is the Assistant Professor in Chiba Laboratory, for the advice about the research and the great help in experiments.

In Chiba Laboratory, I have met many kind members. Mr. Hoshi was my tutor and also the first member in the project of swirling actuators. My work is on the base of his contribution. Mr. Thabuis worked together with me in this project during February to August, 2018. His knowledge and experience in mechanical engineering helped me a lot. Mr. Qiu helped me greatly in experiments. Mr. Noguchi often discussed with me in patience and helped me in Japanese. Besides them, I am also grateful for all other lab members. The life in the lab was always interesting.

I also want to thank my parents and friends who keep supporting me mentally, especially during the tough period of the COVID-19 pandemic.

Last but not the least, I want to thank China Scholarship Council for giving me the chance to study in Japan and providing the financial support for three years.

Contents

Abstract ii

Acknowledgments iv

List of Tables ix

List of Figures xiii

1 Introduction 1

1.1 Applications of Low-Speed High-Torque Electric Machines 1

1.2 Types of Low-Speed High-Torque Electric Machines 3

1.2.1 Combination of Electric Machines and Speed Reducers 3

1.2.2 Direct-Drive Machines 10

1.2.3 Magnetic-Geared Machine 11

1.3 Contribution of this Work 12

1.4 Research Objectives 14

1.5 Thesis Organization 15

2 Literature Review 17

2.1 Introduction 17

2.2 Direct-Drive Electric Machines 17

2.2.1 Direct-Drive Servo Motors 17

2.2.2 PM Vernier Machines 18

2.2.3 Other Direct-Drive Electric Machines 20

2.3 Magnetic Gears and Magnetic-Geared Machines 21

2.3.1 Coaxial Magnetic Gears 21
2.3.2 Magnetic-Geared Machines 22
2.3.3 Cycloidal Magnetic Gears 23
2.4 Mechanical-Geared Machines 25
2.5 Comparison of Low-Speed High-Torque Electric Machines 27
2.6 Summary 28

3 Principle and Analysis of Swirling Actuator 29

3.1 Introduction 29
3.2 Basic Structure and Operating Principle 29
3.3 Design of Electromagnetic Part 33
3.3.1 MMF Vector Diagram 34
3.3.2 Design of 12-slot Non-Overlapping Double-Layer Windings 37
3.4 Analysis of Electromagnetic Radial Force 39
3.4.1 Derivation of Air-gap Flux Density 39
3.4.2 Derivation of Radial Force 41
3.4.3 Derivation of Back EMF 43
3.4.4 FEA Results 45
3.5 Experiments of Preliminary Prototype 48
3.5.1 Radial Force Measurement 48
3.5.2 Torque Measurement 52
3.5.3 System Efficiency Evaluation 56
3.5.4 Gear Efficiency Evaluation 59
3.6 Summary 60

4 Torque Density Improvement of Swirling Actuator 61

4.1 Introduction 61
4.2 Radial Force Enhancement 61
4.2.1 Swirler Dimension Optimization 61
4.2.2 FEA Results 63
4.3 Investigation of Gear Design 65

4.3.1 Effect of Pressure Angle 65
4.3.2 Gear Center Distance 66
4.3.3 New Gear Design 68
4.3.4 Analysis of Gear Efficiency 70
4.3.5 Mechanical Stress Analysis of Gears 73
4.4 Experiments of Improved Prototypes 74
4.4.1 Considerations of Mechanical Design 74
4.4.2 Torque Evaluation 77
4.4.3 Loss and Thermal Evaluations 80
4.5 Summary 81

5 Conclusion **83**

References **85**

List of Publications **97**

List of Tables

1.1 Parameters of actuators in MOTOMAN-HC10DTP industrial robot. 3
1.2 Parameters of a PM motor from Maxon. 4
1.3 Parameters of the combination of a PM motor and a gear from Maxon. . . 4

2.1 Parameters of direct-drive servo motors from Yaskawa. 18
2.2 Parameters of actuators in SGM7P series with planetary gears. 26
2.3 Parameters of actuators in FLA series with strain wave gears. 26
2.4 Parameters of actuators in AF series with cycloidal drives. 27

3.1 Specifications of the swirling actuator. 45
3.2 Parameters related to actuator control. 50
3.3 System efficiency and power. 57
3.4 Performance of the prototype at typical operation points. 60

4.1 Specifications of prototypes. 74
4.2 Powers and Losses at Rated Current Density ($i_d = 1$ A, $i_q = 1.5$ A). 80
4.3 Measured temperatures of windings and PMs. 81

List of Figures

1.1 A six-axis industrial robot. Six low-speed high-torque actuators at the joints are indicated by the red arrows. 2

1.2 Spur gears. (a) Two external gears. (b) An external gear and an internal gear. 5

1.3 Structure of the planetary gear. 6

1.4 Structure of the strain wave gear. Gear teeth are simplified into circles. . . 8

1.5 Structure of the coaxial magnetic gear. 9

1.6 Typical structure of magnetic-geared machines. 11

1.7 Basic structure of the homopolar-type swirling actuator [23]. 13

1.8 Comparison between (a) cycloidal drive and (b) swirling actuator. 14

2.1 Structure of the cycloidal magnetic gear. 24

2.2 Torque densities with volumes of low-speed high-torque electric machines. . 28

3.1 Basic structure of the swirling actuator and schematic of the radial force and torque generation. 30

3.2 Operation of the swirling actuator. 31

3.3 MMF of a single coil of a set of non-overlapping windings. 34

3.4 MMF vector of the n^{th} spatial harmonic from a single coil. 35

3.5 MMF vector diagram of the n^{th} spatial harmonic with three-phase AC currents. (a) Positive sequence; (b) negative sequence. 36

3.6 MMF vector diagram of the 5^{th} spatial harmonic generated by the currents. 37

3.7 MMF vector diagram of the 7^{th} spatial harmonic generated by the currents. 38

3.8 Equivalent magnetic circuit of the PM flux with zero currents. 44

3.9 (a) FEA results of $B_{rm}(\theta_s)$ and $B_{ri}(\theta_s)$. (b) Harmonic spectrum of $B_{rm}(\theta_s)$. (c) Harmonic spectrum of $B_{ri}(\theta_s)$. 46
3.10 FEA and analytical results of the radial force components with respect to time. 47
3.11 FEA and analytical results of the radial force components with respect to the initial current phase shift θ_i. 48
3.12 (a) Swirler and rotor. (b) Complete prototype. 49
3.13 Schematic of the static radial force measurement. 49
3.14 Control block diagram for the force measurement. 50
3.15 Measured results of (a) x- and y-axis currents i_x and i_y; (b) x-axis displacement x, y-axis displacement y, and radius r of swirler displacement. 51
3.16 Comparison of analytical, measured and FEA results of the y-axis force F_{yi} with respect to the y-axis current i_y. 52
3.17 (a) Bottom view of the prototype; (b) cross-sectional views of A-A'; (c) pin configuration. 53
3.18 Test bench of the torque measurement. 53
3.19 Control block diagram for the torque measurement. 54
3.20 Measured results of (a) x-axis displacements x, y-axis displacement y and radius r of the circular motion; (b) eccentric direction angle θ_d; (c) phase currents i_u, i_v and i_w; (d) d- and q-axis currents i_d and i_q. The references $i_d^* = 1$ A and $i_q^* = 1$ A. 55
3.21 Measured torque in the plane of d- and q-axis currents i_d and i_q. 56
3.22 Measured and calculated system efficiency. 57
3.23 Gear efficiency η_g in the plane of d- and q-axis currents i_d and i_q. 58
3.24 Swirler center loci at points (a), (b) and (c). 59

4.1 Waveforms for analytical calculation of the radial air-gap flux density. . . . 62
4.2 Analytical results of the active radial force F_a with respect to the nominal air-gap length g_0 and PM thickness t_m. 63
4.3 FEA and calculated results of radial force components with respect to the q-axis current i_q. 64

4.4 Gear sets with different pressure angles α. (a) $\alpha = 42°$, (b) $\alpha = 20°$. 66
4.5 Schematic for calculating the gear center distance. 67
4.6 Gear design candidates. 69
4.7 Tooth interference conditions of Gear 0, Gear 1 and Gear 2. 69
4.8 Forces on the swirler and velocities of the swirler and rotor. 70
4.9 Calculated torque with respect to the transmission ratio G. 71
4.10 Calculated torques with respect to r; (b) calculated gear efficiencies η_g and meshing position angle β with respect to r. 72
4.11 Contour plots of the von Mises stresses on (a) Gear 1 and (b) Gear 2. . . . 73
4.12 Pictures of fabricated gears of (a) Prototype 1; (b) Prototype 2; (c) Prototype 3. 75
4.13 Front sectional view of the prototypes. 75
4.14 (a) Top view of the prototypes; (b) the ideal pin configuration ($r = r_0$); (c) the actual pin configuration ($r < r_0$). 77
4.15 (a) Calculated and measured torques and (b) eccentric radius r with respect to the d-axis current i_d. The q-axis current i_q is 1.5 A and the rotor speed is 5 r/min. 78
4.16 Current operation points at the rotor speed of 5 r/min. 78
4.17 (a) Calculated and measured torques and (b) measured eccentric radius r with respect to the q-axis current i_q. The rotor speed is 5 r/min. 79
4.18 FEA results of the irreversible demagnetization ratio of the PM at 40 A/mm^2. 81

Chapter 1

Introduction

1.1 Applications of Low-Speed High-Torque Electric Machines

Electric machines have been widely used in various of industrial applications in the past several decades. It was estimated that electric machines consume over half of the total generated electric power in a typical industrialized economy, and the proportion becomes about 2/3 in the industrial sector in 2008 [1]. Recently, with the increasing concerns about global warming and environmental protection, there has been a trend for transportation electrification worldwide. Electric vehicles (EVs) and even electric air-crafts have been developed rapidly [2]. Moreover, to raise the production efficiency, industrial robots have also received great interest from manufacturers. These are two typical fields where electric machines play an essential role in the driving systems.

There are many applications that require low-speed high-torque electric machines. In a wind turbine, the low-speed generator can have the high power of 10 MW and high torque of 11.9 MNm, whereas the rotational speed of the turbine is only from 6 r/min to 9.6 r/min [3]. In [4], the traction motor for directly driving the vehicle wheels has a low base speed of 300 r/min and a high rated torque of 2500 Nm. In industrial robots, low-speed high-torque actuators are equipped at the joints. Fig. 1.1 shows a six-axis industrial robot picking items. The photo is taken by the author in the international robot exhibition in Tokyo, 2019. Six low-speed high-torque actuators are indicated by red arrows. This

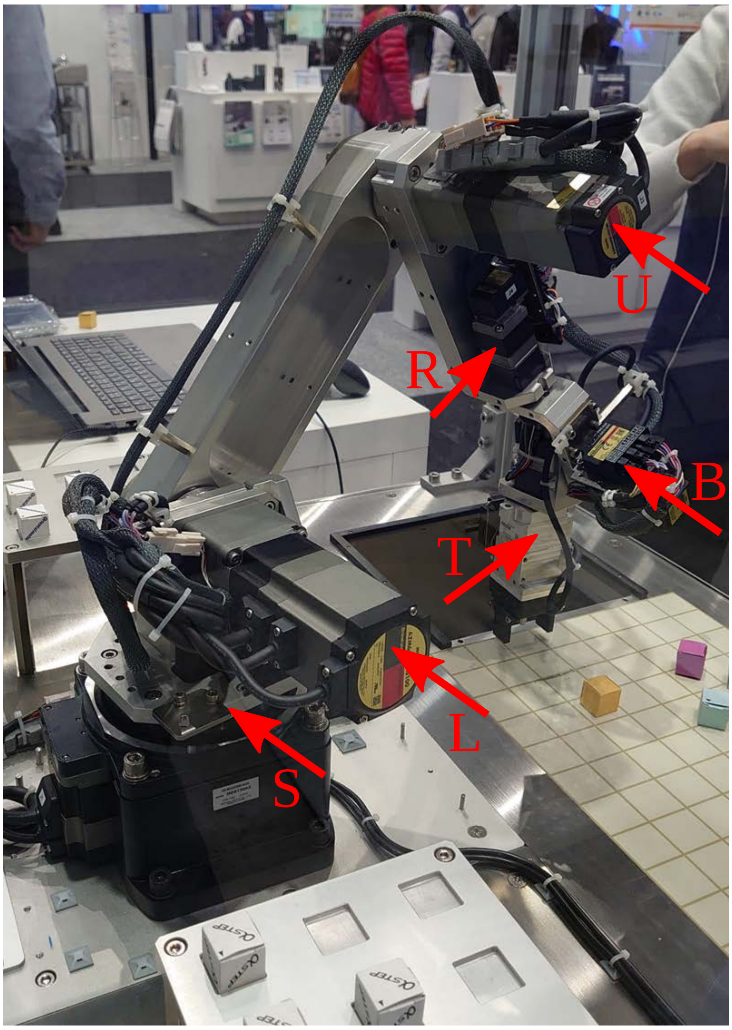

Fig. 1.1: A six-axis industrial robot. Six low-speed high-torque actuators at the joints are indicated by the red arrows.

is the typical configuration of six-axis industrial robots. Among the six actuators, R-axis actuator controls the rotation of the upper arm; B-axis actuator controls the tilting up and down of the wrist; T-axis actuator controls the rotation of wrist. In [5], the parameters of MOTOMAN-HC10DTP collaborative robot from Yaskawa are shown. Tab. 1.1 lists the maximum speed and torque of the R-, B- and T-axis actuators in the MOTOMAN-HC10DTP industrial robot. This collaborative robot is capable of holding the maximum weight of 10 kg. It can be seen that the actuators in MOTOMAN-HC10DTP operate at low speeds of only several tens of r/min. However, high torques of several tens of Nm are required.

The torque densities, including the weight torque density and the volume torque den-

Tab. 1.1: Parameters of actuators in MOTOMAN-HC10DTP industrial robot.

	R-axis	B-axis	T-axis
Maximum torque [Nm]	27.4	27.4	9.8
Maximum speed [r/min]	30	41.6	41.6

sity, are very important to evaluate the low-speed high-torque machines. A compact structure is also desirable in some cases. For example, the in-wheel motors should be short in the axial direction but can be relatively large in the radial direction. In Fig. 1.1, the L-, U- and R-axis actuators are long in the axial directions. If the volume torque densities of these actuators are higher, or the actuators are flat, the total volume of the industrial robot will be reduced. In [5], the own weight of MOTOMAN-HC10DTP is 48 kg. Improving the weight torque densities of the actuators can make the collaborative robot light.

1.2 Types of Low-Speed High-Torque Electric Machines

Generally, low-speed high-torque electric machines can be implemented by the combination of electric machines and speed reducers, or using direct-drive machines without extra speed reducers. In the present section, five typical types of speed reducers are introduced, including the spur gear, planetary gear, cycloidal drive, strain wave gear and magnetic gear. As for the direct-drive machines, the principles and characteristics of the PM servo motor, vernier machine and magnetic-geared machine are introduced.

1.2.1 Combination of Electric Machines and Speed Reducers

Electric machines normally have high power densities at high rotational speeds. On the contrary, to realize high torques at low speeds, the diameters of electric machines tend to be large, leading to large machine volumes. Thus, combining the high-speed electric machine and speed reducer is a reasonable option to match the speed range and torque of the target application. As an example, a PM motor and a gear from Maxon are picked up [6]. Tab. 1.2 shows the parameters of the PM motor and Tab. 1.3 shows the

Tab. 1.2: Parameters of a PM motor from Maxon.

Power	Maximum speed	Torque	Efficiency	Power density	Torque density
200 W	16100 r/min	0.1 Nm	90 %	3.6 kW/L	2.1 Nm/L

Tab. 1.3: Parameters of the combination of a PM motor and a gear from Maxon.

transmission ratio	Gear efficiency	Maximum speed	Torque	Torque density
103 (3 stages)	90 %	156 r/min	8.9 Nm	43 Nm/L

parameters of the combination of the PM motor and gear. The PM motor and gear have identical rated power of 200 W. The PM motor operates at the maximum speed of 16100 r/min with a small torque of 0.1 Nm. The power density is as high as 3.6 kW/L but the torque density is only 2.1 Nm/L. After combined with the gear with a transmission ratio of 103, the torque reaches 8.9 Nm. The corresponding torque density is 43 Nm/L, which is 20 times higher than the PM motor. Although the gear increases the volume, the torque density still improves significantly thanks to the high transmission ratio. This typical example indicates that the performance of low-speed high-torque machines with speed reducers highly depends on the speed reducers. Thus, several typical speed reducers are introduced here.

Spur Gear

The spur gear is the most common type of gears. Generally, the spur gear has a cylindrical shape. The gear teeth are distributed radially on the cylindrical surface. When the gear teeth are on the external surface of the cylinder, the gear is called an external gear. On the contrary, when the gear teeth are on the internal surface of the cylinder, the gear is called an internal gear. An external gear can mesh with an external gear or an internal gear, whereas an internal gear can only mesh with an external gear. The meshed gears have parallel axes and there is no axial load on the gear teeth. The most common tooth profile of spur gears is the involute type.

When two external gears are meshed as shown in Fig. 1.2(a), the gears rotates in the opposite directions. If the tooth numbers of the input gear and the output gear are Z_i and Z_o, respectively, the transmission ratio G is presented as

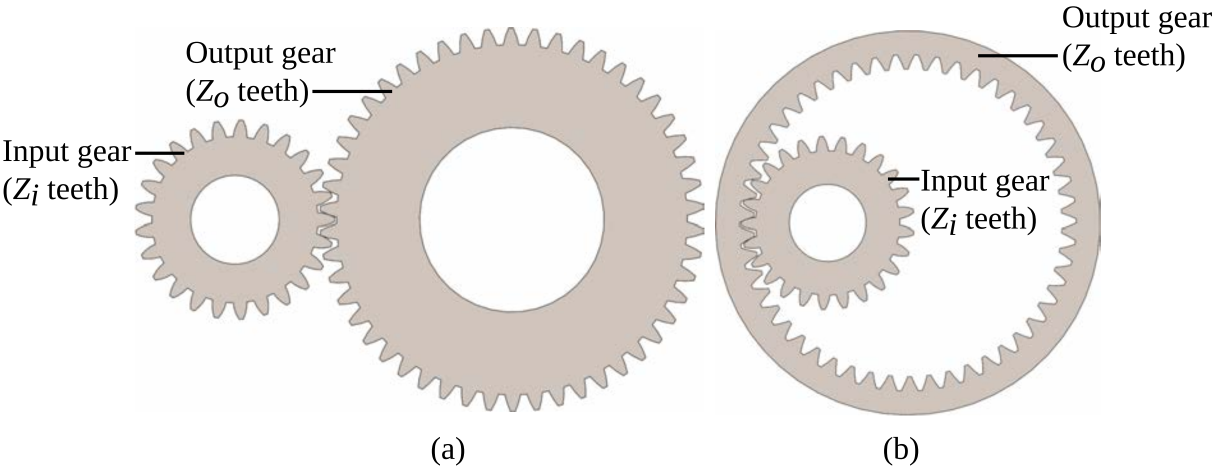

Fig. 1.2: Spur gears. (a) Two external gears. (b) An external gear and an internal gear.

$$G = -\frac{Z_o}{Z_i}. \tag{1.1}$$

The minus symbol indicates the opposite rotating directions. When an internal gear is meshed with an external gear as shown in Fig. 1.2(b), the gears rotate in the identical direction and the transmission ratio becomes

$$G = \frac{Z_o}{Z_i}. \tag{1.2}$$

Moreover, the combination of the internal gear and external gear is more compact than the combination of two external gears, due to the close center distance between the axes of the internal gear and external gear.

Planetary Gear

The planetary gear consists of a sun gear, a ring internal gear, several planet gears and a carrier for the planet gears. The sun gear is at the center and meshes with the planet gears. The planet gears also mesh with the ring internal gear. The shafts of the planet gears are connected to the carrier. When the carrier rotates, the planet gears will have an orbital motion.

By fixing different parts, the planetary gear can have different transmission ratios. If the ring internal gear is fixed, the sun gear is set as the input, and the carrier is set as

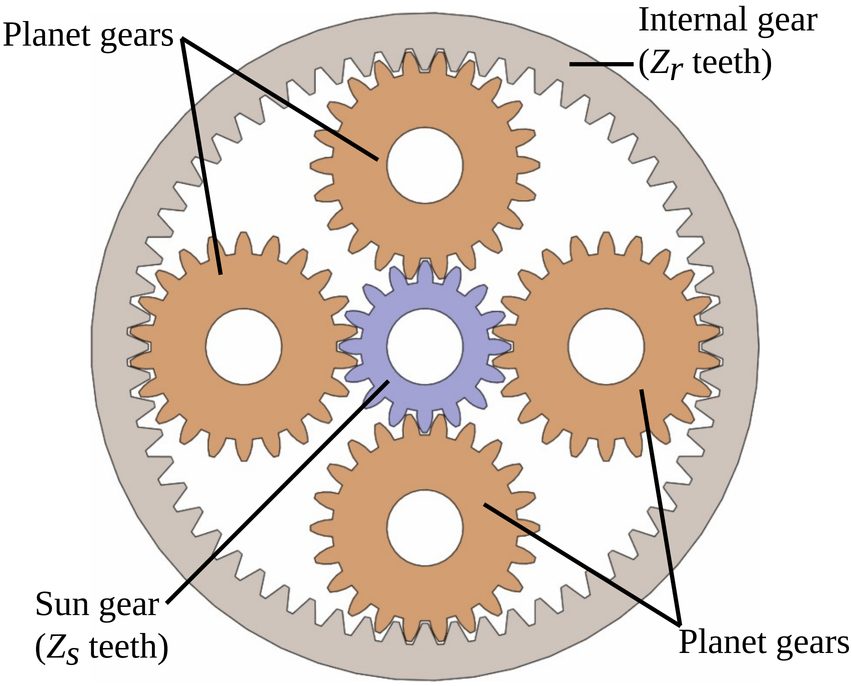

Fig. 1.3: Structure of the planetary gear.

the output, the transmission ratio G is

$$G = \frac{Z_r}{Z_s} + 1 \tag{1.3}$$

where Z_r and Z_s are the tooth numbers of the ring internal gear and sun gear, respectively. If the sun gear is fixed, the ring internal gear is set as the input, and the carrier is set as the output, the transmission ratio G is

$$G = \frac{Z_s}{Z_r} + 1. \tag{1.4}$$

Since the ring internal gear has more gear teeth than the sun gear, the transmission ratio in (1.3) is higher. To reach a high transmission ratio, a small sun gear and a large ring internal gear are required.

The planetary gear has a complicated structure. The tooth shape of the planet gears should be carefully designed to avoid any interference. However, the multiple planet gears can share the load. Thus, the friction loss from the meshed teeth is low, and the torque capability is high. The planetary gears are used in servo motors and also automobiles as a vital part of automatic transmission.

Cycloidal Drive

The cycloidal drive is a high-gear-ratio speed reducer using the planocentric gearing mechanism [7]. The rotation of an input motor is converted into the circular (or orbital) motion by crankshafts. The rotation speed and the circular motion speed are identical. Then, the high-speed circular motion is converted into the low-speed rotation by the gears. The gear profile is normally cycloidal type. Compared with involute-type gears, cycloidal-type gears have much more simultaneously meshing teeth, which leads to high torque capability and rigid construction. Maintaining an accurate center distance between the cycloidal-type gears and pins (or rollers) is essential for typical cycloidal drives, which requires a precise manufacturing and assembly. One of the most famous products equipped with cycloidal drives is the RV speed reducer from Nabetesco [8].

Strain Wave Gear

The strain wave gear, also known as the harmonic drive, is famous for its zero-backlash characteristic. Its basic structure is shown in Fig. 1.4. The input shaft is connected to the “wave generator” which has an elliptical shape. The “flexspline” is a thin cylindrical external gear and mounted outside the wave generator. The flexspline is deformable and follows the elliptical shape of the wave generator when the wave generator rotates. The “circular spline” is a stationary internal gear. In the direction of the major axis of the elliptical shape, the flexspline fully meshes with the circular spline and leads to zero backlash. Zero backlash indicates that the strain wave gear can realize high-precision position control. The output is connected to the flexspline.

If the circular spline has Z_c teeth and the flexspline has Z_f teeth, the transmission ratio of the strain wave gear G is

$$G = \frac{Z_f}{Z_f - Z_c}. \tag{1.5}$$

It should also be noted that the flexspline rotates in the opposite direction with the input shaft because Z_f is smaller than Z_c. The tooth number difference between Z_f and Z_c is kept small to give a high transmission ratio. The minimum tooth number difference is 2. For example, to reach a high transmission ratio of 100, the tooth numbers are as large

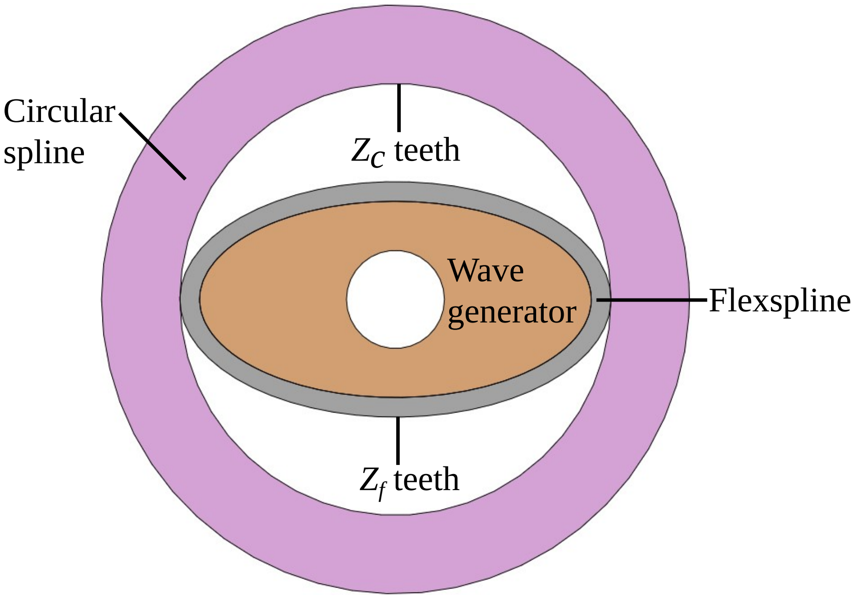

Fig. 1.4: Structure of the strain wave gear. Gear teeth are simplified into circles.

as 200 and 198. It is claimed that a special S tooth profile is applied in products from Harmonic Drive [9]. As a result, up to 30% of the total gear teeth mesh simultaneously. Thus, the strain wave gear can be compact and rigid even with small gear teeth.

The strain wave gear sacrifices the gear efficiency to realize zero backlash. For example, the CSF-mini series has the efficiency of 50%-70% with the transmission ratio of 100 under the ambient temperature of 20°C [10]. As a comparison, the efficiency of involute spur gears can be higher than 90%. Moreover, due to the high transmission ratio, the strain wave gear has low backdrivability [11]. When strain wave gears are applied in a collaborative robot, extra torque sensors are necessary to implement the reverse driving, which increases the cost and system complexity.

Magnetic Gear

Although mechanical gears are dominant among speed reducers, there are also some disadvantages. Due to the physical contact between gear teeth, mechanical gears need regular maintenance and lubrication. Moreover, the gear teeth may break if the gear suffers from overload.

Magnetic gears did not receive much interest from researchers before due to their low torque capability. The presence of rare-earth NdFeB permanent magnets (PMs)

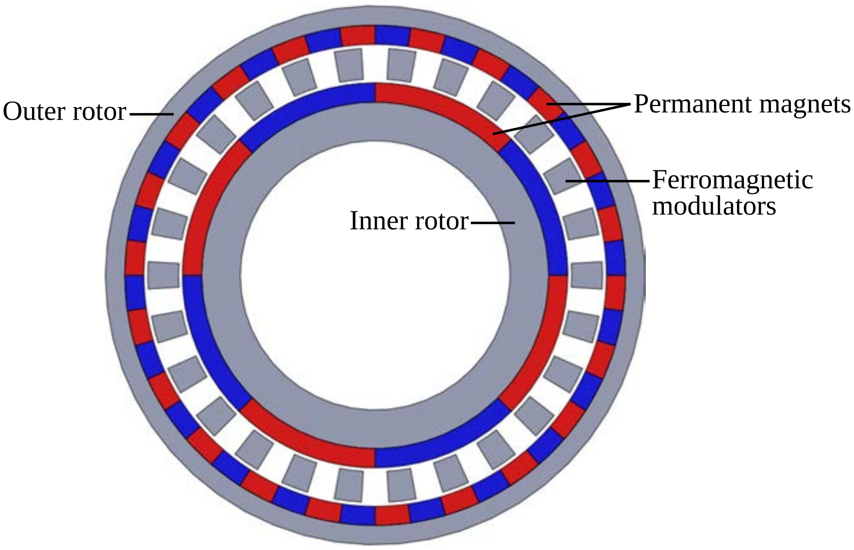

Fig. 1.5: Structure of the coaxial magnetic gear.

has changed this situation. In [12], a novel coaxial magnetic gear(CMG) equipped with sintered NdFeB PMs was first proposed. This CMG achieved a volume torque density of over 100 Nm/L in simulation, which is competitive with the torque density of mechanical gears. Fig. 1.5 shows the structure of the CMG. It has three physically isolated layers in the radial direction. The high-speed inner rotor and outer rotor have iron cores and PMs mounted on the surface of the iron cores. The ferromagnetic modulators are sandwiched between the inner rotor and outer rotor. The inner rotor is connected to the input shaft. Either the outer rotor or the ferromagnetic-modulator-layer is set as the low-speed output. The latter has a higher transmission ratio.

The CMG works based on the flux modulation effect of the modulators. Let us define the pole pair numbers of the inner rotor and outer rotor as p_i and p_o, and define the piece number of the ferromagnetic modulators as n_m. To utilize the flux modulation effect to generate constant output torque, they should satisfy

$$p_i + p_o = n_m. \tag{1.6}$$

The transmission ratio is

$$G = n_m/p_i \tag{1.7}$$

when the outer rotor is kept stationary and the ferromagnetic-modulator-layer is set as the low-speed output.

Compared with mechanical gears, magnetic gears have several obvious advantages. Since the energy is transferred by the magnetic field, the magnetic gear realizes non-contact speed reduction. Therefore, magnetic gears need no gear lubrication and reduced maintenance. In terms of overload, the low-speed high-torque rotor of a magnetic gear will only slip when overload happens. Thus, there is no risk of breaking the gear [13]. The main disadvantage of the magnetic gear is the large quantity of rare-earth PMs, which is the source of its high cost.

1.2.2 Direct-Drive Machines

Although using speed reducers has many advantages, such as the compact structure and high torque density, there are still some applications that prefer direct-drive solutions. First, direct-drive machines have less mechanical loss and better durability than mechanical gears which need more maintenance and lubrication. Second, direct-drive machines do not have backlash, indicating that high-precision position control is possible. Third, direct-drive machines have higher backdrivability than mechanical gears, especially high-gear-ratio mechanical gears [14]. This characteristic will be helpful in applications such as collaborative robots. However, the torque densities of direct-drive machines are generally low, which is the main obstacle for being applied in robotic applications.

Direct-Drive PM machine

The torque of a direct-drive PM machine can be enhanced by enlarging the diameter, increasing the current, and increasing the pole-pair number. A large current will lead to high copper loss. High-pole-pair-number PM machines are not suitable for operating at high speeds since the iron loss tends to increase at high current frequencies. As a result, the power density is generally low. Moreover, for high-pole-pair-number PM machines, it may be difficult to use distributed windings when the stator slot number is limited. Instead, non-overlapping windings are more practical [15]. Non-overlapping windings have shorter end-windings than distributed windings. The iron loss due to the extra spatial harmonics is also more manageable at low speeds.

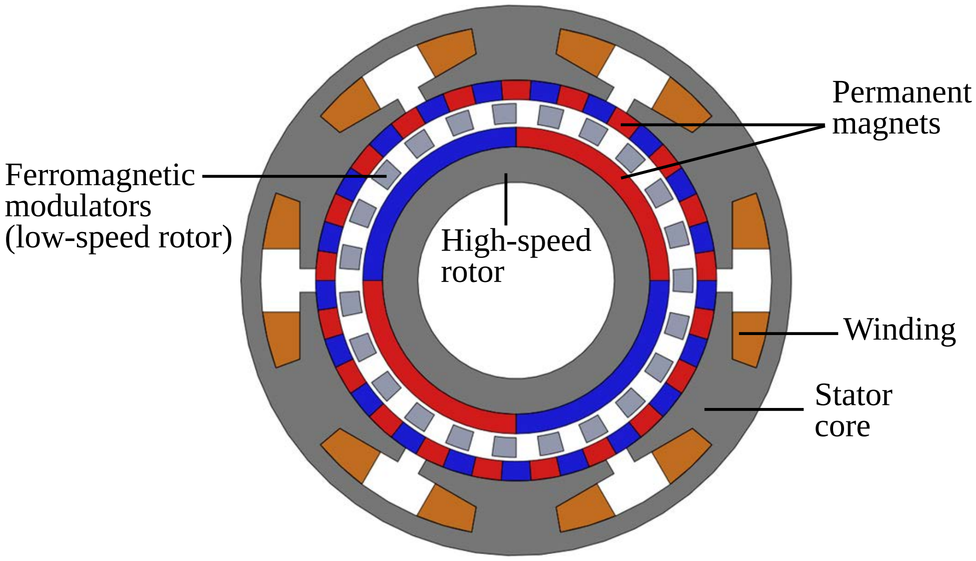

Fig. 1.6: Typical structure of magnetic-geared machines.

Vernier Machine

Vernier machine is a special type of direct-drive machines based on flux modulation effect. In a normal PM machine, the PM pole pair number should be equal to the stator pole pair number to generate constant torque. However, the PM pole pair number of the PM vernier machine is the difference between the stator slot number and stator pole pair number [16]. The flux is modulated by the stator slots. As a result, multiple spatial harmonics are utilized to generate constant torque. The rotor speed still depends on the PM pole pair number. Vernier machines generally have higher torque densities than normal PM machines. The main disadvantage of vernier machines is the low power factor.

1.2.3 Magnetic-Geared Machine

If a CMG is simply connected with a motor in the axial direction, the resultant magnetic-geared machine is obviously not a direct-drive machine. However, a CMG can be integrated with a PM machine, leading to new kinds of machines. One of the integrated machines was named as the "Pseudo" Direct Drive (PDD) [17]. Fig.1.6 shows the structure of the PDD. Compared with the CMG, the essential change is that the outer rotor is changed into a stator with non-overlapping windings. Thus, the stator and high-speed rotor constitute an input PM machine. The torque of the input PM machine is amplified on the low-speed rotor with the same transmission ratio as the CMG. The active parts of the PDD are arranged in the radial direction and there is no input shaft. Thus, the axial length can be reduced.

1.3 Contribution of this Work

In conventional rotational electric machines, the torque is generated by the integral of the electromagnetic tangential force. Since the air-gap flux density is mostly in the radial directions, the radial force on the rotor surface is predominant. However, the radial force is always regarded as a byproduct and the resultant force is designed to be zero by symmetrical motor structures [18].

In magnetic bearings and bearingless motors, the resultant radial force is utilized to make the rotor shaft levitate [19]. In 4-DOF (degrees of freedom) and 2-DOF bearingless motors, the active radial force is controlled to realize magnetic suspension [20, 21]. In 1-DOF bearingless motors, the passive radial force is utilized to maintain the stability of the levitated rotor in the radial direction [22]. At the steady state, the electromagnetic radial force does not output power.

The motivation of the proposed actuator is to utilize the electromagnetic radial force to generate the output torque and power, which was not reported in the literature. In the proposed actuator, the electromagnetic radial force generates the circular motion with a small radius. Thus, it is termed a swirling actuator. The first model of the swirling actuator was proposed by a previous member from the lab of the author. In [23], the analysis of the first model is presented by the author. Fig. 1.7 shows the basic structure of the first model. The swirler has two iron rings and an axially magnetized PM ring sandwiched by the iron rings. The PM ring generates the homopolar bias flux. The radial force components F_d and F_q are generated between the stator and swirler. The circular motion of the swirler is converted into the low-speed rotation by the integrated mechanical gears on the inner rotor.

To improve the first model, the second model is proposed in this work. It has a surface permanent magnet (SPM)-type electromagnetic structure and an outer rotor gear, which enhances the radial force, raises the transmission ratio and simplifies the machine structure

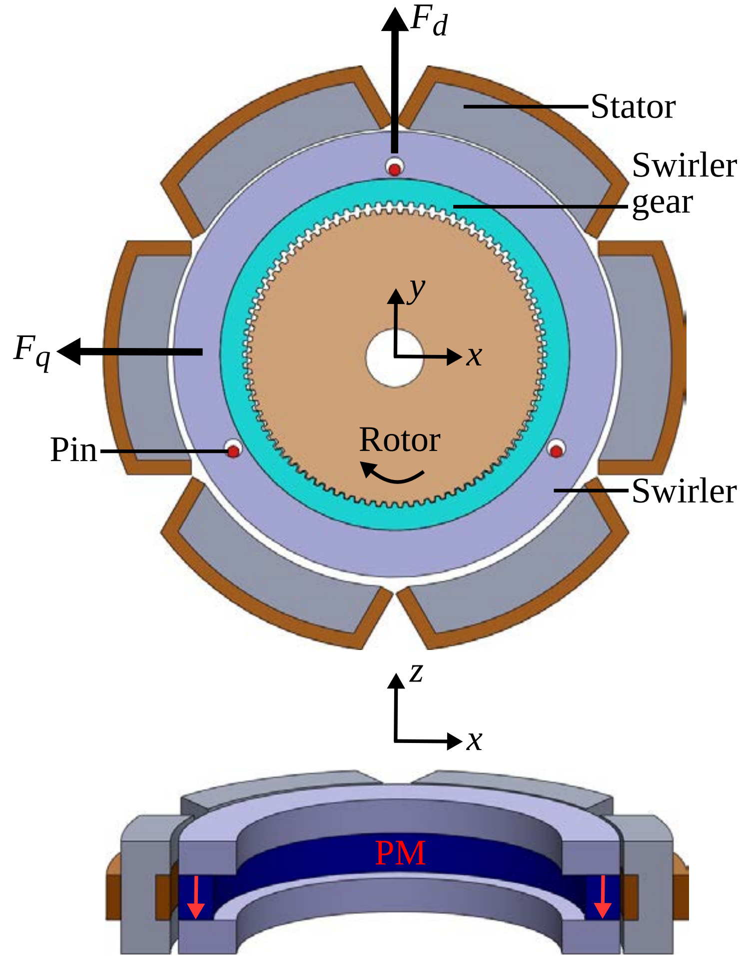

Fig. 1.7: Basic structure of the homopolar-type swirling actuator [23].

compared with the first model.

The relative motion between the swirler and rotor of the swirling actuator is the cycloidal motion. Fig. 1.8 shows the comparison between the cycloidal drive and proposed swirling actuator. Here the cycloidal drive and swirling actuator adopt identical involute-type gears. Fig. 1.8 indicates that the swirling actuator replace the input crankshaft of the cycloidal drive by the electromagnetic part. In comparison to the combination of a motor and a cycloidal drive, the swirling actuator has a similar transmission ratio, but reduces the axial length. The high transmission ratio and flat structure make the swirling actuator a promising candidate for low-speed high-torque applications such as robotic joints and wearable rehabilitation devices [24]. In this work, the proposed swirling actuator reaches a high torque density of 64 Nm/L with a small volume of 0.16 L.

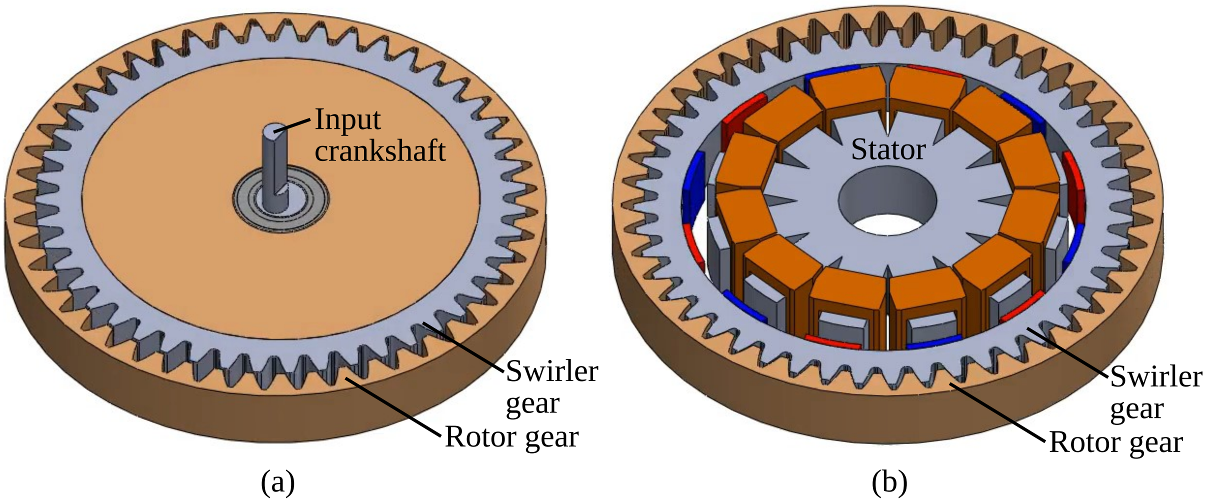

Fig. 1.8: Comparison between (a) cycloidal drive and (b) swirling actuator.

1.4 Research Objectives

This research presents the design and analysis of the low-speed high-torque swirling actuator. The swirling actuator has the electromagnetic part to generate the radial force and the mechanical part including the gears and the motion guiding part. To implement the concept of the swirling actuator, the following research objectives are investigated in the present thesis:

1. Design the electromagnetic part to generate net radial force on the swirler that has the circular motion. Find feasible combinations between the stator slot number and PM pole number.

2. Derive the air-gap flux density and radial force with the non-uniform air-gap length caused by the eccentric swirler. Validate the analytical derivations by 3-D finite element analysis (FEA). Utilize the analytical derivations to optimize the electromagnetic part.

3. Investigate the design of involute-type gears with high transmission ratios. Analyze the gear efficiency.

4. Design an experiment to measure the static electromagnetic radial force. Compare the measured radial force with the analytical derivation and FEA result.

5. Evaluate the torque capabilities of swirling actuators experimentally.

1.5 Thesis Organization

Chapter 1 is the present chapter. First, the applications of low-speed high-torque electric machines are introduced. Second, the basic principles and characteristics of various speed reducers, direct-drive machines and geared machines are simply described.

Chapter 2 presents the literature review. More details of typical low-speed high-torque electric machines are introduced and their torque densities and volumes are summarized and compared. Moreover, literature about cycloidal machines is also introduced because it serves as a good reference for the mechanical design.

Chapter 3 presents the principle and analysis of the swirling actuator. The design procedures of the stator windings are introduced. The radial force is calculated analytically, verified by 3-D FEA and measured by a simple experiment. The torque of a preliminary prototype is measured and the gear efficiency is evaluated.

Chapter 4 presents the torque density improvement of the swirling actuator. First, the electromagnetic radial force is enhanced by adjusting the dimensions and material of the swirler. The FEA results of the improved electromagnetic part are shown. Second, the parameters of the involute-type gears are analyzed and a new gear set is designed. Experimental results of two new prototypes are shown.

Chapter 5 gives the conclusion. In addition to the summary of the achieved performance, future work about possible improvements of the proposed swirling actuator are described.

Chapter 2

Literature Review

2.1 Introduction

The principles of low-speed high-torque electric machines and typical speed reducers are simply introduced in Chapter 1. In this chapter, examples of direct-drive electric machines, magnetic gears and geared machines from literature are listed. In addition, special attention is given to cycloidal machines because their motion is similar to that of the proposed swirling actuator and the mechanical designs provide a useful reference.

2.2 Direct-Drive Electric Machines

2.2.1 Direct-Drive Servo Motors

The SGM7D series of low-speed high-torque direct-drive servo motors from Yaskawa is set as an example [25]. The series has servo motors with different sizes and torque capabilities. Tab. 2.1 lists the parameters of two motors from the series. One has the smallest size and the other has the largest size. The small model has a low rated speed of 120 r/min and a torque density of 6 Nm/L. The large model has an even lower rated speed of 30 r/min and a torque density of 20 Nm/L. The torque density is improved in the large model. However, the power densities of the two models are low. The large model has a power density of 38 W/L. As a comparison, the high-speed PM machine used in the second-generation Toyota Prius hybrid electric vehicle has the same maximum torque

Tab. 2.1: Parameters of direct-drive servo motors from Yaskawa.

Product code	SGM7D-03H	SGM7D-2DI
Rated speed	120 r/min	30 r/min
Peak torque	4 Nm	400 Nm
Rated output	38 W	754 W
Diameter	116 mm	264 mm
Axial length	63 mm	358 mm
Volume	0.7 L	19.6 L
Torque density	6 Nm/L	20 Nm/L
Power density	57 W/L	38 W/L

of 400 Nm. However, its power density is as high as 5.6 kW/L since it operates at high speeds of 1200-6000 r/min [26]. Thus, conventional direct-drive PM servo motors are not suitable for high-power applications due to the large dimensions.

2.2.2 PM Vernier Machines

The simplest PM vernier machine only changes the PM pole pair number compared with a conventional PM machine. In [27], an optimized 12-slot vernier machine with 11-pole-pair of surface-mounted PMs on the rotor was designed and tested. The torque was 17.4 Nm and the torque density was 21 Nm/L. The instantaneous torque equation of the PM vernier machine was derived and it was shown that the the torque ripple of PM vernier machines is essentially low. The power factor was only 0.6, which is typical in SPM-type vernier machines.

Another typical structure of PM vernier machines is the stator with auxiliary split teeth [28], [29]. The split teeth perform as the flux modulation poles (FMPs). In [29], the proposed model has a 6-slot-4-pole stator with non-overlapping windings. Each stator tooth has two split teeth and the machine has 12 FMPs. By carefully design the pitch of the FMPs, the authors claimed that the proposed configuration has a torque density improvement of more than 20%. The test prototype has a torque of 21 Nm and reaches a torque density of 21 Nm/L. In [30], the authors further made the split teeth into stage-cut coding-shaped teeth to utilize multiple spatial harmonics that contribute to torque generation. The output average torque was 30% larger than the machine with regular split teeth.

To improve the power factor of vernier machines, several new topologies were proposed. One effective topology is the double-stator spoke-array (DSSA) vernier machine [31–34]. The spoke-array rotor can increase the air-gap flux density and reduce the flux leakage, which is the reason for the high power factor. In [32], analytical derivation was presented to indicate that it is difficult for a SPM vernier machine to reach a high power factor. Instead, the DSSA vernier machine could reach a high torque and a power factor greater than 0.9 with 12-slot-4-pole stators. In [33], the authors tested a 24-slot-22-pole-pair DSSA vernier machine with a large volume of more than 30 L. The torque density reached a notable value of 66 Nm/L and the power factor was 0.83. In [34], 12-slot-10-pole-pair DSSA vernier machines with low-cost ferrite magnets were designed and compared with a 48-slot-2-pole-pair interior permanent magnet (IPM) machine. The ferrite DSSA vernier machine had 33% higher torque than the IPM machine using rare-earth PMs. The relatively small power factor of 0.72 was the trade off to obtain the high torque and efficiency, but it is still better than those of SPM vernier machines.

Besides radial flux vernier machines, axial flux vernier machines were also investigated. In [35], an axial-flux DSSA vernier machine was proposed. The 18-slot-17-pole-pair machine had a torque density of 37.7 Nm/L from 3-D Finite Element Analysis (FEA). The power factor was also as high as 0.89, which was similar to that of a radial flux DSSA vernier machine. In [36], a triple-rotor dual-stator axial vernier machine was built and tested. The inner rotor also had spoke-array PMs, whereas the outer rotors were SPM type. Despite the complicated structure, the torque density of 24.4 Nm/L was not very high, but the power factor was as high as 0.93. In [37], a novel vernier machine that combined the axial flux and radial flux machines was proposed. A set of toroidal windings was configured on the stator and the "end-windings" were utilized to couple with the axial rotors. With the increased rotor area that contributed to torque generation, the torque density was greatly enhanced. It was claimed that a 17-pole-pair model can generate a torque density of 57.8 Nm/L, which was significant among direct-drive electric machines.

There are many other different structures of PM vernier machines. The vernier machine in [38] has an outer spoke-type rotor and a hybrid stator with split teeth and straight teeth. Consequent-pole rotors were adopted to reduce the quantity of PMs [39–46]. Among them, the vernier machines in [44–46] have both PMs on the rotor and stator, and the stator PMs are arranged non-uniformly to introduce additional reluctance torque.

2.2.3 Other Direct-Drive Electric Machines

In [47], an outer-rotor switched flux memory machine was presented. The main characteristic of memory machines is the use of low-coercive-force (LCF) magnets, in which the flux density level can be changed by a pulse current within a very short time duration and then memorized [48, 49]. The authors designed a hybrid stator that have LCF magnets and rare-earth PMs. The thin outer rotor and spoke-type PMs help enlarge the available space of the components on the stator. The optimized model had a torque density of 31.6 Nm/L.

In [50], a novel claw-pole-stator PM motor was designed. The stator has 3 claw-pole-layers corresponding with 3 phases. Each claw-pole-layer has 20 claw poles and the rotor also has 20 poles of PMs. It was shown by 3-D FEA that the motor can provide a peak torque density of 37.65 Nm/L with a small volume of 0.2 L.

In [51], a so-called airgap-less electric motor was proposed. The outer rotor ring does not have any saliency and not constrained in the radial direction. Thus, it touches the stator teeth during the operation, leading to a zero air-gap length at the contact point. Obviously, the motion of the rotor is the cycloidal motion that is the combination between the circular motion and rotation. To provide the output torque, a motion converter such as a cycloidal drive was necessary, which was not included in the initial prototype. The authors claimed a weight torque density of 5.6 Nm/kg.

In [52], a cycloidal reluctance machine was compared with a switched reluctance machine. The salient rotor of the switched reluctance machine was replaced by a ring-shaped rotor. The rotor has a cycloidal motion and the non-uniform air-gap length provides the ratio between the aligned inductance and unaligned inductance. A prototype with an identical minimum air-gap length to that of the switched reluctance machine was built and only the static torque was measured. The cycloidal reluctance machine showed a higher static torque-per-ampere than the couterpart switched reluctance machine.

2.3 Magnetic Gears and Magnetic-Geared Machines

2.3.1 Coaxial Magnetic Gears

The classic SPM-structure CMG was analyzed by 2D FEA in [12] and a prototype was tested in [53]. The prototype in [53] has stationary ferromagnetic modulators and a transmission ratio of 5.75. The torque density was higher than 100 Nm/L, whereas the measured torque density dropped to 72 Nm/L. The authors stated that the discrepancy was due to the significant end-effects caused by long effective magnetic air-gaps. In [54], a prototype with a transmission ratio of 5.5 and standard rectangular PMs was built. This prototype also suffered from the large end-effects and the measured torque density was 54 Nm/L.

Different topologies have been investigated and optimized to improve the torque densities of CMGs. By changing the radial PMs into Halbach-array PMs on both the inner and outer rotors, the pull-out torque, efficiency and torque ripple were improved [55]. Spoke-array PMs provide flux focusing effects that can increase the air-gap flux density. The CMG in [56] adopted spoke-array PMs in both the inner and outer rotors. A parameter sweep analysis was conducted to maximum the volume torque density. Experimental results showed that the volume torque density reached 239 Nm/L. In [57], to reduce the flux leakage of the spoke-array PMs on the outer rotor, an auxiliary flux modulator was set outside the outer rotor. Moreover, high-temperature-superconducting bulks on the inner flux-modulator-layer and uneven segment PMs on the inner rotor also help improve the torque density to a notable value of 266.89 Nm/L. Besides the radial-flux CMGs, the axial-flux counterparts also have great potential. A comparative study between the radial-flux and axial-flux SPM-type CMGs was conducted in [58]. The axial-flux CMG can outperform its radial-flux counterpart when it has a large diameter and a short axial length. In [59], an axial-transverse-flux CMG was proposed. The optimized torque density reached 282.56 Nm/L, and the authors claimed that the gear can maintain high torque densities of over 150 Nm/L within a wide range of length-diameter ratios, which outperforms the axial-flux CMG.

To deal with the issue of the high cost of CMGs, researchers have tried to reduce the quantity of rare-earth PMs or use cheaper magnets. A detailed comparison between NdFeB and ferrite SPM-type CMGs was presented in [60]. It was shown that even the most cost-effective design of the ferrite gear is still more expensive than the NdFeB gear due to the large active material mass. It is generally preferable to adopt NdFeB designs in SPM-type CMGs. Meanwhile, it is interesting that the ferrite-version of the spoke-array-type CMG in [56] could provide a good volume torque density of 84 Nm/L. Another attempt to reduce the cost is the reluctance-type CMG [61]. The high-speed-rotor only has an iron core with salient poles. This structure is simple, robust, and more suitable for high-speed operation. However, the torque density was inevitably much lower than the SPM-type CMG.

The single-stage CMG generally has a transmission ratio lower than 10, which may not be enough for some applications that operate at very low speeds. There are two reasons for the low transmission ratio. The first reason is the limited pole numbers due to practical constraints; the second reason is that the CMG tends to have high torque densities with low transmission ratios [62]. If high transmission ratios are required, multi-stage CMGs can be adopted. In [63], two types of multi-stage CMGs were analyzed. The first type is connecting the single-stage CMGs in series. The resultant transmission ratio is the product of the transmission ratios of single-stage CMGs. The second type is called the compound differential CMG. In this configuration, the resultant transmission ratio can be much higher than the first type if the difference of transmission ratios between the single-stage CMGs is small.

The transmission ratio of the CMG can be changed as shown in [64]. The conventional segment PMs on the two rotors were replaced by many small cylindrical diametrically magnetized PMs. Each cylindrical PM can rotate independently by spur gears, leading to different pole-pair numbers and transmission ratios.

2.3.2 Magnetic-Geared Machines

CMGs can be directly connected to high-speed electric machines in the axial direction as shown in [65–67]. The resultant magnetic-geared machines (MGMs) have the cylindrical shape with long axial lengths.

Meanwhile, magnetic-geared machines with integrated CMGs have received more interest. The first typical structure is inserting an outer-rotor SPM machine inside the inner rotor of the SPM-type CMG. There are 3 layers of PMs in this structure. In [68], a MGM for in-wheel motors was proposed. The SPM machine and the inner rotor of the CMG both have 3 pole-pairs, and the outer rotor of the CMG has 22 pole-pairs. A notable torque density of 87 Nm/L was achieved from 2-D FEA. In [69], the MGM adopted Halbach-array PMs. The PM machine and the inner rotor of the CMG had different pole-pair numbers. The torque density was 40 Nm/L. In [70,71], an interior permanent magnet (IPM)-structure MGM was designed for walking support machines. The 4 pole-pair IPMs were shared by the PM machine and the inner rotor of the CMG, which reduced the eddy current loss of the inner rotor. The measured torque density was 27 Nm/L. In [72], the axial-flux-type MGM was designed and prototyped.

PDD machines are another type of MGM, as mentioned in Chapter 1.2.3. The first PDD machine realized a torque density exceeding 60 Nm/L under a low current density of 2 A/mm^2 [17]. Several products of PDD machines have been developed from Magnomatics. The 65-kW PDD traction motor has a torque density of 62 Nm/L [4]. The 5.5-kW PDD marine current turbine generator has a torque density of 36 Nm/L and operates at 100 r/min [73]. The PDD aerospace actuator has a torque density of 45 Nm/L with a small volume of 0.23 L [74]. There are also some variants of PDD machines, such as the IPM-inner-rotor-type PDD [75], and the Halbach-consequent-pole-type PDD [76]. Moreover, by eliminating the ferromagnetic-modulator-layer in the PDD machine and set the outer layer of PMs as the low-speed rotor, a vernier PDD was proposed as the stator straight teeth perform as the FMPs [77]. An improved version of [77] that adopted split teeth to be the FMPs was presented in [78]. Non-overlapping windings with short end-windings were configured thanks to the split teeth. The torque density considering the end-windings were 40.3 Nm/L and 78.1 Nm/L, respectively in [77] and [78].

2.3.3 Cycloidal Magnetic Gears

The cycloidal magnetic gear (CyMG) is the magnetic conterpart of the cycloidal drive. Fig. 2.1 shows the basic structure of a CyMG. There are an inner rotor and an outer

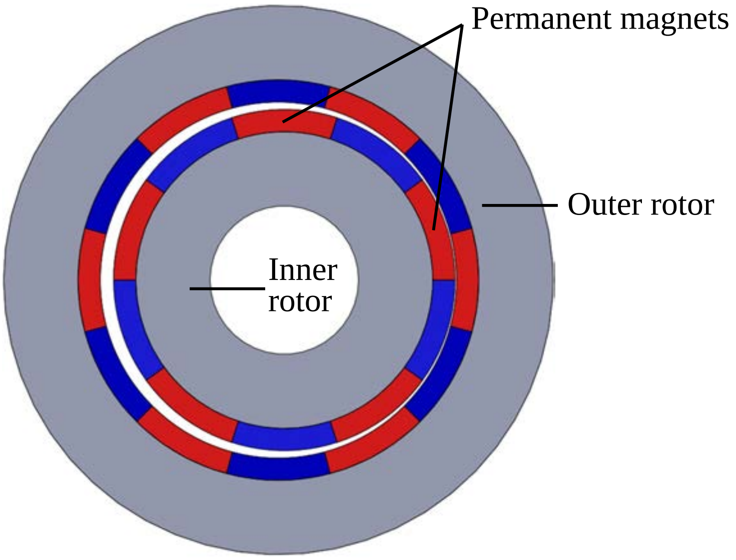

Fig. 2.1: Structure of the cycloidal magnetic gear.

rotor with p_i and p_o pole pairs of SPMs, respectively. Compared with the CMG, there is no ferromagnetic modulator in the CyMG. It should be noted that the inner rotor is eccentric with the outer rotor, which leads to an non-uniform air-gap length. It is this non-uniform air-gap length that modulates the air-gap flux density to generate constant torque. When the outer rotor is fixed, and the inner rotor has a cycloidal motion which consists of the high-speed circular motion and low-speed rotation, the transmission ratio is

$$G = p_i/(p_i - p_o). \tag{2.1}$$

When the outer rotor rotates and the inner rotor has a circular motion, the transmission ratio becomes

$$G = p_o/(p_o - p_i). \tag{2.2}$$

Compared with CMGs, CyMGs can realize higher transmission ratios. It was shown that CyMGs also favour high transmission ratios to realize high torque densities [62].

In [79], a SPM-type CyMG with a transmission ratio of -21 was proposed. The mechanical design of a prototype machine was investigated. To cancel the unbalanced PM attractive force on the frame, two gear sets with a phase difference of 180° were equipped. A torque density of 107 Nm/L was realized in experiments.

In [80], a CyMG with spoke-array-type rotors was proposed. It had a transmission ratio of -25 and with a parameter sweep analysis, it reached a high torque density of 291 Nm/L in 2-D FEA.

In [81], the axial-flux CyMG was first proposed. In [82], the axial-flux and radial-flux CyMGs with Halbach-array PMs were optimized and compared. The axial-flux CyMG provided a higher torque density of 475 Nm/L. The authors also pointed out that both the axial-flux and radial-flux CyMGs exhibits non-uniform, large and unbalanced radial forces on the eccentric rotors, which are the main obstacle for practical applications. Thus, in [83], they proposed a multi-layer axial-flux CyMG aiming to minimize the unbalanced radial force. This machine had a high transmission ratio of 96 and a torque density of 251 Nm/L. However, it had 8-layers of PMs which led to a very high cost.

For a single-stage CyMG, another issue is that the output rotor shaft is intrinsically an eccentric shaft. In [84], a dual-stage CyMG was proposed. The aim for adopting a dual-stage structure was to connect the outer rotor of the second stage, which is not eccentric, to the output shaft. The dual-stage configuration is similar to the compound differential CMG [63]. The resultant transmission ratio was as high as 360 but the torque density was only 75 Nm/L. In [85], a dual-rotor planetary magnetic gear was proposed. It can be regarded as two CyMGs connected in the radial direction. Although the high-speed rotor has a cycloidal motion, the low-speed inner rotor is not eccentric and the output shaft is concentric to the input main axis. The disadvantage of this configuration is that the transmission ratio is lower than those of the two equivalent single-stage CyMGs.

2.4 Mechanical-Geared Machines

Several products of mechanical-geared machines from manufactures are selected as examples. The SGM7P series of actuators from Yaskawa are equipped with planetary gears [25]. Tab. 2.2 lists the parameters of several actuators in SGM7P series. The input motor SGM7P-01A7J6 has a rated power of 100 W, and the geared actuators with transmission ratios of 3-50 are shown. The torque density of the input motor is 4.4 Nm/L, whereas the torque densities of the geared machines increase to 6.1-77.1 Nm/L. High-transmission-ratio gears can greatly improve the torque densities. Note that when the transmission ratios are 25 and 50, the axial lengths increase, indicating that the

Tab. 2.2: Parameters of actuators in SGM7P series with planetary gears.

Product code	G	Peak torque	Diameter	Axial length	Torque density
SGM7P-01A7J6	N/A	0.96 Nm	60 mm	60 mm	4.4 Nm/L
S7P01A-VL050-03	3	2.72 Nm	60 mm	124 mm	6.1 Nm/L
S7P01A-VL050-05	5	4.54 Nm	60 mm	124 mm	10.2 Nm/L
S7P01A-VL050-10	10	9.07 Nm	60 mm	124 mm	20.3 Nm/L
S7P01A-VL050-25	25	18 Nm	60 mm	140.5 mm	35.6 Nm/L
S7P01A-VL070-50	50	43 Nm	60 mm	155 mm	77.1 Nm/L

Tab. 2.3: Parameters of actuators in FLA series with strain wave gears.

Product code	G	Peak torque	Diameter	Axial length	Torque density
FLA-11A	100	11 Nm	71 mm	40.3 mm	69 Nm/L
FLA-14A	100	18.2 Nm	85 mm	45.3 mm	71 Nm/L
FLA-17A	100	34 Nm	92 mm	51.8 mm	99 Nm/L

high-transmission-ratio gears require larger volumes.

The FLA series of actuators from Harmonic Drive are equipped with strain wave gears [86]. It is claimed that this series has flat shapes compared with previous series, indicating that there have been requirements for flat actuators. Tab. 2.3 lists the parameters of actuators in FLA series. The transmission ratio is as high as 100, leading to notable torque densities of 69-99 Nm/L with small volumes. Moreover, the torque densities increase with the machine dimensions with the same transmission ratio. Thus, the torque density improvement may origin from equipping larger input electric machines.

The AF series of actuators from Nabtesco are equipped with cycloidal drives [87]. Tab. 2.4 lists the parameters of two actuators in AF series. These two models are the smallest among the series. However, they are still much larger than the products shown in Tab. 2.2 and Tab. 2.3. This may indicate that the high-transmission-ratio cycloidal drives are difficult to be more compact. Despite the large machine volumes, the torque densities are higher than 100 Nm/L.

There are also several special machines from literature that utilize the principle of cycloidal drives. In [88] and [89], actuators driven by shape-memory-alloy (SMA) wires were presented. The contraction and expansion of SMA wires led to the circular motion. In [88], the circular motion was converted to the rotation by a cycloidal drive with involute-type teeth. In [89], the circular motion was converted to the rotation by crankshafts. The cycloidal drive with cycloidal-type teeth was equipped to amplify the torque. In [90], a

Tab. 2.4: Parameters of actuators in AF series with cycloidal drives.

Product code	G	Peak torque	Diameter	Axial length	Torque density
AF017N081	81	289 Nm	133 mm	189 mm	110 Nm/L
AF017N126	126	415 Nm	133 mm	249.2 mm	120 Nm/L

miniature machine was proposed for noncontact operations in medical procedures. It was driven by an external rotating magnetic field. A cycloidal drive with involute-type teeth was used, which realized a high transmission ratio of 29 with a diameter of only 11 mm.

2.5 Comparison of Low-Speed High-Torque Electric Machines

Fig. 2.2 shows the volume torque densities with the volumes of some representative low-speed high-torque electric machines introduced previously. Conventional direct-drive PM machines have low torque densities. Various special direct-drive machines improve the torque densities up to around 40 Nm/L with small volumes. The magnetic-geared machines have recently shown higher torque densities than direct-drive machines. The products from Magnomatics have covered different sizes and applications. Moreover, mechanical-geared machines have the highest torque densities.

An important criterion for evaluating low-speed high-torque machines is the transmission ratios. High-performance mechanical gears can achieve transmission ratios higher than 100 with a small volume. In contrast, the transmission ratios of direct-drive machines and magnetic-geared machines are normally limited by the numbers of PM pole pairs and FMPs, which is an essential reason for the inferior torque densities.

Note that for mechanical geared machines and direct-drive servo motors, data of peak torques at peak currents are always provided. Meanwhile, most vernier machines and magnetic-geared machines in the literature only report continuous torque values at rated currents. Thus, Fig. 2.2 is not a completely fair comparison. It only serves as a rough evaluation for the torque capabilities of different types of low-speed high-torque machines.

The developed swirling actuator has a competitive torque density of 64 Nm/L with a small volume of 0.16 L. It has a flat structure and can have a transmission ratio higher

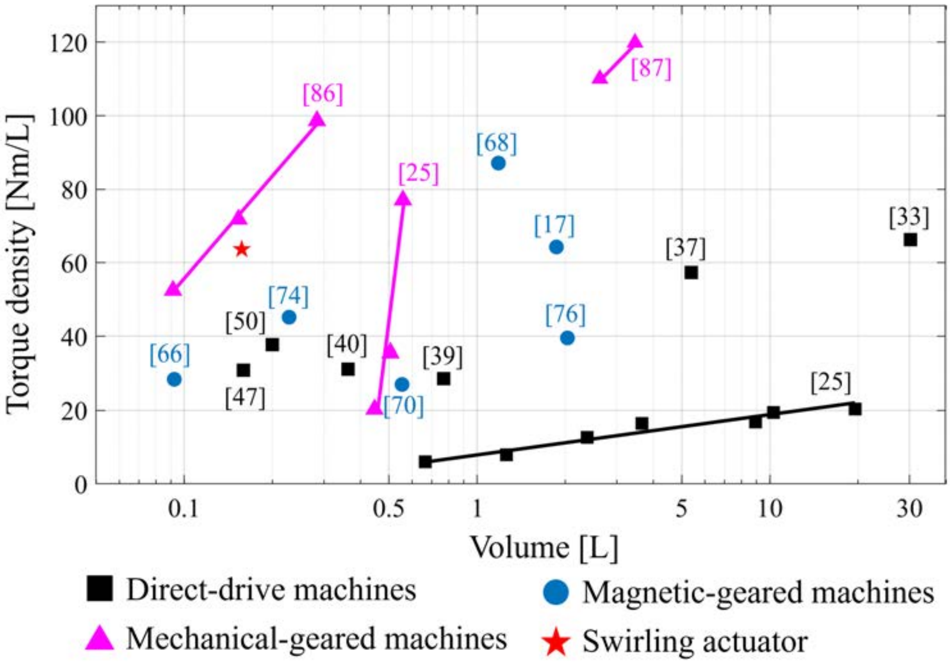

Fig. 2.2: Torque densities with volumes of low-speed high-torque electric machines.

than 100. The actuator does not require a large quantity of rare-earth PMs and adopts common involute-type gears, leading to a low machine cost. These characteristics make the swirling actuator an attractive choice for low-speed high-torque applications.

2.6 Summary

This chapter presents a literature review of low-speed high-torque machines including direct-drive electric machines, coaxial and cycloidal magnetic gears, and geared machines. The topologies, transmission ratios and torque densities are summarized and compared.

Chapter 3

Principle and Analysis of Swirling Actuator

3.1 Introduction

In this chapter, the design and evaluation of a swirling actuator with SPM-type swirler is presented in detail. First, the principle of the swirling actuator is introduced. Second, the electromagnetic part is designed and analyzed. A preliminary prototype was built and experimental results of radial force and torque measurement are presented.

3.2 Basic Structure and Operating Principle

Fig. 3.1 shows the basic structure of the swirling actuator and the schematic of the radial force and torque generation. The actuator consists of an inner stator, a swirler with outer gear teeth, and an outer rotor with inner gear teeth. The 12-pole PMs are mounted on the inner surface of the swirler and magnetized in the radial direction. Three-phase AC currents flow into the non-overlapping windings on the 12 stator teeth. The stator and rotor have a common center. The swirler has a circular motion. Thus, the swirler center rotates around the stator center with a radius of r. The stator teeth are aligned with the PMs when r is zero.

The solid and dashed curves in Fig. 3.1 show the flux generated by the PMs and

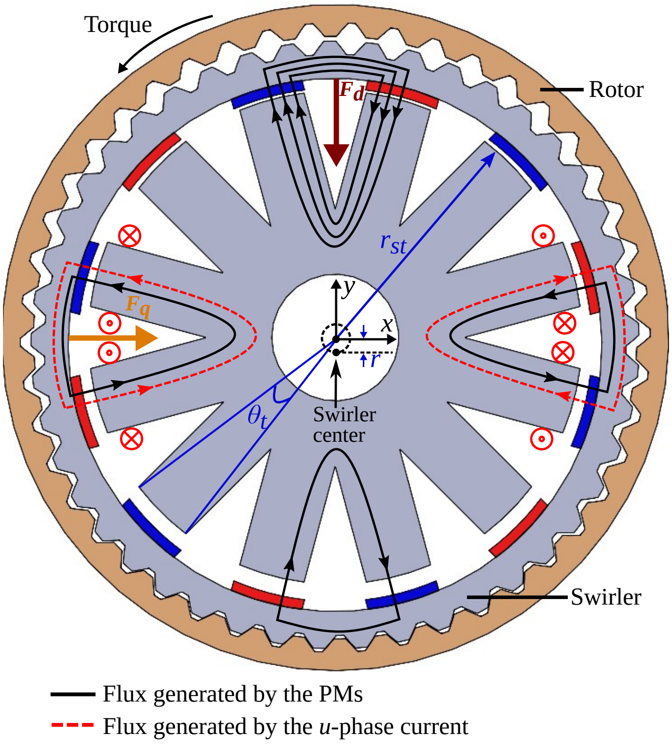

Fig. 3.1: Basic structure of the swirling actuator and schematic of the radial force and torque generation.

u-phase current, respectively. The swirler is eccentric in the negative y-direction. Thus, the air-gap length between the stator teeth and PMs is long in the negative y-direction, resulting in sparse air-gap PM flux. In contrast, the air-gap length is short in the y-direction, resulting in dense air-gap PM flux. As a result, a PM attractive force F_d in the negative y-direction is generated on the swirler. The F_d moves the swirler to the eccentric direction. When the u-phase windings are excited, the directions of the flux generated by the u-phase current are identical and opposite to the PM flux in the negative x-direction and x-direction, respectively. Thus, the unbalanced air-gap flux density generates a radial force F_q on the swirler in the x-direction. The F_q pushes the meshing gear teeth to generate a counterclockwise torque on the rotor.

Fig. 3.2 shows the operation of the swirling actuator. The three-phase AC currents are defined as

$$\begin{aligned} i_u &= I_s \cos(\omega_s t + \theta_i), \\ i_v &= I_s \cos(\omega_s t + \theta_i - \frac{2\pi}{3}), \\ i_w &= I_s \cos(\omega_s t + \theta_i + \frac{2\pi}{3}) \end{aligned} \tag{3.1}$$

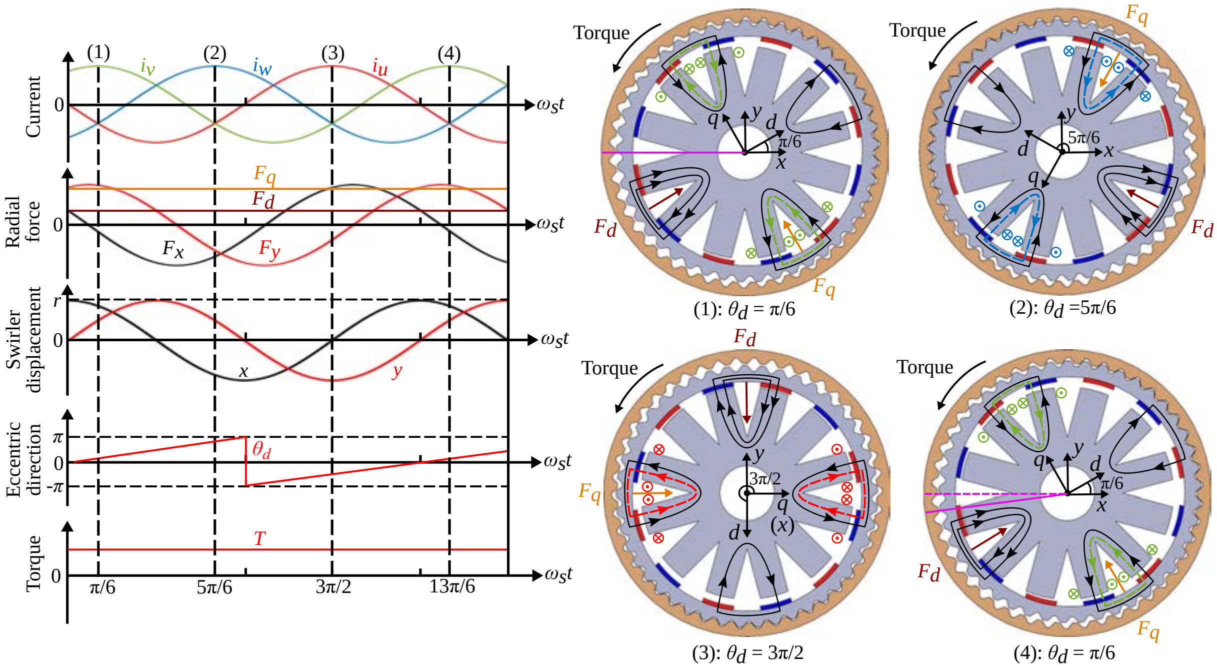

Fig. 3.2: Operation of the swirling actuator.

where I_s, ω_s and θ_i are the amplitude, angular frequency and initial phase shift of the currents. The θ_i is 90° in Fig. 3.2. The swirler circular motion frequency and current frequency are identical. The swirler circular motion can be decomposed into the x- and y-axis displacements x and y. Thus, x and y are given as

$$
\begin{aligned}
x &= r\cos\theta_d, \\
y &= r\sin\theta_d
\end{aligned}
\tag{3.2}
$$

where θ_d is the eccentric direction angle of the swirler. For simplification, θ_d is assumed to be 0° when $t = 0$ in the analytical derivations. Thus, θ_d is given as

$$
\theta_d = \omega_s t. \tag{3.3}
$$

Based on θ_d, a rotational dq coordinate system is established. The d-axis is in the eccentric direction of the swirler and the q-axis is perpendicular to the d-axis. The directions of the d- and q-axis forces F_d and F_q rotate with θ_d, whereas their amplitudes are constant. In Fig. 3.2, the rotor gear has one more tooth than the swirler gear. After one electric period, the rotor only rotates for an angle of one gear tooth as shown by the purple solid lines.

When the swirler has a circular motion with the radius r and the angular speed of ω_s, the mechanical power of the swirler is given as

$$P_{sw} = F_q \omega_s r. \tag{3.4}$$

The radius r of the swirler circular motion is limited by the mechanical structure. The maximum value of r is defined as r_0. When $r = r_0$, the swirler mechanical power P_{sw} is maximized.

The output mechanical power of the rotor is given as

$$P_r = \omega_r T \tag{3.5}$$

where ω_r is the rotor angular speed and T is the output torque. The mechanical efficiency is defined as

$$\eta_m = \frac{P_r}{P_{sw}}. \tag{3.6}$$

The power loss between P_r and P_{sw} is mainly the friction loss on the gear teeth.

Let us define the gear efficiency as

$$\eta_g = \frac{P_r}{P_{sw}|_{r=r_0}}. \tag{3.7}$$

Then, the output torque T is derived as

$$T = \eta_g F_q r_0 \frac{\omega_s}{\omega_r}. \tag{3.8}$$

The relationship between η_m is η_g is

$$\eta_g = \eta_m \frac{r}{r_0}. \tag{3.9}$$

The transmission ratio between ω_s and ω_r is presented by the swirler tooth number

Z_{sw} and rotor tooth number Z_r as

$$G = \frac{\omega_s}{\omega_r} = \frac{Z_r}{Z_r - Z_{sw}}. \tag{3.10}$$

The transmission ratio is identical to that of the cycloidal drive with rotating rollers. In the proposed actuator, the tooth number difference $(Z_r - Z_{sw})$ is set as 1 to obtain the maximum transmission ratio.

It should be noted that the outer-rotor structure is adopted in the proposed swirling actuator. The gear teeth are on the outer surface of the swirler. In contrast, the gear teeth will be on the inner surface of the swirler if an inner-rotor structure is chosen. Thus, the outer-rotor structure has more gear teeth and a larger transmission ratio.

3.3 Design of Electromagnetic Part

Using Maxwell's stress tensor method, the radial force components on the swirler in the static xy coordinate system are given as [91, 92]

$$\begin{aligned} F_x &= -\frac{r_{st} l_s}{2\mu_0} \int_{-\pi}^{\pi} B^2(\theta_s) \cos\theta_s d\theta_s, \\ F_y &= -\frac{r_{st} l_s}{2\mu_0} \int_{-\pi}^{\pi} B^2(\theta_s) \sin\theta_s d\theta_s \end{aligned} \tag{3.11}$$

where μ_0 is the permeability of vacuum, θ_s is the mechanical angular position in the static xy coordinate system, $B(\theta_s)$ is the radial air-gap flux density, r_{st} is the stator inner radius and l_s is the stack length. The minus symbols indicates that F_x and F_y are on the outer swirler.

It can be derived from (3.11) that two spatial harmonics in $B(\theta_s)$ can generate non-zero resultant radial force if their order difference is 1. Let us define B_{rm} and B_{ri} as the radial air-gap flux densities generated by the PMs and winding currents respectively. The total radial air-gap flux density B is then given as

$$B = B_{rm} + B_{ri}. \tag{3.12}$$

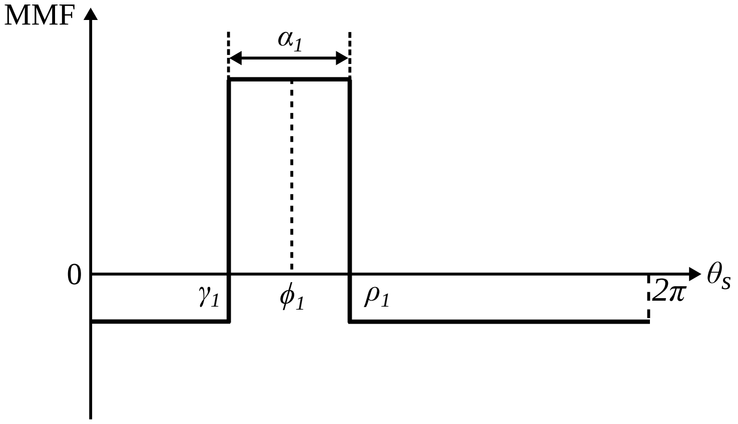

Fig. 3.3: MMF of a single coil of a set of non-overlapping windings.

To analyze the spatial harmonics of B_{rm} or B_{ri}, it is essential to investigate the magneto motive force (MMF) distribution. The MMF generated by the PMs is relatively simple. Thus, this section will focus on the design of stator windings.

3.3.1 MMF Vector Diagram

Let us first consider a single coil of a set of stator windings with N_s turns and a coil span of α_1. The mechanical angular positions of the two coil sides and the symmetrical axis are γ_1, ρ_1 and ϕ_1 respectively. The three position angles satisfy

$$\frac{\gamma_1 + \rho_1}{2} = \phi_1, \rho_1 - \gamma_1 = \alpha_1. \tag{3.13}$$

Assuming that a current i flows into the single coil, the resultant MMF distribution A is shown in Fig. 3.3 and is given as

$$A = \begin{cases} N_s i(1 - \frac{\alpha_1}{2\pi}) & \gamma_1 \leq \theta_s \leq \rho_1 \\ -N_s i(\frac{\alpha_1}{2\pi}) & 0 \leq \theta_s < \gamma_1 \text{ or } \rho_1 < \theta_s < 2\pi. \end{cases} \tag{3.14}$$

The Fourier series expansion of A is

$$A = a_0 + \sum_1^n (a_n \cos n\theta_s + b_n \sin n\theta_s) \tag{3.15}$$

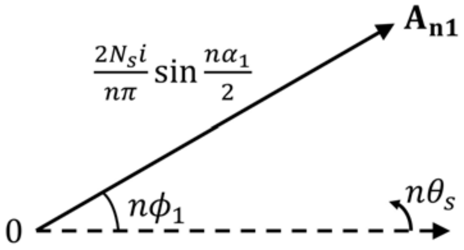

Fig. 3.4: MMF vector of the n^{th} spatial harmonic from a single coil.

where

$$
\begin{aligned}
a_0 = 0, a_n &= \frac{1}{\pi}\int_0^{2\pi} A_1 \cos n\theta_s d\theta_s \\
b_n &= \frac{1}{\pi}\int_0^{2\pi} A_1 \sin n\theta_s d\theta_s.
\end{aligned}
\tag{3.16}
$$

By using (3.13) and (3.14), the coefficients a_n and b_n can be calculated as

$$
\begin{aligned}
a_n &= \frac{2N_s i}{n\pi}\sin\frac{n\alpha_1}{2}\cos n\phi_1 \\
b_n &= \frac{2N_s i}{n\pi}\sin\frac{n\alpha_1}{2}\sin n\phi_1.
\end{aligned}
\tag{3.17}
$$

With (3.17), the n^{th} spatial harmonic of A is given as

$$
A_{n1} = a_n \cos n\theta_s + b_n \sin n\theta_s = \frac{2N_s i}{n\pi}\sin\frac{n\alpha_1}{2}\cos(n\theta_s - n\phi_1). \tag{3.18}
$$

Thus, the n^{th} spatial harmonic of A can be represented by a MMF vector $\mathbf{A_{n1}}$ with the amplitude of $\frac{2N_s i}{n\pi}\sin\frac{n\alpha_1}{2}$ and the phase of $n\phi_1$ based on the electrical angular position $n\theta_s$, as shown in Fig. 3.4. An arbitrary n^{th} spatial harmonic in the total MMF distribution can be evaluated by the superposition of MMF vectors of all coils.

Fig. 3.5 shows two common MMF vector diagrams of a certain n^{th} spatial harmonic when three-phase AC currents flow into the stator windings. The three MMF vectors $\mathbf{A_{nu}}$, $\mathbf{A_{nv}}$ and $\mathbf{A_{nw}}$ are generated by the u-phase, v-phase and w-phase windings respectively. $\mathbf{A_{nu}}$, $\mathbf{A_{nv}}$ and $\mathbf{A_{nw}}$ are separated from each other by $\frac{2\pi}{3}$. In Fig. 3.5(a) they are in positive sequence (uvw), whereas in Fig. 3.5(b) they are in negative sequence (uwv). The θ_n is the electrical angular position of the u-phase MMF vector $\mathbf{A_{nu}}$. Let us assume that all the coils have the same turn number N_s and coil span α_1, then the n^{th} spatial harmonics

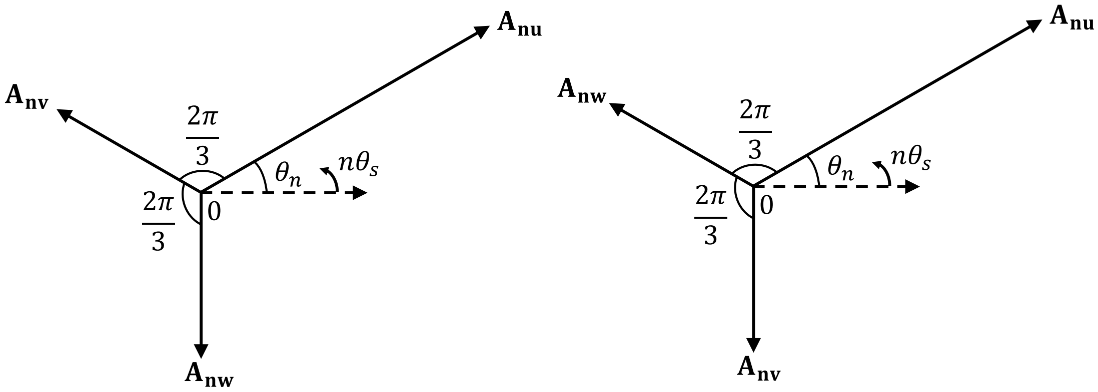

(a) (b)

Fig. 3.5: MMF vector diagram of the n^{th} spatial harmonic with three-phase AC currents. (a) Positive sequence; (b) negative sequence.

from each phase in Fig. 3.5(a) are defined as

$$\begin{aligned} A_{nu} &= k_n i_u \cos(n\theta_s - \theta_n) \\ A_{nv} &= k_n i_v \cos(n\theta_s - \theta_n - \frac{2\pi}{3}) \\ A_{nw} &= k_n i_v \cos(n\theta_s - \theta_n + \frac{2\pi}{3}) \end{aligned} \tag{3.19}$$

where k_n is the coefficient of the n^{th} spatial harmonic. The resultant n^{th} spatial harmonic A_n is calculated by (3.19) and (3.1) as

$$A_n = A_{nu} + A_{nv} + A_{nw} = \frac{3}{2} k_n I_s \cos\left[n\theta_s - (\omega_s t + \theta_i + \theta_n)\right]. \tag{3.20}$$

Thus, in the case of the MMF vector diagram in Fig. 3.5(a), the n^{th} MMF spatial harmonic rotates in counterclockwise direction with a constant amplitude. The initial phase is $\theta_i + \theta_n$. Similarly, in the case of Fig. 3.5(b), the calculated result of A_n is

$$A_n = \frac{3}{2} k_n I_s \cos\left[n\theta_s - (-\omega_s t - \theta_i + \theta_n)\right]. \tag{3.21}$$

Here the n^{th} MMF spatial harmonic rotates in clockwise direction and the initial phase is $-\theta_i + \theta_n$.

To summarize, with the MMF vector diagram, we can evaluate the existence of an arbitrary n^{th} MMF spatial harmonic by checking $\mathbf{A_{nu}}$, $\mathbf{A_{nv}}$ and $\mathbf{A_{nw}}$ for a set of three-phase

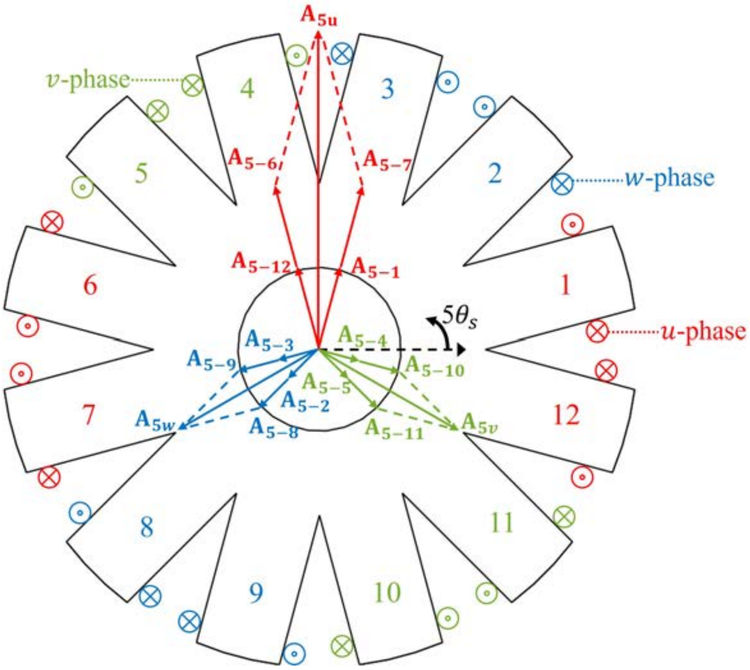

Fig. 3.6: MMF vector diagram of the 5^{th} spatial harmonic generated by the currents.

AC windings. The superposition of $\mathbf{A_{nu}}$, $\mathbf{A_{nv}}$ and $\mathbf{A_{nw}}$ indicates the amplitude, rotating direction and spatial phase of the n^{th} spatial harmonic, which are essential information to calculate the air-gap flux density and other associated quantities.

3.3.2 Design of 12-slot Non-Overlapping Double-Layer Windings

Since the 12-pole surface-mounted PMs mainly generate the 6^{th} MMF spatial harmonic, to have an order difference of 1 to generate the net radial force, the 5^{th} and 7^{th} spatial harmonics are expected in the MMF generated by the winding currents.

Non-overlapping double-layer windings are adopted in the actuator to shorten the end-windings. With short end-windings, a flat structure is feasible and the copper loss is reduced. The coil span α of a 12-slot on-overlapping windings is $\frac{\pi}{6}$.

Fig. 3.6 and Fig. 3.7 show the MMF vector diagrams of the 5^{th} spatial harmonic A_5 and the 7^{th} spatial harmonic A_7 of the designed windings. $\mathbf{A_{5-j}}$ $(j = 1, 2, ...12)$ indicates the MMF vector of the 5^{th} spatial harmonic generated by the j^{th} coil. For example, the mechanical angular position of the 1^{st} coil is $\pi/12$, then the electrical angular position

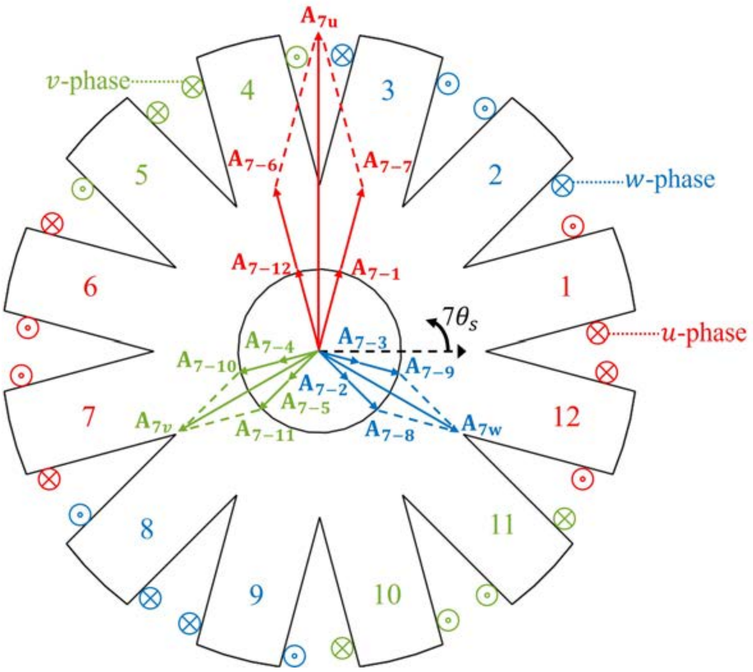

Fig. 3.7: MMF vector diagram of the 7^{th} spatial harmonic generated by the currents.

of $\mathbf{A_{5-1}}$ is $5\pi/12$. Since the $u-$phase winding consists of the 1^{st}, the 6^{th}, the 7^{th} and the 12^{th} coils, the phase MMF vector $\mathbf{A_{u5}}$ is the vector sum of $\mathbf{A_{5-1}}$, $\mathbf{A_{5-6}}$, $\mathbf{A_{5-7}}$ and $\mathbf{A_{5-12}}$. According to (3.18), the identical amplitude of $\mathbf{A_{5-1}}$, $\mathbf{A_{5-6}}$, $\mathbf{A_{5-7}}$ and $\mathbf{A_{5-12}}$ is $\frac{2N_s i_u}{5\pi}\sin\frac{5\alpha}{2}$. Thus, the coefficient k_5 is calculated as

$$k_5 = \frac{2N_s}{5\pi}\sin\frac{5\alpha}{2} \times 4 \times \cos\frac{\pi}{12} = \frac{8N_s}{5\pi}\cos^2(\frac{\pi}{12}). \tag{3.22}$$

The $v-$phase and $w-$phase MMF vectors $\mathbf{A_{v5}}$ and $\mathbf{A_{w5}}$ are built similarly. It can be observed that $\mathbf{A_{u5}}$, $\mathbf{A_{v5}}$ and $\mathbf{A_{w5}}$ are in the negative sequence, which indicates that the 5^{th} spatial harmonic A_5 rotates in the clockwise direction. The electrical position of $\mathbf{A_{u5}}$ is $\frac{\pi}{2}$. Thus, based on (3.21), A_5 can be given as

$$A_5 = \frac{3}{2}k_5 I_s \cos[5\theta_s - (-\omega_s t - \theta_i + \frac{\pi}{2})] = A_{i5}\sin(5\theta_s + \omega_s t + \theta_i) \tag{3.23}$$

where

$$A_{i5} = \frac{12}{5\pi}\cos^2(\frac{\pi}{12})N_s I_s. \tag{3.24}$$

In contrast, the phase MMF vectors $\mathbf{A_{u7}}$, $\mathbf{A_{v7}}$ and $\mathbf{A_{w7}}$ are in the positive sequence. Thus, A_7 rotates in counterclockwise direction. The electrical angular position of $\mathbf{A_{u7}}$ is $\frac{\pi}{2}$. Based on (3.20), it is given as

$$A_7 = \frac{3}{2}k_7 I_s \cos\left[7\theta_s - (\omega_s t + \theta_i + \frac{\pi}{2})\right] = A_{i7}\sin\left(7\theta_s - \omega_s t - \theta_i\right) \tag{3.25}$$

where

$$A_{i7} = \frac{12}{7\pi}\cos^2\left(\frac{\pi}{12}\right)N_s I_s. \tag{3.26}$$

It should be noted that the adopted winding configuration is not the only choice to generate the 5^{th} and 7^{th} MMF spatial harmonics. From the MMF vector diagrams. the distribution factors of the 5^{th} and 7^{th} harmonics can be calculated as $\cos(\pi/12) = 0.966$. Moreover, from (3.18), the pitch factors of the 5^{th} and 7^{th} harmonics are $\sin(5\pi/12) = 0.966$ and $\sin(7\pi/12) = 0.966$ respectively. The resultant winding factors of the 5^{th} and 7^{th} harmonics are 0.933, which are the highest among all the possible configurations.

3.4 Analysis of Electromagnetic Radial Force

3.4.1 Derivation of Air-gap Flux Density

Let us define the MMF generated by the PMs as $A_m(\theta_s)$. It can be approximated by the dominant 6^{th} spatial harmonic as

$$A_m(\theta_s) \approx -A_{m6}\sin 6\theta_s, \tag{3.27}$$

where the amplitude A_{m6} is derived as

$$A_{m6} = \frac{4B_R t_m}{\pi\mu_0\mu_r}, \tag{3.28}$$

where B_R, μ_r and t_m are the residual flux density, relative permeability and thickness of the PMs, respectively. Based on Chapter 3.3.2, the MMF generated by the winding currents can be approximated as

$$A_i(\theta_s) \approx A_{i5}\sin(5\theta_s + \omega_s t + \theta_i) + A_{i7}\sin(7\theta_s - \omega_s t - \theta_i). \tag{3.29}$$

Since the PMs are aligned with the stator teeth, the air-gap radial flux density under the stator slots is neglected. Thus, let us define the permeance coefficient function $P(\theta_s)$ to describe the slot effect as

$$P(\theta_s) = \begin{cases} 1, & (\frac{2k-1}{12})\pi - \frac{\theta_t}{2} < \theta_s < (\frac{2k-1}{12})\pi + \frac{\theta_t}{2} \\ 0, & (\frac{2k-3}{12})\pi - \frac{\theta_t}{2} < \theta_s < (\frac{2k-1}{12})\pi - \frac{\theta_t}{2} \end{cases} \tag{3.30}$$

where θ_t is the span angle of the stator teeth and $k = 1, 2, ..., 12$.

The eccentric swirler leads to a non-uniform air-gap length $g(\theta_s)$ which is derived as

$$g(\theta_s) \approx g_0 + r\cos(\theta_s - \theta_d) \tag{3.31}$$

where the nominal air-gap length g_0 is defined as the air-gap length when the swirler is concentric with the stator. Then, if the reluctance of the stator core and the swirler core is neglected, the air-gap radial flux densities $B_{rm}(\theta_s)$ and $B_{ri}(\theta_s)$ generated by the PMs and currents are given as

$$B_{rm}(\theta_s) = \frac{\mu_0 A_m(\theta_s)P(\theta_s)}{g(\theta_s) + t_m/\mu_r}, \tag{3.32}$$

$$B_{ri}(\theta_s) = \frac{\mu_0 A_i(\theta_s)P(\theta_s)}{g(\theta_s) + t_m/\mu_r}. \tag{3.33}$$

The non-uniform air-gap length $g(\theta_s)$ leads to the permeance variation and introduces extra orders of spatial harmonics in the air-gap flux densities. From (3.31), the function $1/[g(\theta_s + t_m/\mu_r)]$ in (3.32) and (3.33) is approximated as

$$\frac{1}{g(\theta_s) + t_m/\mu_r} \approx \frac{1}{g_e} - \frac{r\cos(\theta_s - \theta_d)}{g_e^2}, \tag{3.34}$$

where $g_e = g_0 + t_m/\mu_r$ is defined as the effective air-gap length. The accuracy of the approximation (3.34) will be good if r is much shorter than g_e. By substituting (3.27), (3.30) and (3.34) into (3.32), $B_{rm}(\theta_s)$ is derived as

$$B_{rm}(\theta_s) \approx -\frac{\mu_0 \sin 3\theta_t}{g_e} A_{m6} \sin 6\theta_s + \frac{\mu_0 \sin 3\theta_t}{2g_e^2} r A_{m6}[\sin(5\theta_s + \theta_d) + \sin(7\theta_s - \theta_d)]. \tag{3.35}$$

The extra 5^{th} and 7^{th} harmonics related to r are generated in $B_{rm}(\theta_s)$. By substituting (3.29), (3.30) and (3.34) into (3.33), $B_{ri}(\theta_s)$ is derived as

$$B_{ri}(\theta_s) \approx \frac{\mu_0}{g_e \cos\frac{\pi}{12}}[A_{i5} \sin\frac{5\theta_t}{2} \sin(5\theta_s + \omega_s t + \theta_i) + A_{i7} \sin\frac{7\theta_t}{2} \sin(7\theta_s - \omega_s t - \theta_i)]. \tag{3.36}$$

3.4.2 Derivation of Radial Force

The 5^{th}, 6^{th}, and 7^{th} harmonics in $B_{rm}(\theta_s)$ and $B_{ri}(\theta_s)$ can generate the net radial force. By substituting (3.2), (3.12), (3.32) and (3.33) into the Maxwell stress equation (3.11), F_x and F_y are derived as

$$\begin{aligned} F_x &\approx \frac{\mu_0 \pi r_{st} l_s}{2g_e^2}[\frac{\sin^2 3\theta_t}{g_e} A_{m6}^2 x + \frac{\sin 3\theta_t}{\cos\frac{\pi}{12}} A_{m6}(A_{i5} \sin\frac{5\theta_t}{2} + A_{i7} \sin\frac{7\theta_t}{2}) \cos(\omega_s t + \theta_i)], \\ F_y &\approx \frac{\mu_0 \pi r_{st} l_s}{2g_e^2}[\frac{\sin^2 3\theta_t}{g_e} A_{m6}^2 y + \frac{\sin 3\theta_t}{\cos\frac{\pi}{12}} A_{m6}(A_{i5} \sin\frac{5\theta_t}{2} + A_{i7} \sin\frac{7\theta_t}{2}) \sin(\omega_s t + \theta_i)], \end{aligned} \tag{3.37}$$

The F_x and F_y can be transformed into the rotational dq coordinate system by using θ_d as

$$\begin{bmatrix} F_d \\ F_q \end{bmatrix} = \begin{bmatrix} \cos\theta_d & \sin\theta_d \\ -\sin\theta_d & \cos\theta_d \end{bmatrix} \begin{bmatrix} F_x \\ F_y \end{bmatrix}. \tag{3.38}$$

Thus, F_d and F_q are given as

$$\begin{aligned} F_d &\approx \frac{\mu_0 \pi r_{st} l_s \sin^2 3\theta_t}{2g_e^3} A_{m6}^2 r + \frac{\mu_0 \pi r_{st} l_s \sin^2 3\theta_t}{2g_e^2 \cos\frac{\pi}{12}} A_{m6}(A_{i5} \sin\frac{5\theta_t}{2} + A_i 7 \sin\frac{7\theta_t}{2}) \cos\theta_i, \\ F_q &\approx \frac{\mu_0 \pi r_{st} l_s \sin^2 3\theta_t}{2g_e^2 \cos\frac{\pi}{12}} A_{m6}(A_{i5} \sin\frac{5\theta_t}{2} + A_i 7 \sin\frac{7\theta_t}{2}) \sin\theta_i. \end{aligned} \tag{3.39}$$

It can be verified by (3.39) that F_d and F_q are constant with respect to time. The first term of F_d is the PM attractive force F_{dm} generated by the eccentric radius r. The second term of F_d and the F_q are the active forces generated by the interaction between the PMs and currents. The active forces are the functions of the initial current phase shift θ_i . The

F_q reaches the maximum at $\theta_i = 90°$. Note that both the 5^{th} and 7^{th} harmonics in the current-originated MMF $A_i(\theta_s)$ contribute significantly to the active forces.

The three-phase currents are also transformed into the static xy coordinate system and rotational dq coordinate system. The x-axis current i_x and the y-axis current i_y are given as

$$\begin{bmatrix} i_x \\ i_y \end{bmatrix} = \sqrt{\frac{2}{3}} \begin{bmatrix} 1 & -\frac{1}{2} & -\frac{1}{2} \\ 0 & -\frac{\sqrt{3}}{2} & -\frac{\sqrt{3}}{2} \end{bmatrix} \begin{bmatrix} i_u \\ i_v \\ i_w \end{bmatrix}. \tag{3.40}$$

By substituting (3.1) into (3.40), i_x and i_y are derived as

$$\begin{bmatrix} i_x \\ i_y \end{bmatrix} = \sqrt{\frac{3}{2}} I_s \begin{bmatrix} \cos{(\omega_s t + \theta_i)} \\ \sin{(\omega_s t + \theta_i)} \end{bmatrix}. \tag{3.41}$$

With the same transforming matrix in (3.38), the d- and q-axis currents i_d and i_q are derived as

$$\begin{bmatrix} i_d \\ i_q \end{bmatrix} = \sqrt{\frac{3}{2}} I_s \begin{bmatrix} \cos\theta_i \\ \sin\theta_i \end{bmatrix}. \tag{3.42}$$

Similar to the theory of magnetic bearings, let us define the displacement force factor k_d and the current force factor k_i. The product of k_d and the displacement r is the PM attractive force, whereas the products of k_i and the current components are the active forces. Thus, F_d and F_q are given by k_d and k_i as

$$\begin{bmatrix} F_d \\ F_q \end{bmatrix} = k_d \begin{bmatrix} r \\ 0 \end{bmatrix} + k_i \begin{bmatrix} i_d \\ i_q \end{bmatrix}. \tag{3.43}$$

The k_d and k_i can be derived as

$$\begin{aligned} k_d &= \frac{8 r_{st} l_s \sin^2 3\theta_t B_R^2 t_m^2}{\pi \mu_0 \mu_r^2 (g_0 + t_m/\mu_r)^3}, \\ k_i &= \frac{8\sqrt{6} N_s r_{st} l_s B_R t_m \sin 3\theta_t \cos\frac{\pi}{12}}{\pi \mu_r (g_0 + t_m/\mu_r)^2} (\frac{1}{5}\sin\frac{5\theta_t}{2} + \frac{1}{7}\sin\frac{7\theta_t}{2}). \end{aligned} \tag{3.44}$$

Equation (3.44) indicates that both k_d and k_i are constants. Thus, F_d and F_q have linear relationships with i_d and i_q respectively. A short nominal air-gap length g_0 is desirable to enhance k_d and k_i. The minimum g_0 should be larger than the designed radius r_0 of the circular motion.

By transforming (3.43) into the static xy coordinate system, F_x and F_y are also given by k_d and k_i as

$$\begin{bmatrix} F_x \\ F_y \end{bmatrix} = k_d \begin{bmatrix} x \\ y \end{bmatrix} + k_i \begin{bmatrix} i_x \\ i_y \end{bmatrix}. \tag{3.45}$$

3.4.3 Derivation of Back EMF

The analysis of the back electromotive force (EMF) helps understand the intrinsic principle of the power transmission in the swirling actuator. Fig. 3.8 shows the equivalent magnetic circuit of the PM flux with zero currents. The A_M is the amplitude of the MMF generated by PMs which is given as

$$A_M = \frac{B_R t_m}{\mu_0 \mu_r}. \tag{3.46}$$

The $P_j (j = 1, 2, ..., 12)$ represents the sum of the air-gap permeance and PM permeance facing the j^{th} stator tooth, which is given as

$$P_j = \int_{\frac{(2j-1)\pi}{12} - \frac{\theta_t}{2}}^{\frac{(2j-1)\pi}{12} + \frac{\theta_t}{2}} \frac{1}{\frac{g(\theta_s)}{\mu_0 r_s l_s d\theta_s} + \frac{t_m}{\mu_0 \mu_r r_s l_s d\theta_s}} = \int_{\frac{(2j-1)\pi}{12} - \frac{\theta_t}{2}}^{\frac{(2j-1)\pi}{12} + \frac{\theta_t}{2}} \frac{\mu_0 r_s l_s}{g(\theta_s) + t_m/\mu_r} d\theta_s. \tag{3.47}$$

By substituting the approximation (3.34) into (3.47), P_j is derived as

$$P_j \approx \frac{\mu_0 r_s l_s \theta_t}{g_e} - \frac{2\mu_0 r_s l_s r}{g_e^2} \sin\frac{\theta_t}{2} \cos\left[\frac{2(j-1)\pi}{12} - \theta_d\right]. \tag{3.48}$$

The flux through P_j is given as

$$\phi_j = A_M P_j. \tag{3.49}$$

Then, the back EMF generated by ϕ_j is given as

$$e_j = N_s \frac{d\phi_j}{dt} = N_s A_M \frac{dP_j}{dt}. \tag{3.50}$$

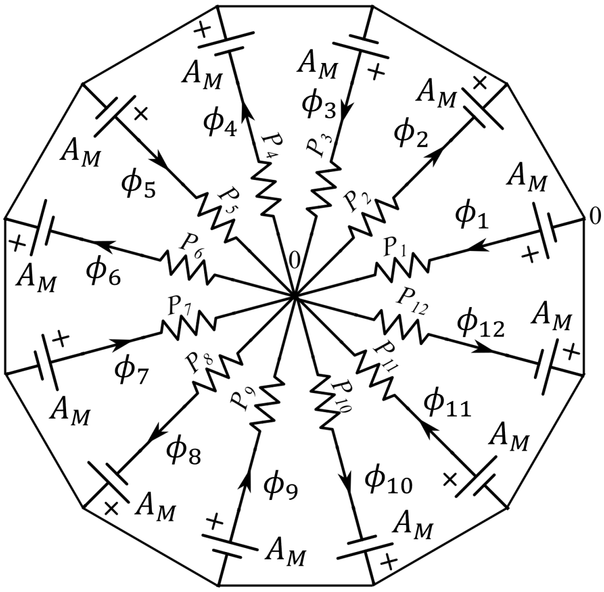

Fig. 3.8: Equivalent magnetic circuit of the PM flux with zero currents.

By substituting (3.3) and (3.48) into (3.50), e_j is derived as

$$e_j = \frac{2N_s A_M \mu_0 r_s l_s r}{g_e^2} \omega_s \sin\frac{\theta_t}{2} \sin[\omega_s t - \frac{2(j-1)\pi}{12}]. \tag{3.51}$$

Equation (3.51), the back EMF is proportional to the eccentric radius r and current frequency ω_s.

The phase back EMFs are given as

$$\begin{aligned} e_u &= e_6 + e_7 - e_1 - e_{12}, \\ e_v &= e_{10} + e_{11} - e_4 - e_5, \\ e_w &= e_2 + e_3 - e_8 - e_9. \end{aligned} \tag{3.52}$$

By (3.51), the phase back EMFs are derived as

$$\begin{aligned} e_u &= \frac{8N_s A_M \mu_0 r_s l_s r}{g_e^2} \omega_s \sin\frac{\theta_t}{2} \cos\frac{\pi}{12} \cos(\omega_s t + \frac{\pi}{2}), \\ e_v &= \frac{8N_s A_M \mu_0 r_s l_s r}{g_e^2} \omega_s \sin\frac{\theta_t}{2} \cos\frac{\pi}{12} \cos(\omega_s t - \frac{\pi}{6}), \\ e_w &= \frac{8N_s A_M \mu_0 r_s l_s r}{g_e^2} \omega_s \sin\frac{\theta_t}{2} \cos\frac{\pi}{12} \cos(\omega_s t + \frac{7\pi}{6}). \end{aligned} \tag{3.53}$$

Similar to the stator currents, the back EMFs are also transformed into the dq coordinate

Tab. 3.1: Specifications of the swirling actuator.

Symbol	Quantity	Value
D	Outer diameter [mm]	100
L	Axial length with end-windings [mm]	20
g_0	Nominal air-gap length [mm]	1
r_{st}	Stator inner radius [mm]	37
l_s	Stack length [mm]	13
t_m	PM thickness [mm]	2
r_0	Maximum eccentric radius [mm]	0.4
B_R	PM residual flux density [T]	1.4
N_s	Winding turn number per stator tooth	140
G	Transmission ratio	113

system as

$$e_d = 0, e_q = \frac{4\sqrt{6}N_s A_M \mu_0 r_s l_s r}{g_e^2}\omega_s \sin\frac{\theta_t}{2}\cos\frac{\pi}{12}. \tag{3.54}$$

It is shown the back EMF only has the q-axis component e_q. Thus, the q-axis current i_q generates the active power with e_q, whereas the d-axis current i_d generates the reactive power with e_q.

3.4.4 FEA Results

Tab. 3.1 lists the specifications of the developed swirling actuator. The nominal air-gap length g_0 is set as 1 mm, which is relatively long compared with the air-gap lengths of conventional electric machines with similar dimensions. A short air-gap length is avoided for the first prototype to confirm the principle. The maximum radius of the circular motion r_0 is 0.4 mm. Thus, the minimum air-gap length is 0.6 mm. The stator core is made of the laminated silicon steel 50JNE470. The swirler material is the ferromagnetic stainless steel SUS440C (ANSI 440C), whereas the rotor material is the stainless steel SUS304 (ANSI 304) with negligible permeability.

The analytical results of the air-gap flux density and radial force are verified with 3-D FEA. Fig. 3.9(a) shows the FEA results of $B_{rm}(\theta_s)$ and $B_{ri}(\theta_s)$ when the eccentric direction angle θ_d is -90°. The current amplitude I_s is 5.4 A and the phase $(\omega_s t + \theta_i)$ is 0°. The corresponding current density in the windings is 40 A/mm^2 which is the peak value for short-time operation. The amplitude of $B_{ri}(\theta_s)$ is lower than that of $B_{rm}(\theta_s)$ due to the limited winding turn number N_s and the long effective air-gap length g_e.

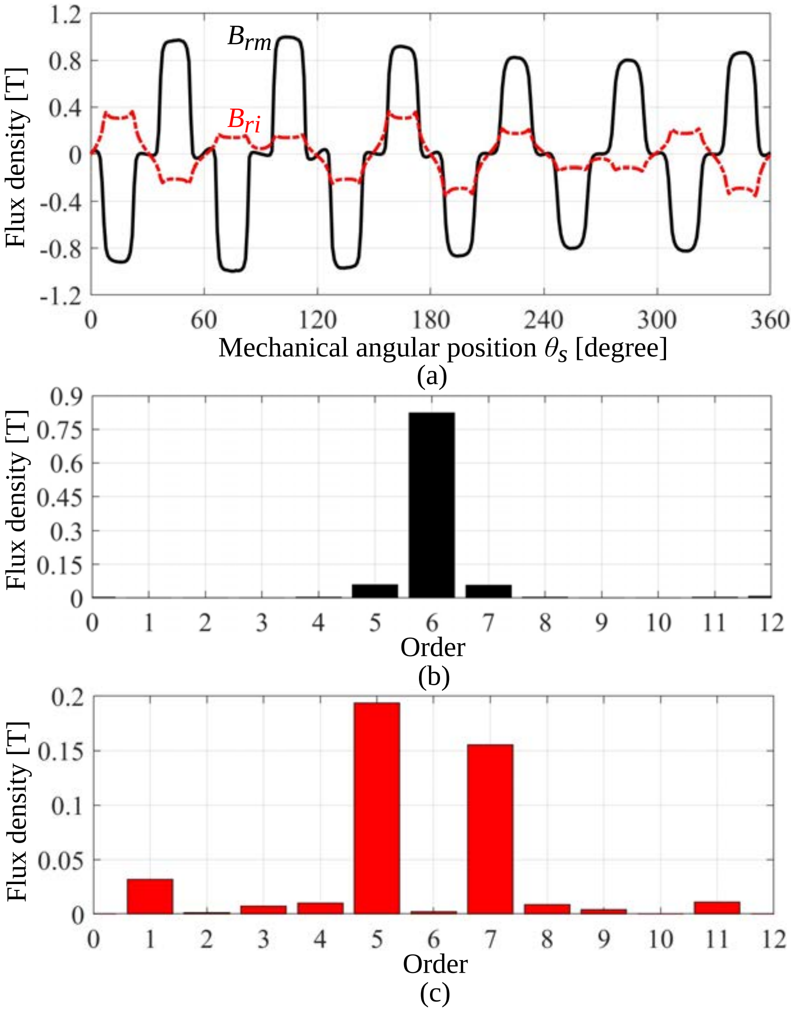

Fig. 3.9: (a) FEA results of $B_{rm}(\theta_s)$ and $B_{ri}(\theta_s)$. (b) Harmonic spectrum of $B_{rm}(\theta_s)$. (c) Harmonic spectrum of $B_{ri}(\theta_s)$.

The harmonic spectra of $B_{rm}(\theta_s)$ and $B_{ri}(\theta_s)$ are shown in Fig. 3.9(b) and Fig. 3.9(c), respectively. There are the 5^{th}, 6^{th} and 7^{th} harmonics in $B_{rm}(\theta_s)$ and the 5^{th} and 7^{th} harmonics in $B_{ri}(\theta_s)$, corresponding to the derived (3.35) and (3.36). The other harmonics have ignorable amplitudes. The small 3^{rd}, 4^{th}, 6^{th}, 8^{th}, and 9^{th} harmonics in $B_{ri}(\theta_s)$ are caused by the nonuniform air-gap length. The amplitudes are less than 0.01 T, which are negligible. The 1^{st} and 11^{th} harmonics in $B_{ri}(\theta_s)$ are caused by the 1^{st} and 11^{th} harmonics in the current MMF $A_i(\theta_s)$. They are not included in the analytical derivations because they do not contribute to the radial force.

Fig. 3.10 shows the radial force components F_x, F_y, F_d and F_q obtained by FEA and analytical equations with respect to time. The current frequency f_s , amplitude I_s and initial current phase shift θ_i are 10 Hz, 5.4 A and 90°, respectively. The F_x and F_y are

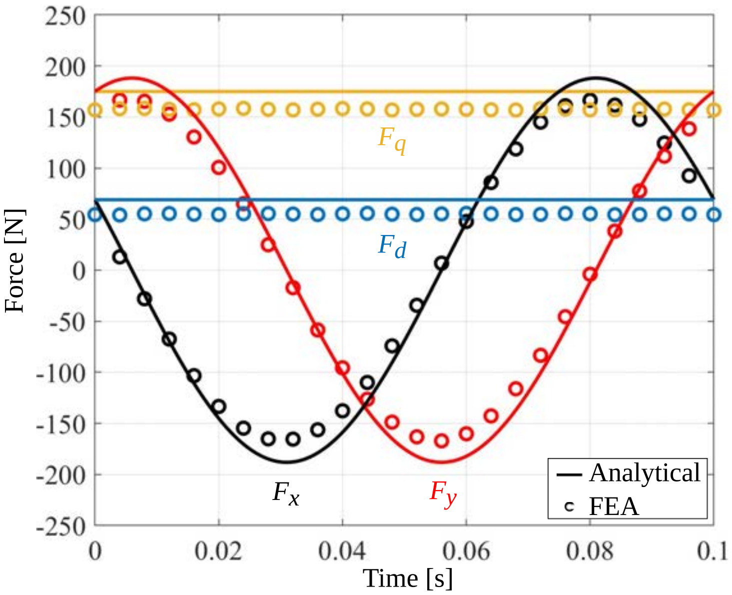

Fig. 3.10: FEA and analytical results of the radial force components with respect to time.

sinusoidal, and F_d and F_q are almost constant with negligible ripples.

Fig. 3.11 shows F_d and F_q given by FEA and analytical equations with respect to the initial current phase shift θ_i. The current amplitude I_s is 5.4 A. To drive the actuator with positive rotation speed, non-negative d-axis current i_d and positive q-axis current i_q are provided, corresponding to $0° < \theta_i \leq 90°$ in Fig. 3.11. When $\theta_i = 90°$, i_d is zero and i_q is maximized. Thus, F_d only consists of the PM attractive force F_{dm} and the active force only contributes to F_q. Intuitively, this operation point can generate the highest torque.

It should be noted that the force amplitudes of the FEA results are lower than those of the analytical results in Fig. 3.10 and Fig. 3.11. The discrepancy is mainly caused by omitting the swirler reluctance in the analytical derivation. The swirler material stainless steel 440C has a high hardness that is suitable for the gear structure. However, the maximum relative permeability of SUS440C (ANSI 440C) is about 300 and its saturation flux density is lower than 1.5 T. Thus, the reluctance is high compared with the laminated silicon steel.

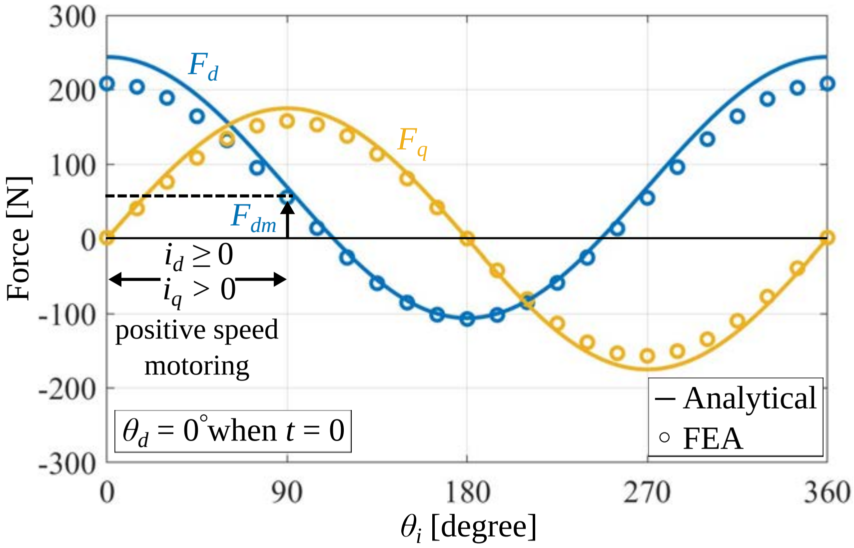

Fig. 3.11: FEA and analytical results of the radial force components with respect to the initial current phase shift θ_i.

3.5 Experiments of Preliminary Prototype

The first prototype was built to evaluate the radial force and torque. Fig. 3.12(a) shows the swirler and rotor gear. Fig. 3.12(b) shows the complete prototype for the torque measurement. The configuration for the radial force evaluation is slightly different and will be introduced in the next section.

3.5.1 Radial Force Measurement

Fig. 3.13 shows the schematic for measuring the static radial force. The rotor gear is not included in the radial force measurement. The x- and y-axis displacements x and y are measured by two eddy-current-type displacement sensors. Two sensor targets are fixed to the swirler and shifted by 90°. To limit the displacement of the swirler, there are three pins fixed to the frame and inserted into the swirler holes. The diameters of the frame holes, swirler holes and pins are defined as D_{hf}, D_{hsw} and D_p, respectively. In the radial force measurement, D_{hf} is equal to D_p. The maximum eccentric radius r_0 of the swirler is given by

$$r_0 = (D_{hsw} - D_p)/2. \tag{3.55}$$

In Fig. 3.13, D_{hsw} is 2.8 mm, and D_p is 2.4 mm. As a result, r_0 is 0.2 mm.

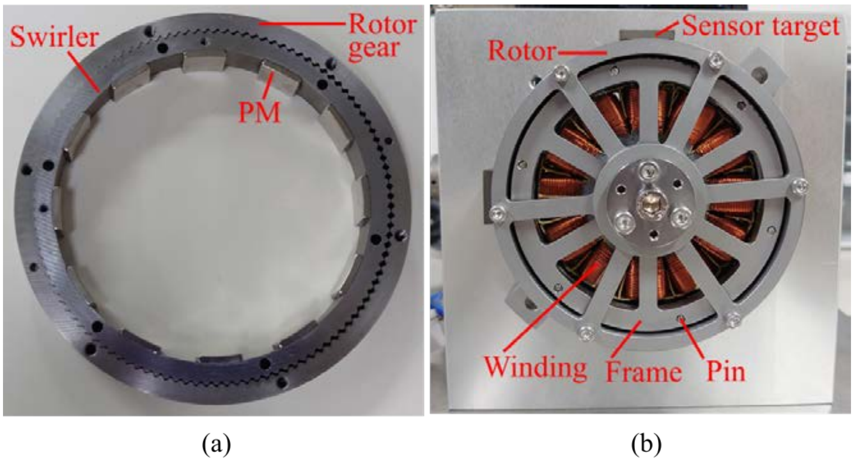

Fig. 3.12: (a) Swirler and rotor. (b) Complete prototype.

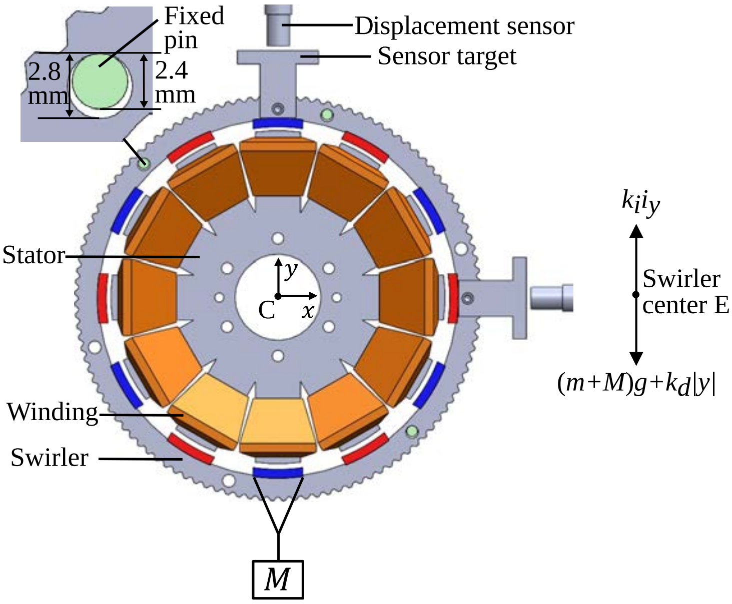

Fig. 3.13: Schematic of the static radial force measurement.

The swirler weight m is 0.16 kg. The external weight M is applied to the swirler through thin nylon wires. The swirler is pulled by M to the touchdown position in the negative y-direction. Thus, the PM attractive force is generated in the negative y-direction, which is given by $k_d|y|$. On the contrary, the y-axis current i_y generates the active y-axis force F_{yi}, which is given by $k_i i_y$. If F_{yi} is large enough, the swirler moves upwards. When i_y reaches the minimum value to move the swirler upwards, F_{yi} is equal to the sum of the PM attractive force $k_d|y|$ and the gravity of the swirler and the external weight. The force relationship is given as

$$F_{yi} = k_i i_y = (m + M)g + k_d|y|. \tag{3.56}$$

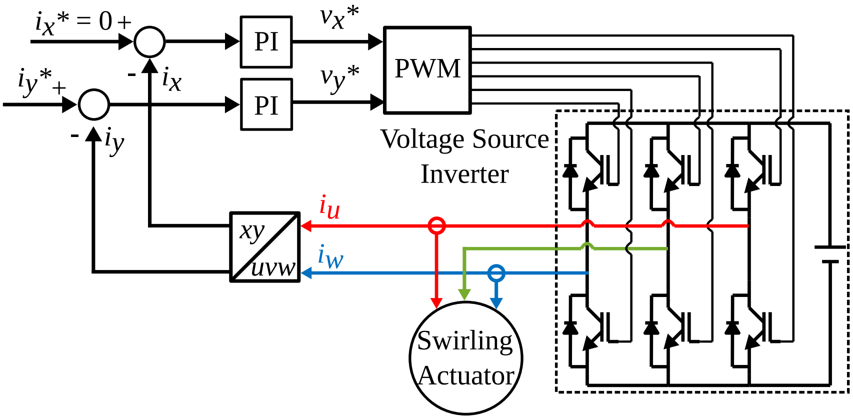

Fig. 3.14: Control block diagram for the force measurement.

Tab. 3.2: Parameters related to actuator control.

Phase resistance [Ω]	6.4
Phase inductance [mH]	12
Input DC voltage of VSI [V]	100
Switching frequency [kHz]	10
Proportional gain of current controller k_p	25
Integral gain of current controller	12500

The y-axis current i_y and y-axis displacement y can be measured directly. At least two sets of measurement are necessary to identify the force factors by (3.56). Let us define i_{y1} and i_{y2} as the minimum y-axis currents to move the swirler with the external weights M_1 and M_2, respectively. The initial y-axis displacement y is identical in all the measurements. Then, the displacement force factor k_d is given as

$$k_d = \frac{(M_2 - M_1)g}{(i_{y2} - i_{y1})|y|} i_{y1} - \frac{(m + M_1)g}{|y|}. \tag{3.57}$$

In the experiment, k_d is calculated by (3.57) at $M_1 = 0$ and $M_2 = 1$ kg. Next, the active y-axis force F_{yi} is obtained by the sum of $(m + M)g$ and $k_d|y|$, as shown in the right side of (3.56). The external weight M is changed from 0 to 13 kg with a step of 1 kg. An average k_i is obtained from the 14 sets of measurement.

Fig. 3.14 shows the control block diagram of the swirling actuator for the force measurement. The x- and y-axis currents i_x and i_y are controlled by two proportional-integral (PI) controllers. The reference x-axis current i_x^* is always zero. The u-phase and w-phase currents i_u and i_w are measured and transformed into i_x and i_y to compare with the reference i_x^* and i_y^*. The outputs of the PI controllers are the x- and y-axis voltage commands

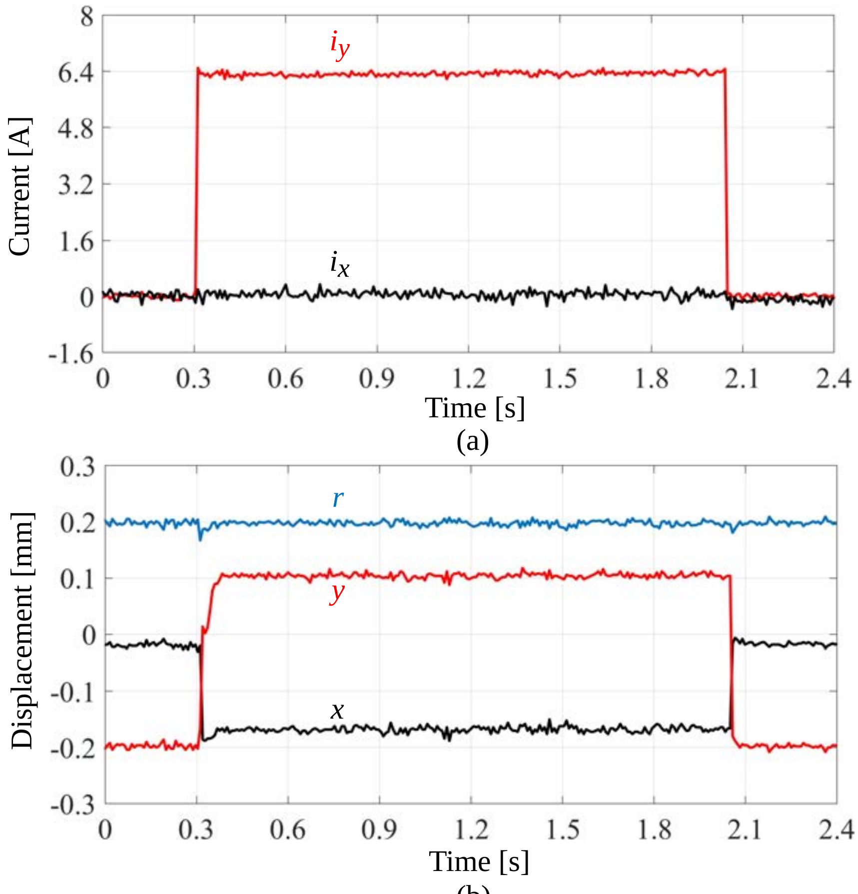

(a)

(b)

Fig. 3.15: Measured results of (a) x- and y-axis currents i_x and i_y; (b) x-axis displacement x, y-axis displacement y, and radius r of swirler displacement.

v_x^* and v_y^*. A three-phase voltage source inverter generates the output voltage based on v_x^* and v_y^* by the pulse width modulation (PWM). The control is implemented on a digital signal processor (TMS320F28335). Tab. 3.2 lists the parameters related to the actuator control. The phase inductance is measured when the swirler is concentric with the stator.

Fig. 3.15 shows the waveforms of the measured displacements and currents during the experiment with the external weight M of 13 kg. The measured eccentric radius r of the swirler is given by

$$r = \sqrt{x^2 + y^2}. \tag{3.58}$$

At the initial touchdown condition, y is about -0.2 mm and x is close to zero. When the y-axis current i_y changes from 0 to 6.4 A, the force F_{yi} overcomes the force in the negative y-direction. Thus, the swirler moves upwards to the new touchdown position where $y \approx 0.1$ mm. Since x is not exactly zero at the initial touchdown position, the

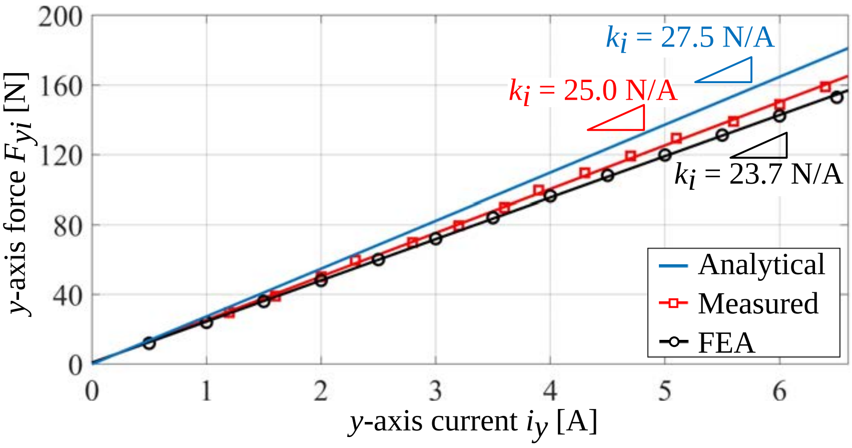

Fig. 3.16: Comparison of analytical, measured and FEA results of the y-axis force F_{yi} with respect to the y-axis current i_y.

x-axis attractive force makes the swirler move also in the negative x-direction. When i_y returns to zero, the external weight M pulls the swirler back to the initial touchdown position in the negative y-direction. The eccentric radius r of the swirler is always 0.2 mm at touchdown positions.

Fig. 3.16 shows the results of y-axis force F_{yi} with respect to the y-axis current i_y from the analytical calculation, FEA and measurement. The F_{yi} shows a good linearity with i_y. The average current force factor k_i are 27.5 N/A, 23.7 N/A and 25.0 N/A from the analytical calculation, FEA and measurement, respectively. The k_i from the analytical calculation and FEA are 10% high and 5% low with respect to the measured k_i. The k_d are 167 N/mm, 139 N/mm and 146 N/mm from the analytical calculation, FEA and measurement, respectively. The k_d from the analytical calculation and FEA are 14% high and 5% low with respect to the measured k_d. Reasonable correspondences are seen. Thus, it is verified that the radial force is generated as expected.

3.5.2 Torque Measurement

The mechanical structure for implementing the circular motion of the swirler is essential for the operation of the swirling actuator. Fig. 3.17(a) shows the bottom view of the prototype including the mechanical parts. Fig. 3.17(b) shows the cross-sectional views at section A-A' indicated in Fig. 3.17(a). Fig. 3.17(c) shows the configuration of an arbitrary pin. It can be seen that six pins go through the frames and swirler and prevent

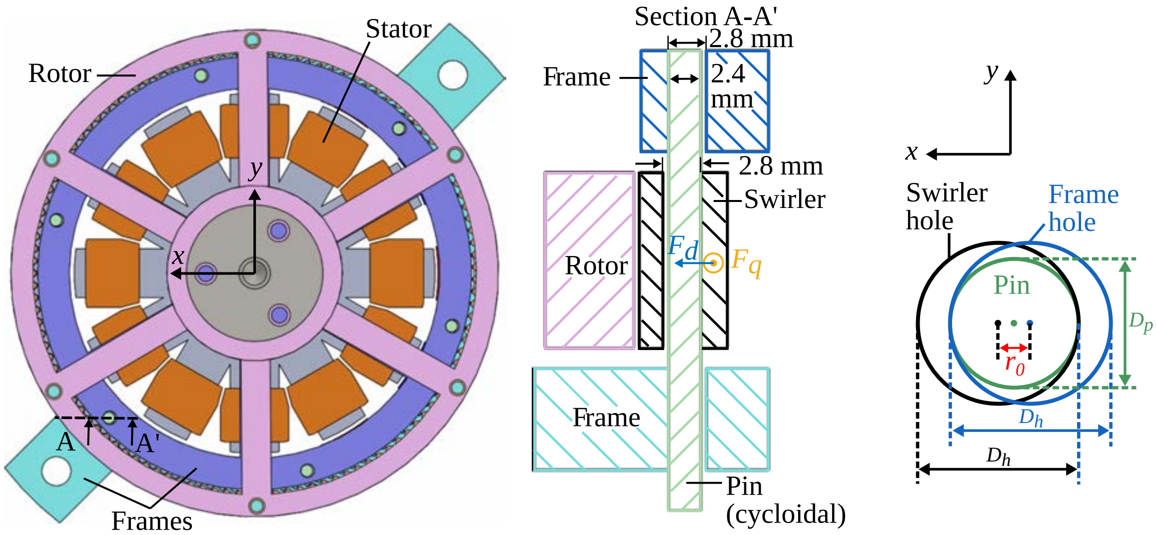

(a) (b) (c)

Fig. 3.17: (a) Bottom view of the prototype; (b) cross-sectional views of A-A'; (c) pin configuration.

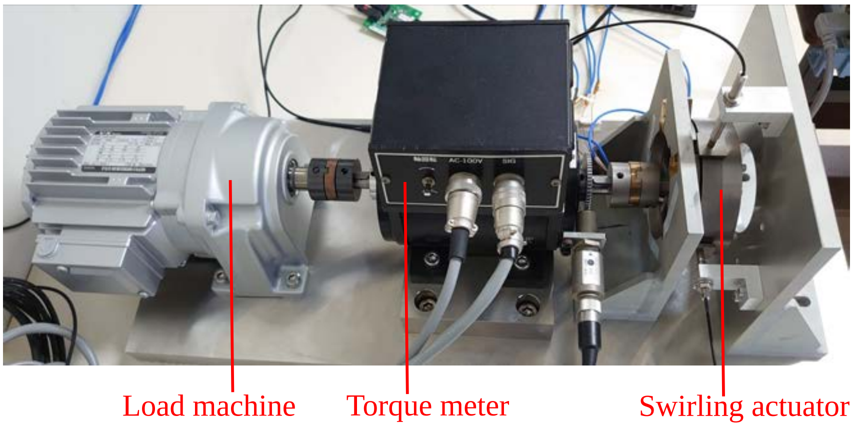

Fig. 3.18: Test bench of the torque measurement.

the rotation of the swirler. Unlike in the radial force measurement, the pins are not fixed, but have the cycloidal motion in the torque measurement. Since the movement between the swirler and pins is rolling but not sliding, the friction loss is low and a smooth circular motion of the swirler is realized. The diameters of frame holes and swirler holes are both D_h. As shown in Fig. 3.17(c), the center distance between the frame holes and swirler holes is the eccentric radius of the swirler. To restrict the maximum eccentric radius to r_0, D_h and D_p need to satisfy

$$D_h - D_p = r_0. \tag{3.59}$$

In Fig. 3.17(b), D_h is 2.8 mm and D_p is 2.4 mm. As a result, r_0 is 0.4 mm.

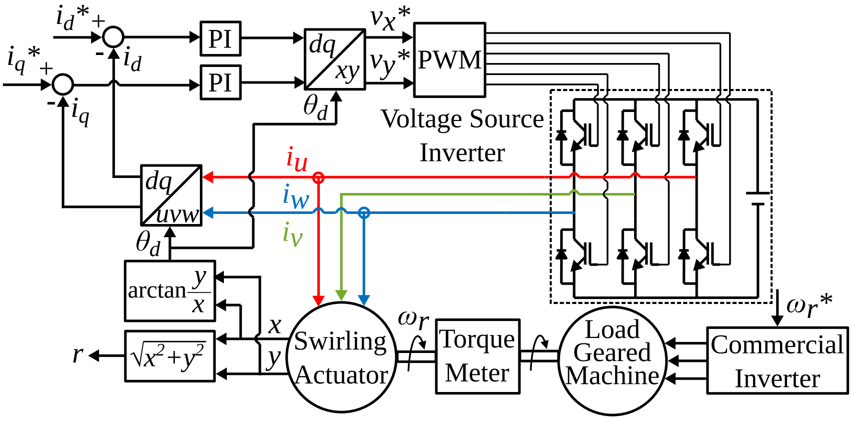

Fig. 3.19: Control block diagram for the torque measurement.

Fig. 3.18 shows the test bench. A torque meter (Onosokki SS100) with a range of 10 Nm is used to measure the torque and the rotation speed. The load machine is a geared AC machine (Fuji Hensokuki VX02-025M) with a transmission ratio of 25. The rated power, speed and torque are 200 W, 60 r/min and 30 Nm respectively. To avoid the wearing and reduce the noise, the gear teeth are lubricated by the grease with NLGI grade 2.

Fig. 3.19 shows the control block diagram for the torque measurement. The i_d^*, i_q^*, and ω_r^* are the references of the d-axis current, q-axis current, and rotor angular speed, respectively. The eccentric direction angle θ_d is calculated by the measured x- and y-axis displacements x and y as

$$\theta_d = \arctan \frac{y}{x}. \tag{3.60}$$

The θ_d is used for the coordinate transformation between the static xy coordinates and rotational dq coordinate systems. The rotor angular speed ω_s is regulated by the load machine.

Fig. 3.20 shows the measured waveforms when $i_d = 1$ A and $i_q = 1$ A as an example. The x- and y-axis displacements x and y are sinusoidal, which indicates a good circular motion of the swirler. The radius r of the circular motion has an average value of 0.37 mm which is slightly shorter than the maximum value $r_0 = 0.4$ mm. The current frequency f_s is 10 Hz and the rotor speed is about 5 r/min The measured torque is 1.0 Nm.

Fig. 3.21 shows the measured torque T in the plane of d- and q-axis currents i_d and i_q. The current frequency f_s is 10 Hz. The current values are limited by the maximum current

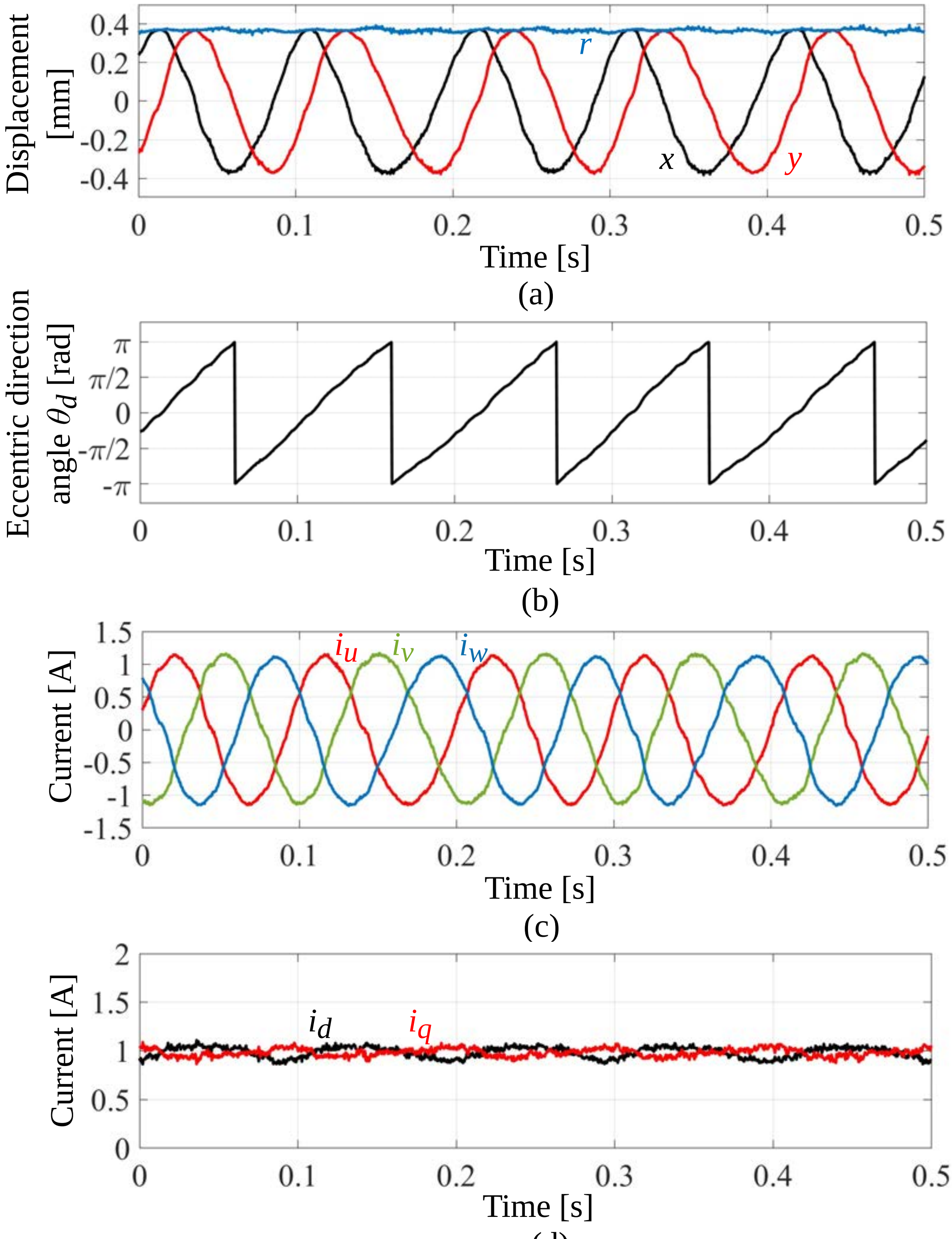

(a)

(b)

(c)

(d)

Fig. 3.20: Measured results of (a) x-axis displacements x, y-axis displacement y and radius r of the circular motion; (b) eccentric direction angle θ_d; (c) phase currents i_u, i_v and i_w; (d) d- and q-axis currents i_d and i_q. The references $i_d^* = 1$ A and $i_q^* = 1$ A.

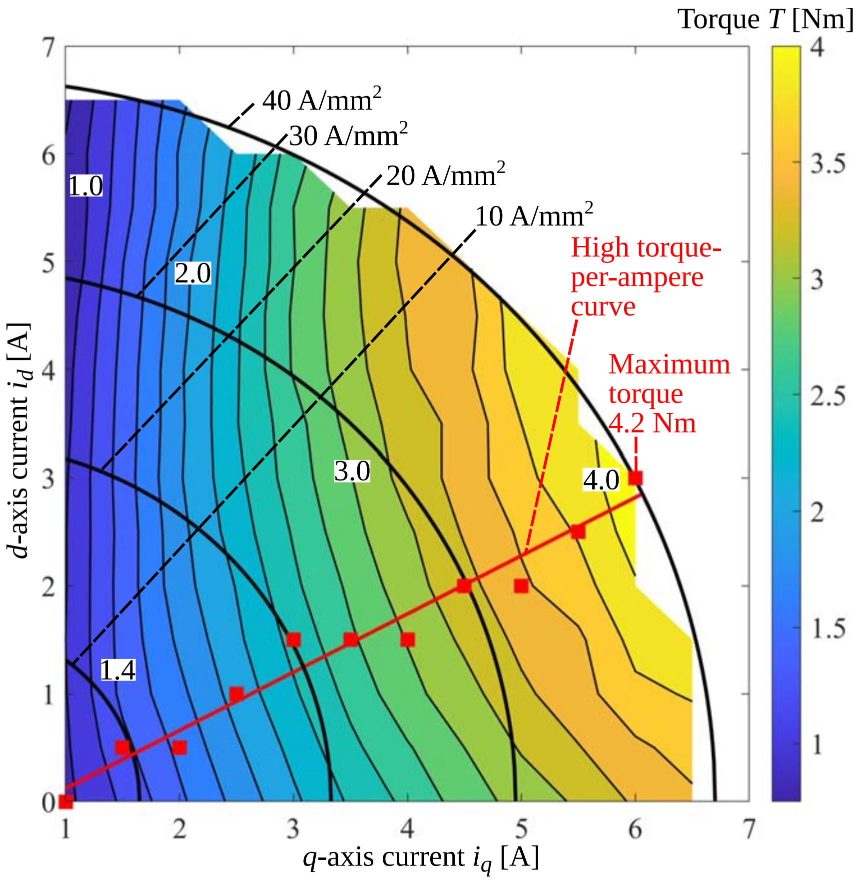

Fig. 3.21: Measured torque in the plane of d- and q-axis currents i_d and i_q.

density of 40 A/mm^2. The torque increases with i_q since the q-axis force F_q increases with i_q. The maximum torque is 1.4 Nm at the current density of 10 A/mm^2, which is available for the continuous operation. The maximum torque for short-time operation is 4.2 Nm with $i_d = 3$ A and $i_q = 6$ A at the current density of 40 A/mm^2. The continuous torque density is 9 Nm/L and the short-time peak torque density is 27 Nm/L. It can be observed that the positive i_d enhances the torque, especially when i_q is high. The red squares in Fig. 3.21 indicate the operation points with the maximum torque-per-ampere (T/I_s). The red line is obtained by the linear fitting of these operation points, which could help determine i_d^* and i_q^* based on the reference torque T^*.

3.5.3 System Efficiency Evaluation

The system efficiency is defined as

$$\eta_s = \frac{P_r}{P_{in}} \tag{3.61}$$

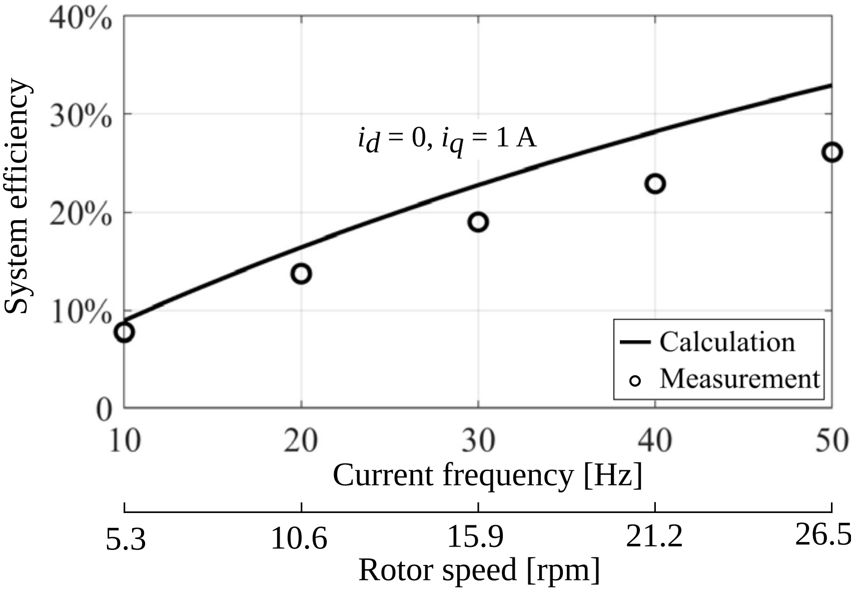

Fig. 3.22: Measured and calculated system efficiency.

Tab. 3.3: System efficiency and power.

	$i_d = 0$; $i_q = 1$ A; $f_s = 50$ Hz
η_s (calculation)	35%
η_s (measurement)	26%
Torque [Nm]	1.0
P_{in} [W]	10.7
P_r [W]	2.8
Copper loss [W]	6.4
Mechanical loss [W]	1.5

where P_{in} is the input electric power. The input electric power P_{in} is measured by a digital power meter (Yokogawa WT1803E). The output power P_r is measured by the product of the measured rotor angular speed ω_r and torque T.

Fig. 3.22 shows the system efficiency η_s from the measurement and calculation. The current operation point is $i_d = 0$ A and $i_q = 1$ A. The current frequency f_s is from 10 Hz to 50 Hz, corresponding to the rotor speed from 5.3 r/min to 26.5 r/min. The η_s increases when f_s increases and reaches 26% at 50 Hz. The measurement is stopped at 50 Hz since the acoustic noise becomes significant. The system efficiency η_s is reasonable since the actuator operates at very low speeds.

The calculated η_s is the ratio between the calculated output power P_r and the calcu-

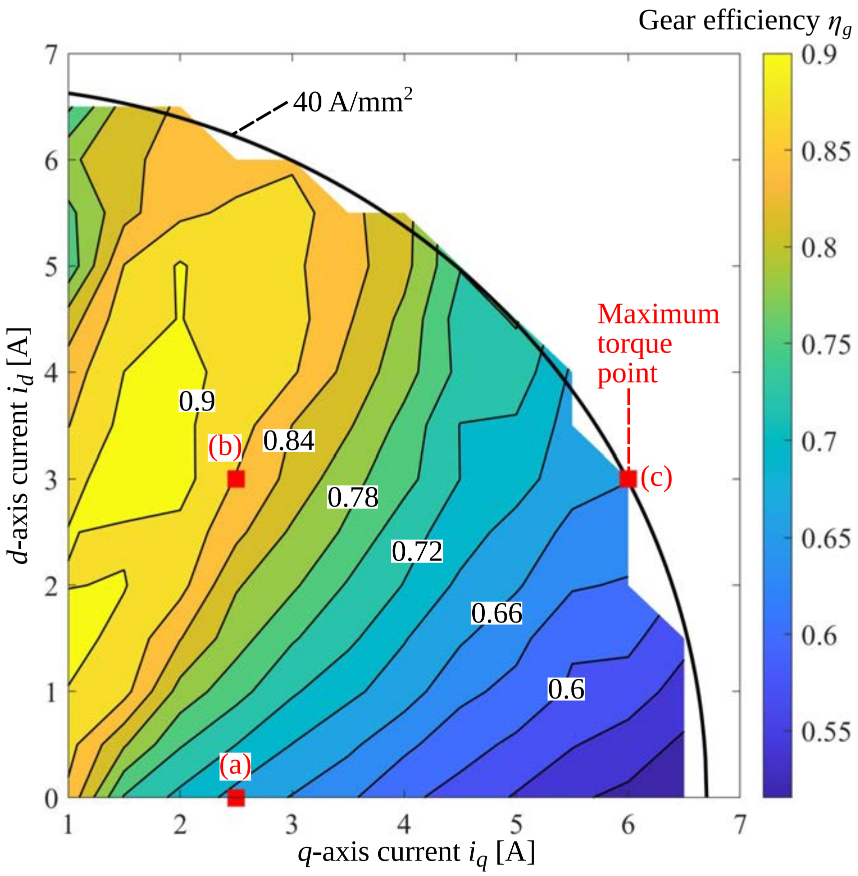

Fig. 3.23: Gear efficiency η_g in the plane of d- and q-axis currents i_d and i_q.

lated input power P_{in}. The calculated P_r is obtained by assuming the ideal gear efficiency, which indicates $P_r = P_{sw}$ and $r = r_0$. The F_q is estimated by the product of i_q and the current force factor k_i. The calculated P_{in} includes the calculated P_r, the copper loss and the eddy current loss. The cooper loss is calculated by the current and the eddy current loss is calculated by 3-D FEA. The FEA results show that the eddy current loss is smaller than 0.01 W at the measured operation point, so the iron loss can be ignored.

Since the mechanical loss is not considered in the calculated η_s, there are discrepancies between the measured η_s and the calculated η_s. The discrepancies become large when f_s increases. This indicates that the mechanical loss increases when f_s increases.

Tab. 3.3 lists the system efficiency and the power at $f_s = 50$ Hz. The copper loss is more predominant than the mechanical loss. A high current force factor k_i will be desirable to reduce the copper loss and improve the system efficiency.

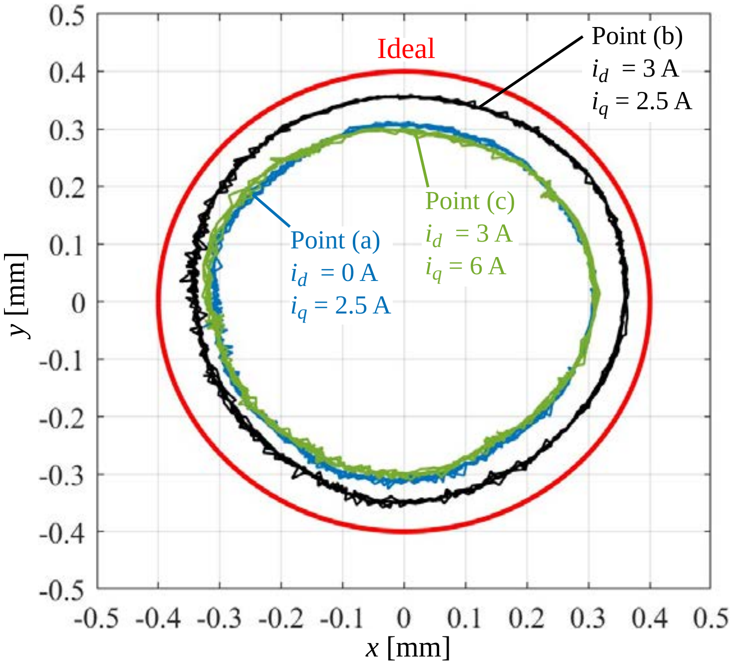

Fig. 3.24: Swirler center loci at points (a), (b) and (c).

3.5.4 Gear Efficiency Evaluation

Fig. 3.23 shows the gear efficiency η_g in the plane of the d- and q-axis currents i_d and i_q. The η_g is given by (3.8) with the measured torque T and the estimated F_q. The current frequency f_s is 10 Hz. Compared with Fig. 3.21, it is found that η_g is relatively high in the low-torque region but decreases in the high-torque region. Providing a positive i_d can improve η_g.

From (3.9), η_g decreases if the radius r of the circular motion is shorter than the maximum value r_0. As a result, the torque also decreases. Fig. 3.24 shows the swirler center loci during the circular motion at operation points (a), (b) and (c), as indicated in Fig. 3.23. The ideal locus with the maximum eccentric radius r_0 of 0.4 mm is also shown. The radii r of the loci at the three operation points are all shorter than r_0. Tab. 3.4 lists the performance data at the three operation points. It is verified that η_g is lower than $\frac{r}{r_0}$ as indicated in (3.9). Among the three points, the locus of point (b) has the large radius r of 0.36 mm. The loci of points (a) and (c) have a short radius r of 0.30 mm. By comparing point (a) and point (b), it is found that a large F_d can enlarge r. By comparing point (b) and point (c), it is found that r is reduced when the torque increases.

Tab. 3.4: Performance of the prototype at typical operation points.

	(a)	(b)	(c)
F_d (FEA) [N]	41	122	111
F_q (FEA) [N]	61	60	140
Torque [Nm]	1.9	2.3	4.2
r [mm]	0.30	0.36	0.30
r/r_0	75%	90%	75%
η_g	69%	86%	66%

3.6 Summary

This chapter presents the principle and analysis of the swirling actuator with SPM-structure swirler. The 12-slot-12pole electromagnetic part is designed based on the principle of radial force generation. The 3-D FEA and experiments show that the radial force is generated as expected. The swirler eccentric radius and gear efficiency are found to be dependent on the radial force. The peak torque density of the prototype reaches 27 Nm/L with a small volume of 0.16 L.

Chapter 4

Torque Density Improvement of Swirling Actuator

4.1 Introduction

The preliminary prototype (Prototype 1) presented in Chapter 3 was built to verify the principle of the proposed swirling actuator. In this chapter, the swirling actuator is improved to raise the torque density. First, the dimensions of the swirler are optimized to enhance the electromagnetic radial force. Second, the mechanical gear design is investigated and a new gear design is presented. Two new prototypes were built and the test results are shown.

4.2 Radial Force Enhancement

4.2.1 Swirler Dimension Optimization

In Chapter 3.4, first, the radial air-gap flux density is calculated by (3.12), (3.32), and (3.33). Fig. 4.1 shows the waveforms for the analytical calculation of the radial air-gap flux density. Then, the radial force components are calculated with Maxwell's stress tensor method.

The air-gap length of the preliminary prototype was relatively large to guarantee a successful operation. According to (3.8), the torque is proportional to the q-axis force F_q.

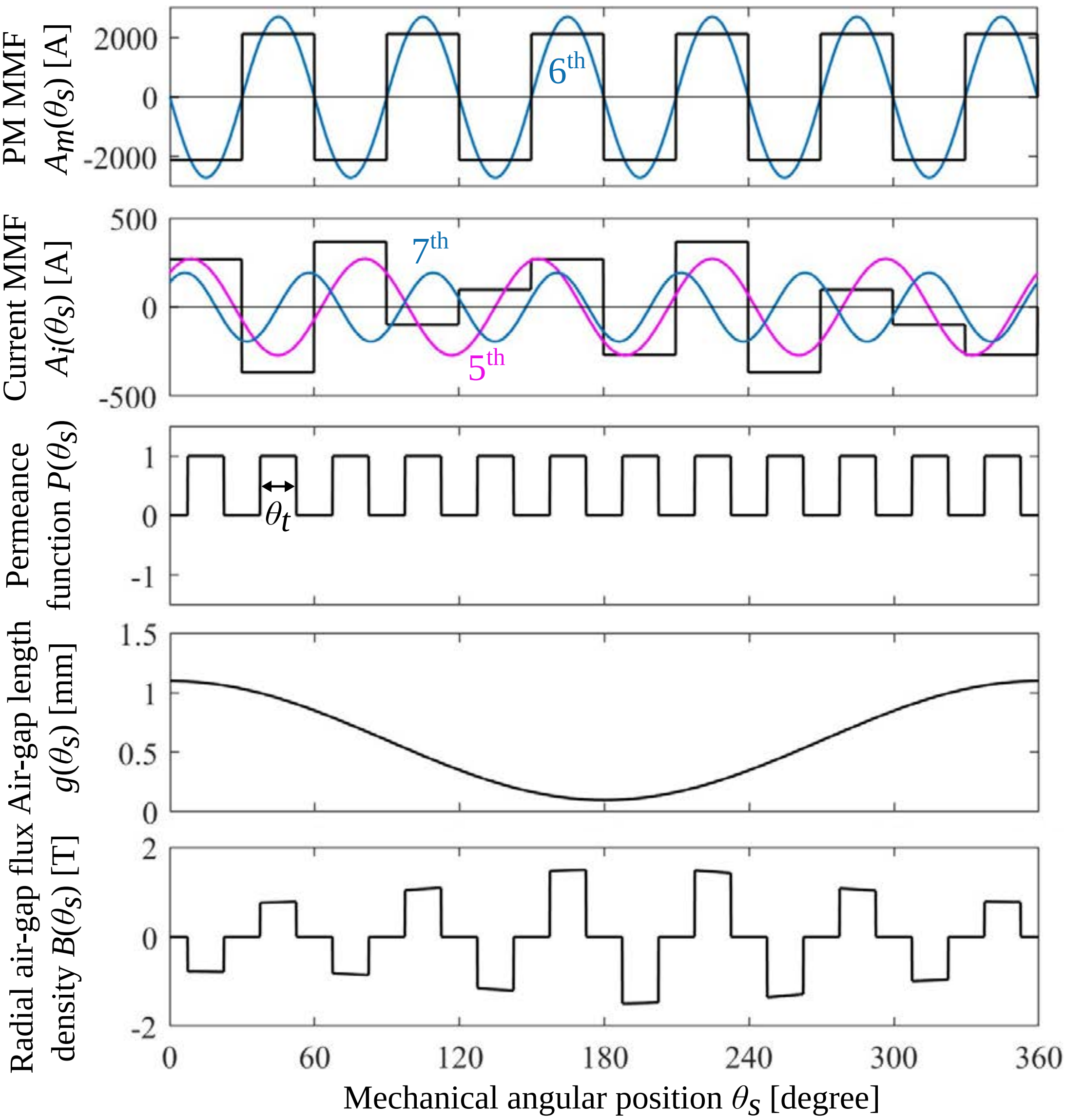

Fig. 4.1: Waveforms for analytical calculation of the radial air-gap flux density.

To enlarge F_q, a short air-gap length is desirable and the dimensions of the SPMs should be optimized.

From (3.44), the partial derivative of the current force factor k_i with respect to the PM thickness t_m is derived as

$$\frac{\partial k_i}{\partial t_m} = (\frac{1}{5}\sin\frac{5\theta_t}{2} + \frac{1}{7}\sin\frac{7\theta_t}{2})\frac{8\sqrt{6}N_s r_{st} l_s B_R \sin 3\theta_t \cos\frac{\pi}{12}}{\pi\mu_r^2} \times \frac{g_0 - t_m/\mu_r}{(g_0 + t_m/\mu_r)^3}. \tag{4.1}$$

For a certain value of the nominal air-gap length g_0, k_i reaches the maximum when (4.1) is zero, i.e., the PM thickness $t_m = \mu_r g_0$.

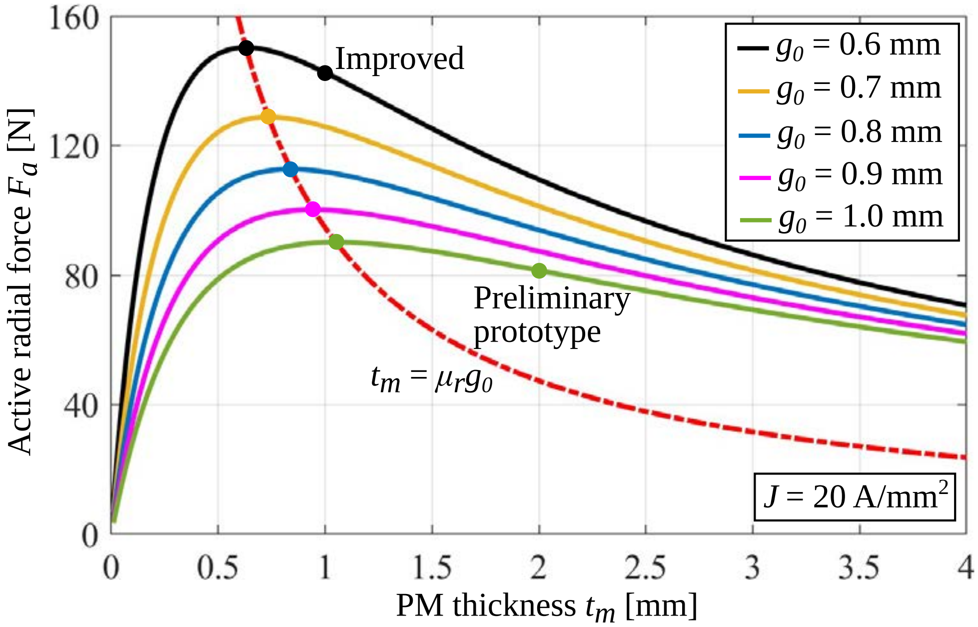

Fig. 4.2: Analytical results of the active radial force F_a with respect to the nominal air-gap length g_0 and PM thickness t_m.

From Fig. 3.11, the active force F_a equals to F_q when θ_i is 90°. Fig. 4.2 shows the analytical results of the active force F_a with respect to the PM thickness t_m. The current density is 20 A/mm^2. There are five solid curves corresponding to different values of g_0 from 0.6 to 1.0 mm with a step of 0.1 mm. Moreover, the red dashed curve satisfying $t_m = \mu_r g_0$ is also shown, which intersects with the other five curves at the peak points. The active force increases as g_0 becomes short. Thus, the design point should be on the curve satisfying $t_m = \mu_r g_0$, and has a g_0 as short as possible. As the relative permeability of PMs μ_r is close to 1, the PMs are expected to be as thin as the air-gap length. However, in the real design, PMs thinner than 1 mm are avoided due to the fabrication difficulty and possible irreversible demagnetization. In the preliminary prototype, the design point is at $t_m = 2$ mm and $g_0 = 1$ mm. In the improved electromagnetic part, $g_0 = 0.6$ mm and $t_m = 1$ mm are selected.

4.2.2 FEA Results

The optimization is verified by 3-D FEA. Fig. 4.3 shows the FEA and calculated results of radial forces F_d and F_q with respect to the q-axis current i_q. Note that the calculated radial forces are obtained by numerical integrations of (3.11) and (3.38) using

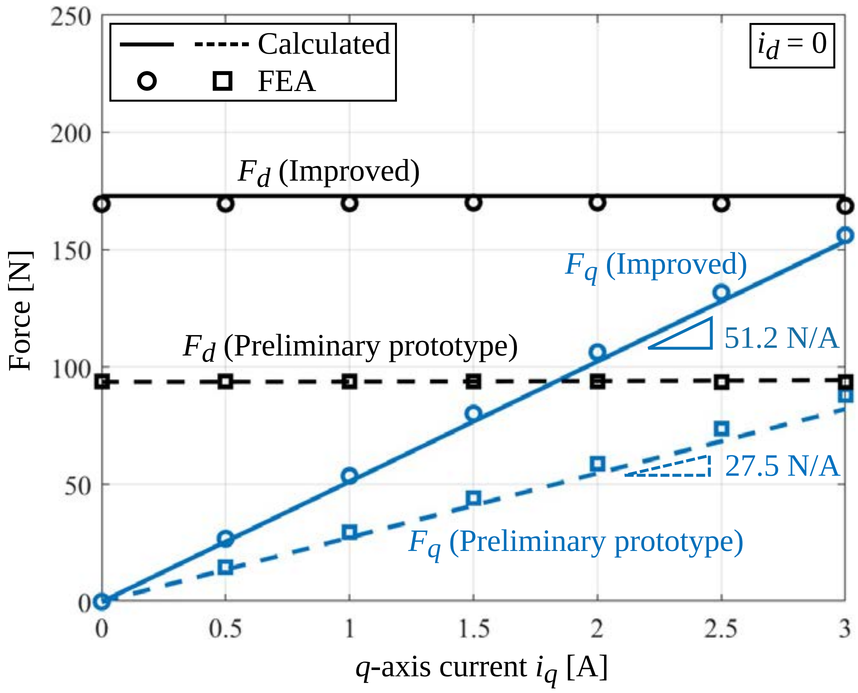

Fig. 4.3: FEA and calculated results of radial force components with respect to the q-axis current i_q.

the original waveforms of $A_m(\theta_s)$, $A_i(\theta_s)$, and $g(\theta_s)$ as shown in Fig. 4.1. There are two reasons for conducting numerical integrations here. First, in Chapter 3.3, only the dominant 6^{th} component of $A_m(\theta_s)$ and 5^{th} and 7^{th} components of $A_i(\theta_s)$ are considered to calculate the radial forces. Besides the dominant components, for $k = 2, 3 \ldots$, the $[(2k-1)6]^{th}$ components in $A_m(\theta_s)$ can also generate the radial forces with the $[(2k-1)6 \pm 1]^{th}$ components in $A_i(\theta_s)$. Second, in the preliminary prototype, the eccentric radius r (< 0.4 mm) is much shorter than the effective air-gap radius g_e (approximately 3 mm). Thus, the approximation (3.34) is relatively accurate. In comparison, the improved electromagnetic part has a shorter effective air-gap radius g_e (approximately 1.6 mm). As a result, the approximation (3.34) will lead to a discrepancy. Conducting numerical integrations can eliminate the discrepancy caused by the approximation (3.34). The d-axis current i_d is zero, indicating that F_d only contains the PM attractive force F_{dm} and F_q equals to the active force F_a. The F_d does not change with i_q, whereas F_q is proportional to i_q. The calculated results agree well with the FEA results. The current force factor k_i is enhanced from 27.5 N/A to 51.2 N/A in the improved electromagnetic part. The F_{dm} is also enhanced from 94 to 173 N.

4.3 Investigation of Gear Design

In Chapter 3, the experimental results indicate that the gear efficiency and actual eccentric radius of the swirler change with the operation points. The reasons are explained in this section by investigating the gear design parameters. A new gear set with identical dimensions and a higher transmission ratio is designed. The effects of gear design parameters on the output torque and mechanical design are illustrated.

4.3.1 Effect of Pressure Angle

Fig. 4.4 shows two gear sets to explain the effect of the pressure angle. The swirler gear is eccentric and meshes with the rotor gear in the x-direction. At the meshing point, there is a pressure force F_{sw} on the swirler perpendicular to the tooth surface. The F_{sw} can be decomposed into the radial component F_r and tangential component F_t. The angle between F_t and F_{sw} is the pressure angle α. The F_{sw} and F_t can be written as the functions of F_r:

$$F_{sw} = \frac{F_r}{\sin\alpha}, \tag{4.2}$$

$$F_t = \frac{F_r}{\tan\alpha}. \tag{4.3}$$

The tangential force F_t generates the rotor output torque. If the friction is ignored, the rotor output torque is given by

$$T = F_t r_r \tag{4.4}$$

where r_r is the rotor pitch circle radius. By substituting (4.3) into (4.4), the rotor output torque is given by

$$T = \frac{F_r r_r}{\tan\alpha}. \tag{4.5}$$

The gear set in Fig. 4.4(a) has a large pressure angle of $\alpha = 42°$, which is identical to the preliminary prototype. In contrast, the gear set in Fig. 4.4(b) has a smaller $\alpha =$ of 20°. From (4.5), with the identical F_r, the gear set in Fig. 4.4(b) can generate a higher torque because of the smaller α.

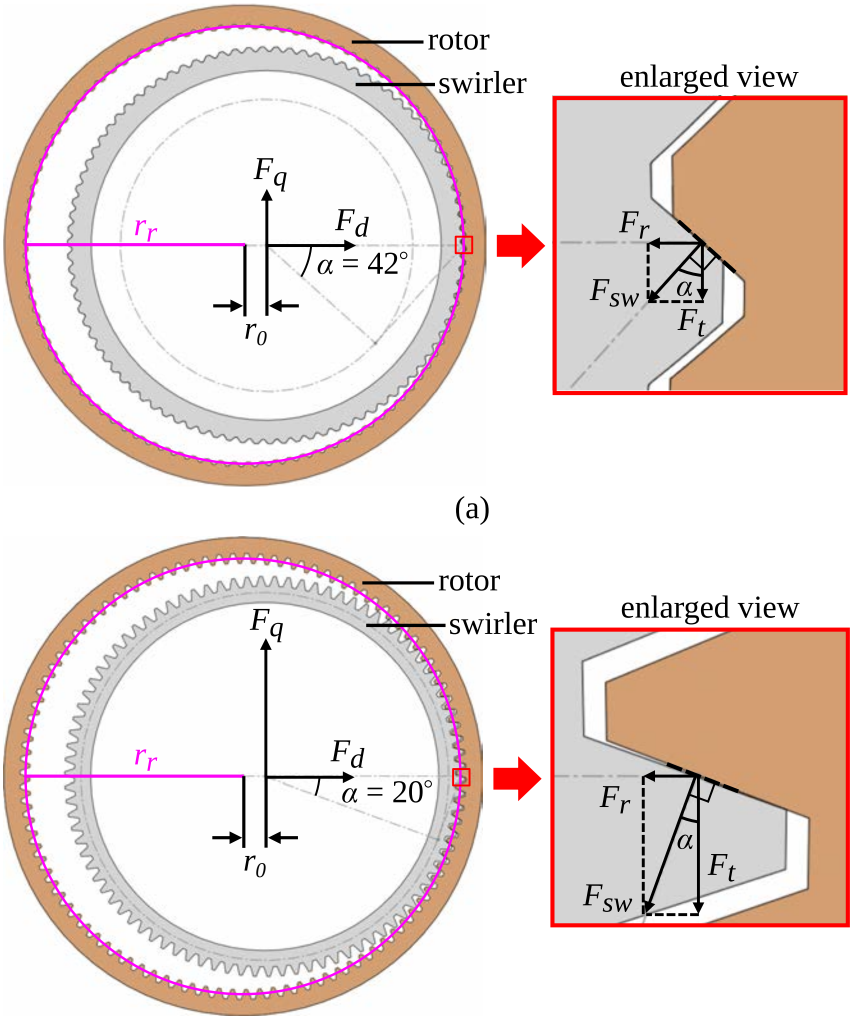

(a)

(b)

Fig. 4.4: Gear sets with different pressure angles α. (a) $\alpha = 42°$, (b) $\alpha = 20°$.

4.3.2 Gear Center Distance

Fig. 4.5 shows the schematic for calculating the gear center distance. Note that the gear center distance is equal to the eccentric radius r of the swirler. Point O_1 and O_2 are the centers of the rotor gear and swirler gear, respectively. The red and blue solid circles are the base circles of the rotor gear and swirler gear with the radii of r_r and r_{sw}, respectively. The red and blue dashed circles are the base circles of the rotor gear and swirler gear with the radii of r_{b1} and r_{b2}, respectively. The radii of the base circles r_{b1} and r_{b2} satisfy the following equations:

$$r_{b1} = r_r \cos\alpha, r_{b2} = r_{sw} \cos\alpha. \tag{4.6}$$

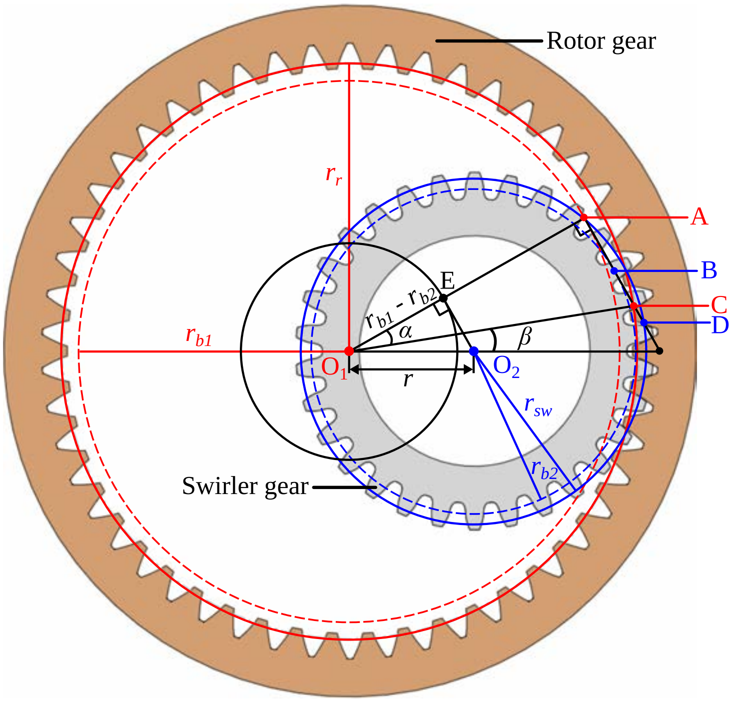

Fig. 4.5: Schematic for calculating the gear center distance.

The module m_g is the parameter describing the size of gear teeth. The definition of m_g is

$$m_g = \frac{2r_r}{Z_r} = \frac{2r_{sw}}{Z_{sw}}. \tag{4.7}$$

The segment AD is the common tangent of the two base circles. Point C is the intersection point between the segment AD and the rotor pitch circle. The angle $\angle \mathrm{CO_1E}$, which is the angle between the eccentric direction and meshing angular position, is defined as β. Let us draw an auxiliary circle that is concentric with the rotor gear and has a radius of $(r_{b1} - r_{b2})$. The segment O$_2$E is the tangent of the auxiliary circle and is parallel with the segment AD. Thus,

$$r = \frac{r_{b1} - r_{b2}}{\cos{(\alpha + \beta)}}. \tag{4.8}$$

By substituting (4.7) and (4.6) into (4.8), r is derived as

$$r = (\frac{Z_r - Z_{sw}}{2})\frac{\cos\alpha}{\cos{(\alpha + \beta)}}m_g. \tag{4.9}$$

The β is derived by (4.9) as

$$\beta = \arccos[\frac{(Z_r - Z_{sw})m_g}{2r} \cos\alpha] - \alpha. \tag{4.10}$$

There are two conditions that may lead to non-zero β. First, the gear set adopts profile shifts in the design process. Second, the actual gear center distance is different from the nominal gear center distance due to fabrication accuracy or different operation points.

When β is zero, (4.9) is simplified into

$$r = \frac{m_g}{2}(Z_r - Z_{sw}). \tag{4.11}$$

Gear 1 in the preliminary prototype has a module m_g of 0.8 mm, a tooth number difference $(Z_r - Z_{sw})$ of 1, and a pressure angle α of 42°. In Chapter 3, the maximum eccentric radius of the swirler r_0 is set as 0.4 mm, which would be equal to the nominal center distance of Gear 1 if Gear 1 did not have profile shifts. However, after the experiments of Chapter 3, it was found that the swirler gear has a profile shift coefficient of -0.125. As a result, the nominal center distance of Gear 1 becomes 0.5 mm. In the new gear design, both the nominal gear center distance and maximum eccentric radius r_0 of the swirler are set as 0.5 mm.

4.3.3 New Gear Design

Fig. 4.6 shows the gear design candidates. The rotor pitch circle radius r_r is about 45 mm and should lead to integer tooth numbers. The values of m_g in Fig. 4.6 are 0.4, 0.5, 0.6, 0.8 and 1 mm which are standard values listed in JISB1702-1. As m_g decreases, the gear tooth becomes smaller, and the tooth numbers increase. The tooth number difference $(Z_r - Z_{sw})$ is set as 1 to maximize the the transmission ratio G according to (3.10). For involute-type gears, such a small tooth number difference may cause undesirable tooth interference. For each combination of α and m_g, the corresponding β is calculated by (4.10) and the interference condition is checked according to Chapter 2.9 of [93]. The selected gears should have no interference. The objectives of the new Gear 2 are reducing the pressure angle α and increasing the transmission ratio G to enhance the torque. Thus,

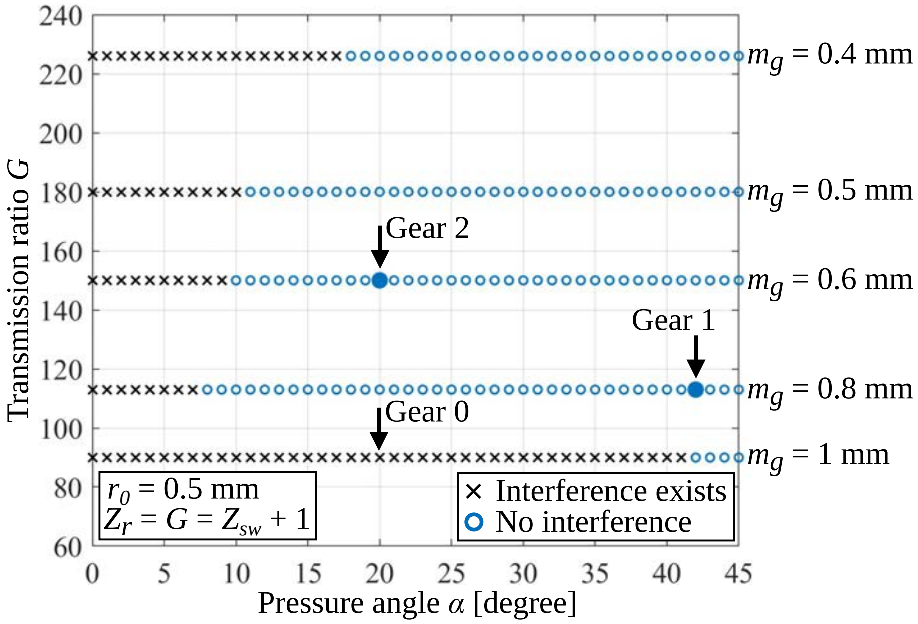

Fig. 4.6: Gear design candidates.

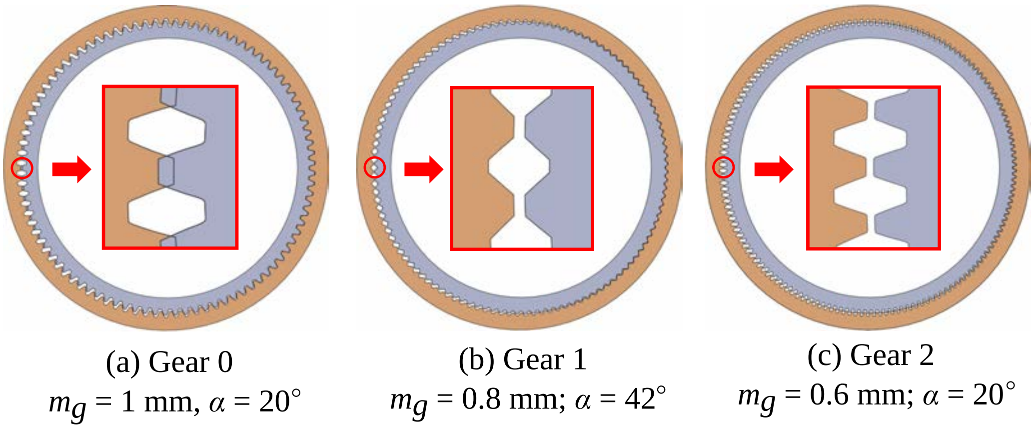
(a) Gear 0
m_g = 1 mm, α = 20°

(b) Gear 1
m_g = 0.8 mm; α = 42°

(c) Gear 2
m_g = 0.6 mm; α = 20°

Fig. 4.7: Tooth interference conditions of Gear 0, Gear 1 and Gear 2.

Gear 2 with $\alpha = 20°$ and $m_g = 0.6$ mm is adopted for the new prototypes. The resultant transmission ratio is 150 which is higher than that of Gear 1. Note that most general involute-type gears adopt the pressure angle $\alpha = 20°$. Thus, Gear 2 may also improve the manufacturability compared with Gear 1.

Fig. 4.7 shows the interference conditions of Gear 0, Gear 1 and Gear 2 as indicated in Fig. 4.6. Gear 0 has a module m_g of 1 mm and a pressure angle α of 20°. According to (4.10), when $r_0 = 0.5$ mm, $m_g = 1$ mm and $(Z_r - Z_{sw}) = 1$, β is always zero regardless of the value of α. Thus, there is no profile shift in Gear 0 and tooth interference exists. In contrast, Gear 1 and Gear 2 have profile shifts and do not have any tooth interference.

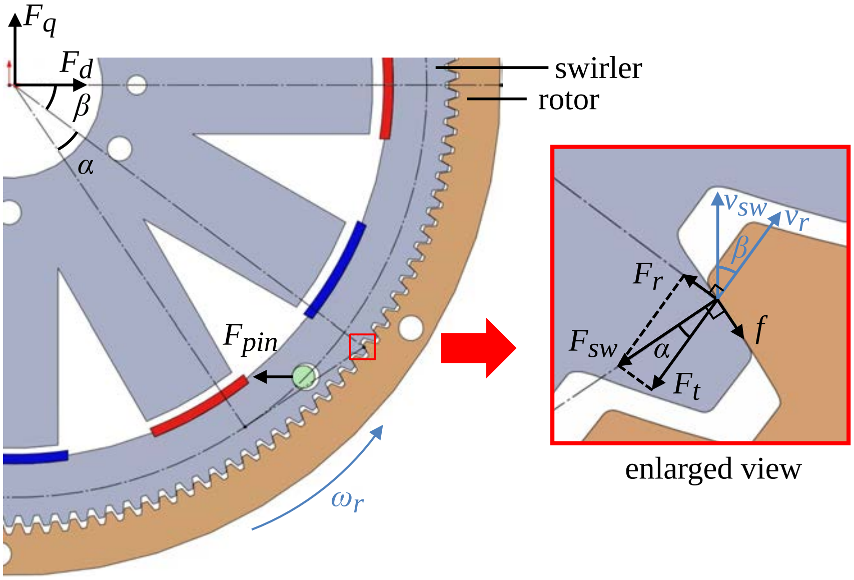

Fig. 4.8: Forces on the swirler and velocities of the swirler and rotor.

4.3.4 Analysis of Gear Efficiency

Fig. 4.8 shows the forces on the swirler and velocities of the swirler and rotor. The F_{pin} is the pressure force from the pins. The friction f on the tooth surface is perpendicular to the pressure force F_{sw}. The swirler is eccentric in the x-direction. When the actuator is in the steady state, the resultant force of the swirler is the centripetal force towards the stator center. The forces on the swirler in the radial and tangential directions satisfy the following equations:

$$\begin{aligned} F_r + (F_{pin} - F_d)\cos\beta + F_q \sin\beta - f\cos\alpha &= m\omega_s^2 r\cos\beta, \\ F_t + (F_{pin} - F_d)\sin\beta - F_q\cos\beta + f\sin\alpha &= m\omega_s^2 r\sin\beta. \end{aligned} \tag{4.12}$$

The friction f is given by

$$f = \mu F_{sw}, \tag{4.13}$$

where μ is the coefficient of friction. The swirler velocity $\boldsymbol{v_{sw}}$ is in the q-axis, whereas the rotor velocity $\boldsymbol{v_r}$ at the meshing point is in the tangential direction. The angle between $\boldsymbol{v_{sw}}$ and $\boldsymbol{v_r}$ is β. When β is not zero, there is a relative motion between the swirler and rotor at the meshing point. The friction loss P_f is calculated as

$$P_f = (f\cos\alpha)(v_{sw}\sin\beta) + (f\sin\alpha)(v_{sw}\cos\alpha - v_r). \tag{4.14}$$

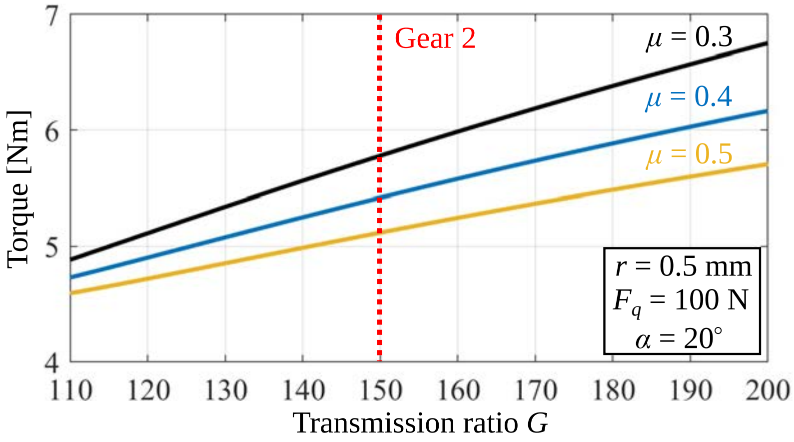

Fig. 4.9: Calculated torque with respect to the transmission ratio G.

The magnitudes of the velocities are

$$v_{sw} = \omega_s r, v_r = \omega_r r_r \tag{4.15}$$

Then, the mechanical power of the rotor considering the friction loss is given by

$$P_r = F_q v_{sw} - P_f = F_q \omega_s r - P_f. \tag{4.16}$$

By substituting (3.4) and (4.16) into (3.7), the gear efficiency η_g is given by

$$\eta_g = \frac{F_q \omega_s r - P_f}{F_q \omega_s r_0}. \tag{4.17}$$

Finally, by (3.8), (3.10), (4.2), (4.3) and (4.12)-(4.17), the rotor output torque is derived as

$$T = F_q G[r\cos(\alpha+\beta) + \frac{\mu r_r \sin\alpha}{G}][\frac{1}{\mu\sin(\alpha+\beta)+\cos(\alpha+\beta)}]. \tag{4.18}$$

Fig. 4.9 shows the calculated torque with respect to G. The eccentric radius r, q-axis force F_q, and pressure angle α are set as 0.5 mm, 100 N and 20°, respectively. The coefficient of friction μ depends on the gear materials, lubrication, fabrication accuracy and surface roughness. It is difficult to calculate or measure μ at this stage. Here μ is assumed to be 0.3, 0.4 and 0.5. Fig. 4.9 indicates that the torque increases as G increases, but on the other hand, it decreases when μ increases. Gear 2 increases the transmission ratio from 113 to 150 compared with Gear 1. This time, even higher transmission ratios are

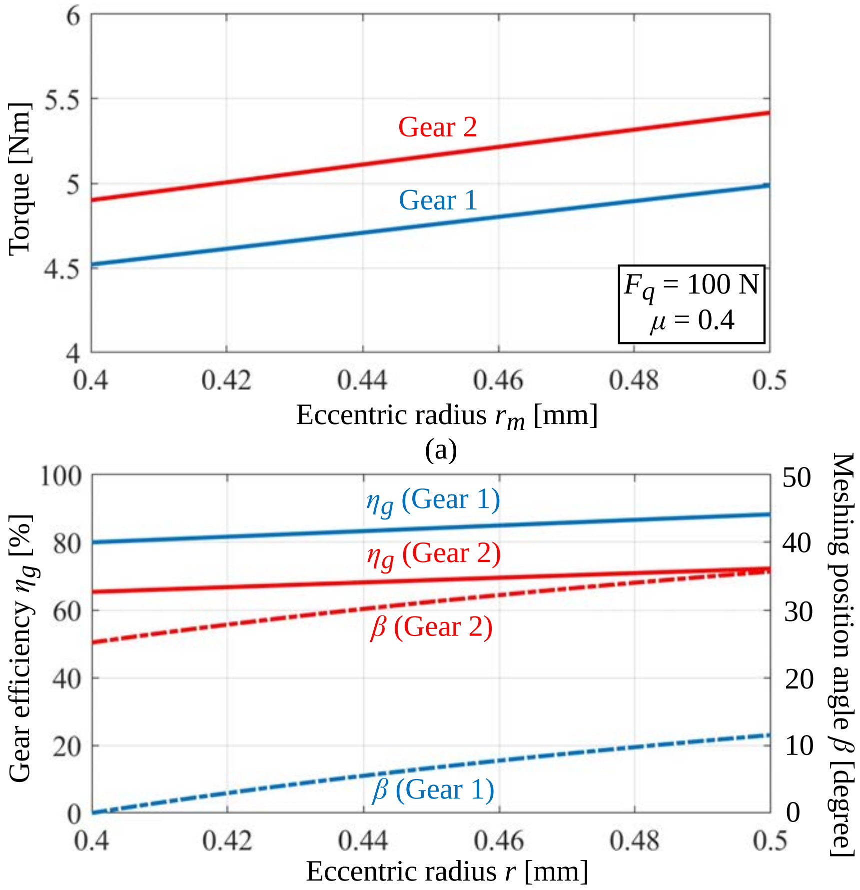

(a)

(b)

Fig. 4.10: Calculated torques with respect to r; (b) calculated gear efficiencies η_g and meshing position angle β with respect to r.

not attempted because the small gear teeth may have a problem in mechanical fabrication precision.

Fig. 4.10(a) shows the calculated torques of Gear 1 and Gear 2 with respect to r when $F_q = 100$ N and $\mu = 0.4$. Fig. 4.10(b) shows the calculated η_g and β with respect to r of Gear 1 and Gear 2. It is observed that the gear efficiency η_g increases as the eccentric radius r increases. The reason is that the rotor mechanical power P_r increases as r increases as shown in (34). Moreover, the maximum efficiency of Gear 2 is 72%, whereas the maximum efficiency of Gear 1 is 88%. As shown in Fig. 7, a large β indicates that the relative velocity between the swirler and rotor is high. As a result, the friction loss P_f is high. The gear efficiency of Gear 2 is lower than that of Gear 1 due to the larger β of Gear 2. However, Gear 2 has a higher torque than Gear 1 owing to the high transmission ratio.

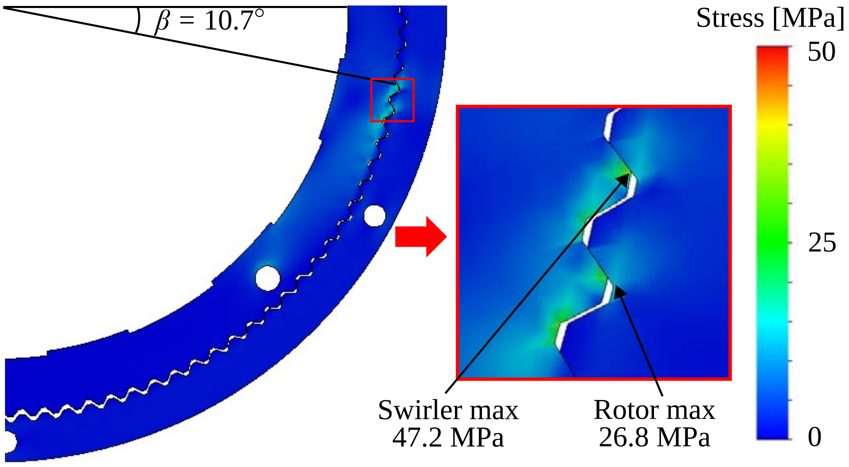

(a) Gear 1

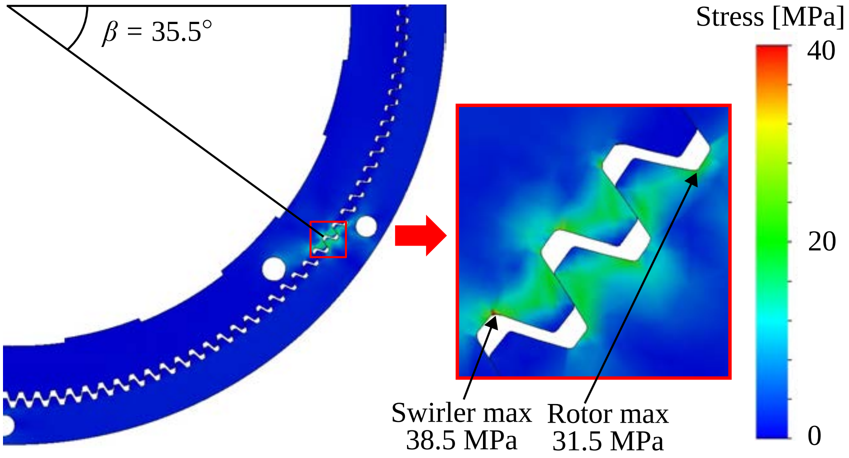

(b) Gear 2

Fig. 4.11: Contour plots of the von Mises stresses on (a) Gear 1 and (b) Gear 2.

4.3.5 Mechanical Stress Analysis of Gears

To validate that the gears have enough strength, the mechanical stresses on the gears are analyzed with 3-D FEA. Fig. 4.11 shows the contour plots of the von Mises stresses on Gear 1 and Gear 2. The swirler is eccentric in the x-direction with the radius of 0.5 mm. A torque of 10 Nm is set on the rotor. The swirler material is the carbon steel S45C (ANSI 1045), whereas the rotor material is the stainless steel SUS304 (ANSI 304). The yield strengths of S45C and SUS304 are 530 MPa and 207 MPa respectively. It can be observed that the stresses are high around the meshing teeth. On the swirler of Gear 1, the maximum stress is 47.2 MPa that is 9% of the yield strength of S45C. On the rotor of Gear 1, the maximum stress is 26.8 MPa that is 13% of the yield strength of SUS304. On

Tab. 4.1: Specifications of prototypes.

	Prototype 1	Prototype 2	Prototype 3
Outer diameter D [mm]	100	100	100
Axial length with end-windings L [mm]	20	20	20
Gear nominal center distance [mm]	0.5	0.5	0.5
Nominal air-gap length g_0 [mm]	1	0.6	0.6
PM thickness t_m [mm]	2	1	1
Rotor pitch radius r_r [mm]	45.2	45.2	45
Gear module m_g [mm]	0.8	0.8	0.6
Pressure angle α [degree]	42	42	20
Transmission ratio G	113	113	150
Swirler gear material	SUS440C	S45C	S45C
Rotor gear material	SUS304	SUS304	SUS304
Rated/Maximum speed [r/min]	5/30	5/30	5/30
Rated/Peak torque [Nm]	1.3/4.2	3.6/7.4	4.1/10.0
Peak torque density [Nm/L]	27	47	64

the swirler of Gear 2, the maximum stress is 38.5 MPa that is 7% of the yield strength of S45C. On the rotor of Gear 2, the maximum stress is 31.5 MPa that is 15% of the yield strength of SUS304. Both Gear 1 and Gear 2 have sufficient margins of stiffness.

4.4 Experiments of Improved Prototypes

Two new prototypes were built to verify the torque density improvement by (i) the electromagnetic optimization and (ii) the improved gear design. Tab. 4.1 lists the specifications of Prototype 1, Prototype 2 and Prototype 3. Compared with Prototype 1, Prototype 2 reduces the nominal air-gap length and PM thickness to enhance the electromagnetic radial force. Prototype 2 further adopts the new Gear 2 with a reduced pressure angle and an enlarged transmission ratio. Fig. 4.12 shows the fabricated gears of the three prototypes.

4.4.1 Considerations of Mechanical Design

Fig. 4.13 shows the front sectional view of the 3-D model of the prototypes. The shaft is fixed with the rotor gear and supported by two mechanical bearings. As shown in Fig.

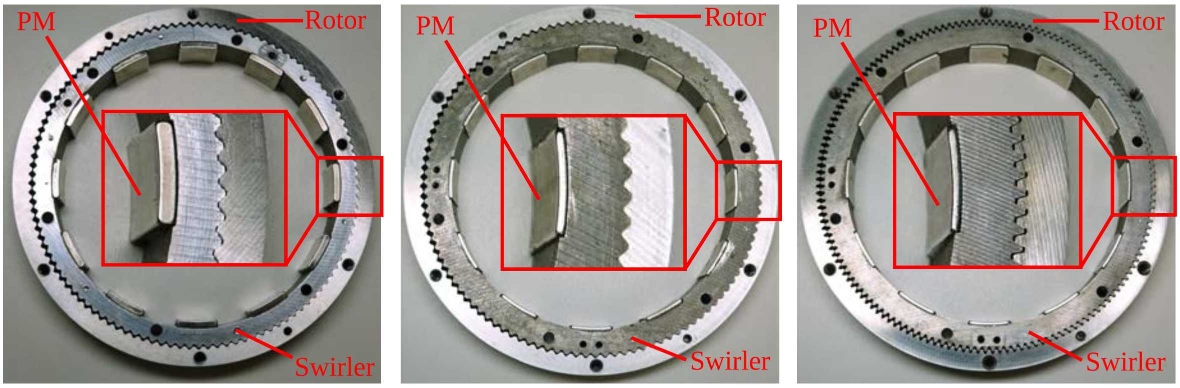

(a) (b) (c)

Fig. 4.12: Pictures of fabricated gears of (a) Prototype 1; (b) Prototype 2; (c) Prototype 3.

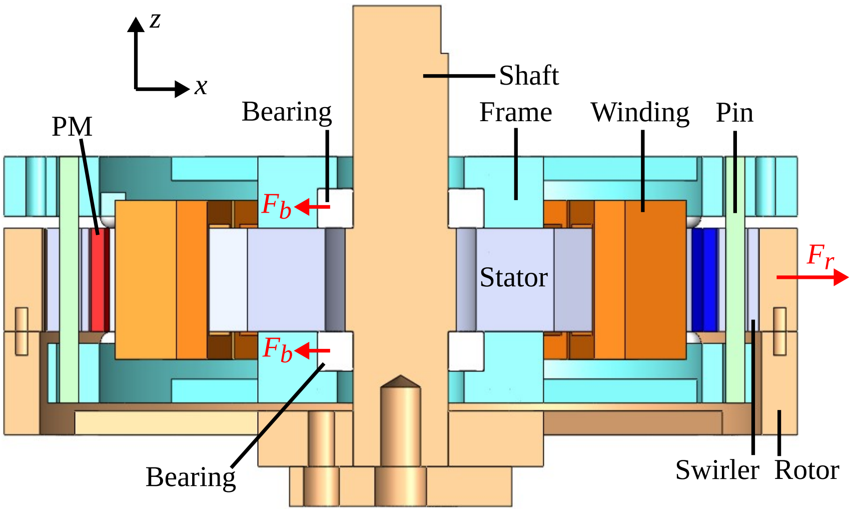

Fig. 4.13: Front sectional view of the prototypes.

4.8, the unbalanced radial force on the rotor is

$$F_{ur} = F_r - f \cos \alpha. \tag{4.19}$$

If the friction f is ignored, based on (4.5), F_{ur} is given by

$$F_{ur} = F_r = \frac{T \tan \alpha}{r_r}. \tag{4.20}$$

Equation (4.20) indicates that reducing the pressure angle α can reduce the unbalanced radial force F_{ur}. By changing α from 42° to 20°, F_{ur} is reduced by 60%. Moreover, the load force on a single bearing is given by

$$F_b = \frac{F_r}{2}. \tag{4.21}$$

The peak torque of the Prototype 3 is 10 Nm. From (4.20) and (4.21), the peak value of F_b is calculated to be 40 N, which is only 2% of the radial load capacity of 1920 N of the bearings (B6801ZZ). Thus, the unbalanced radial force has little effect on the lifetime of the bearings.

Fig. 4.14(a) shows the top view of the 3-D model of the prototypes including the six pins. Fig. 4.14(b) shows the ideal pin configuration when $r = r_0$. The pins are tangential with the frame holes and swirler holes. The diameters of the frame holes and swirler holes are $D_h = 2.8$ mm, and r_0 is 0.5 mm. According to (3.59), the diameter of the pins D_p should be 2.3 mm. To prevent the rotation of the swirler, at least three pins are necessary. By increasing the number of pins to six, the load force on a single pin is reduced and thin pins can be used. The peak torque of Prototype 3 is 10 Nm and the equivalent force that the pins need to overcome is 238 N. Considering the worst condition in which the force is applied on a single pin, the FEA result of the maximum von Mises stress on the pin is 185 MPa. In contrast, the yield strength of the pin material (SUS440C) is 450 MPa. Thus, the pins have adequate stiffness.

It is shown in Chapter 3 that in the actual operation, the eccentric radius r is shorter than the maximum value r_0. Fig. 4.14(c) shows the actual pin configuration when $r < r_0$. The pins are still tangential with the frame holes and swirler holes, but the centers of the frame holes, swirler holes, and pins are no longer collinear. From Fig. 4.8, the force component imposed on the swirler tooth and opposite to F_d is given by

$$F_{dn} = F_r \cos\beta + F_t \sin\beta. \tag{4.22}$$

The swirler is pushed back towards the concentric position by F_{dn}. As a result, the eccentric radius r is reduced. By substituting (4.4) and (4.20) into (4.22), F_{dn} is derived as

$$F_{dn} = \frac{T}{r_r}(\tan\alpha\cos\beta + \sin\beta). \tag{4.23}$$

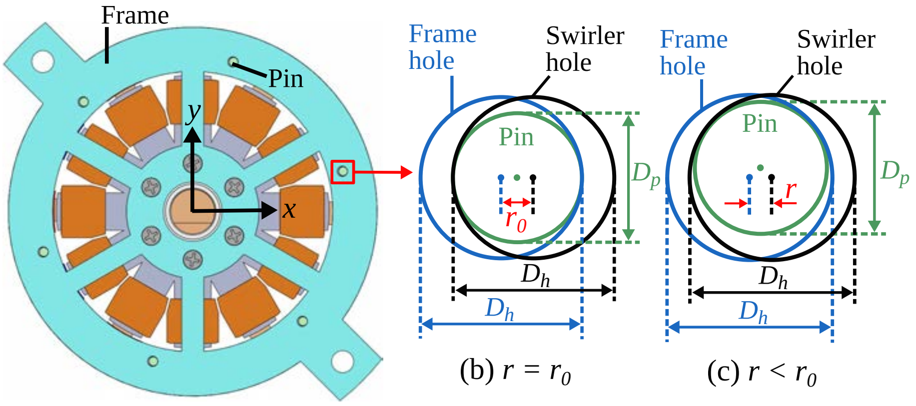

(b) $r = r_0$ (c) $r < r_0$

(a)

Fig. 4.14: (a) Top view of the prototypes; (b) the ideal pin configuration ($r = r_0$); (c) the actual pin configuration ($r < r_0$).

The F_{dn} increases as the torque increases. Consequently, the required F_d to overcome F_{dn} and keep r close to r_0 also increases.

4.4.2 Torque Evaluation

Fig. 4.15 shows the calculated torque, measured torque and measured eccentric radius r, with respect to the d-axis current i_d. The q-axis current is 1.5 A and the rotor speed is 5 r/min. The calculated torque is obtained by (3.8), (3.10) and (4.18). The coefficient of friction μ is assumed to be 0.4 and the FEA results of F_q are used for the calculation. It is noted that r is shorter than r_0 and increases as i_d increases, indicating that increasing the d-axis force F_d can enlarge r. The torque calculated by assuming $r = r_0$ has a large discrepancy compared with the measured torque due to the discrepancy between r and r_0. If the measured value of r is used for the calculation, the discrepancy becomes small. Prototype 3 has a higher torque than that of Prototype 2.

Fig. 4.16 shows the current operation points of Prototype 2 and Prototype 3 at the rotor speed of 5 r/min. For each value of i_q, the i_d that generates the maximum torque is selected, such as the circled points in Fig. 4.15. The current amplitude is limited by the peak current density of 40 A/mm^2. The peak current density is for a short period of about 5–10 seconds. It is shown that the required i_d increases as i_q increases for both prototypes. Prototype 2 suffers from the insufficient i_d when i_q exceeds 3.5 A. In contrast, Prototype 3 needs less i_d to generate the maximum torque. This indicates that the small

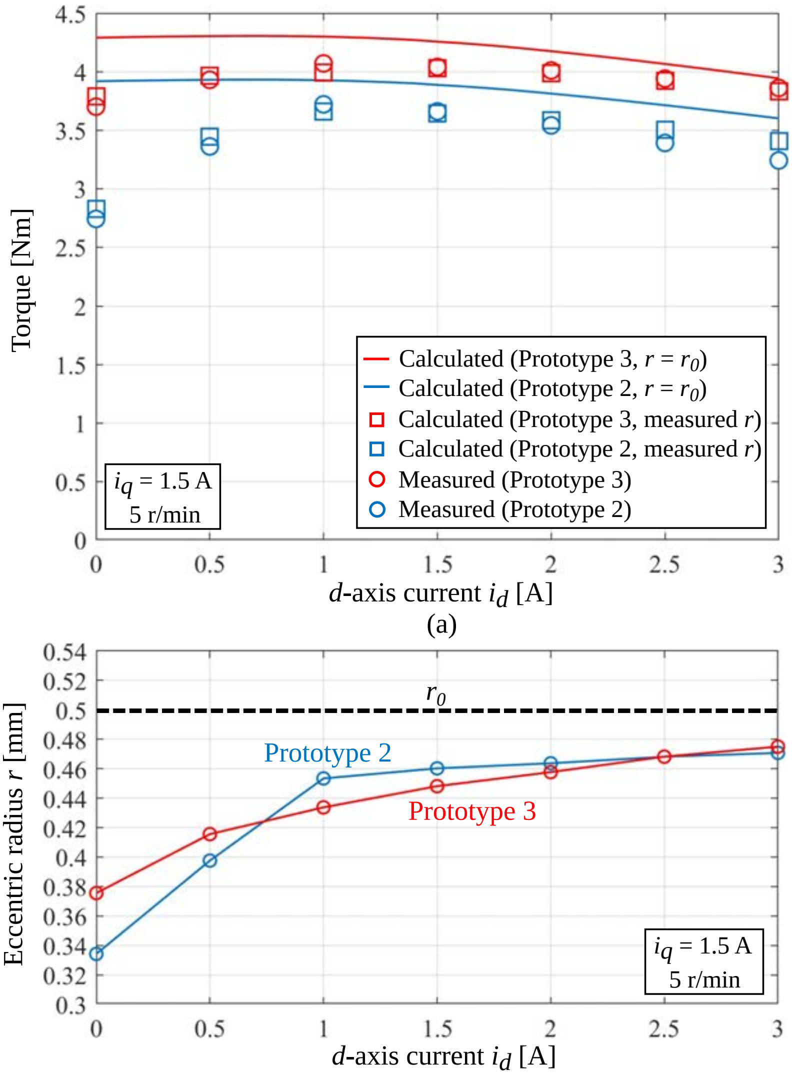

(a)

(b)

Fig. 4.15: (a) Calculated and measured torques and (b) eccentric radius r with respect to the d-axis current i_d. The q-axis current i_q is 1.5 A and the rotor speed is 5 r/min.

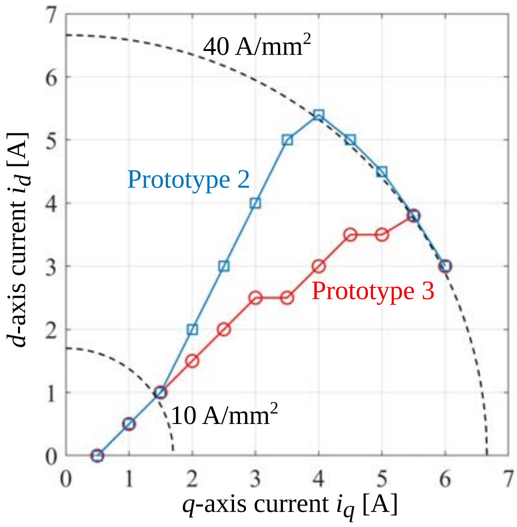

Fig. 4.16: Current operation points at the rotor speed of 5 r/min.

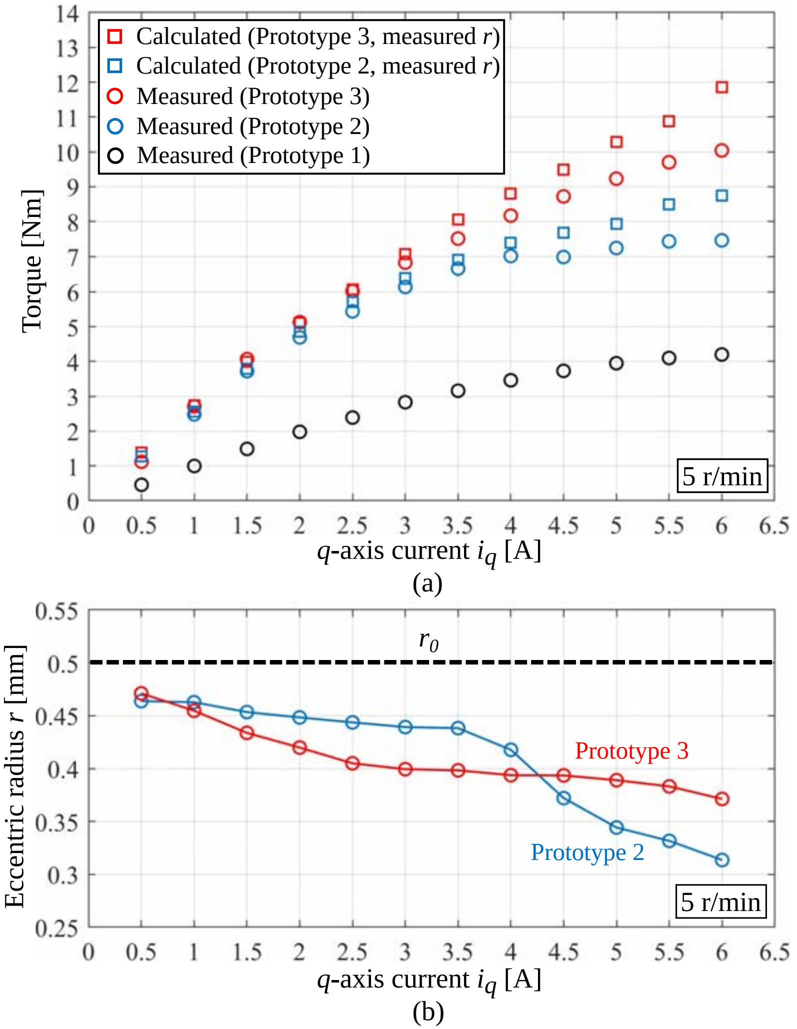

Fig. 4.17: (a) Calculated and measured torques and (b) measured eccentric radius r with respect to the q-axis current i_q. The rotor speed is 5 r/min.

pressure angle in Prototype 3 effectively reduces the radial force F_r on the meshing teeth that needs to be overcome by F_d. As a result, the required i_d is reduced.

Fig. 4.17 shows the calculated torque, measured torque and measured eccentric radius r with respect to the q-axis current i_q. The measured torque of Prototype 1 is also shown for comparison. It is noted that r decreases as i_q increases. There is an obvious decrease of r in Prototype 2 when i_q exceeds 3.5 A due to the limited i_d as shown in Fig. 4.16. The coefficient of friction μ is assumed to be 0.4. For both Prototype 2 and Prototype 3, the calculated torques with the measured r agree with the measured torques when i_q is small. When i_q is large, there are discrepancies between the calculated and measured torques. The possible reason is that μ is not constant and increases with the torque. The peak measured torques of Prototype 2 and Prototype 3 are 7.4 Nm and 10.0 Nm, respectively.

Tab. 4.2: Powers and Losses at Rated Current Density (i_d = 1 A, i_q = 1.5 A).

	Prototype 2		Prototype 3	
Rotor speed [r/min]	5	30	5	30
Current frequency [Hz]	9.4	56.5	12.5	75
Torque [Nm]	3.6	3.0	4.1	3.5
Input power [W]	24.3	35.1	24.7	39.0
Output power [W]	1.9	9.4	2.2	11.0
Copper loss [W]	20.8	20.8	20.8	20.8
Iron loss [W]	0.1	1.6	0.1	2.6
Mechanical loss [W]	1.4	3.3	1.6	4.6
Actuator efficiency	7.8%	26.8%	8.9%	28.2%

The corresponding peak torque densities are 47 and 64 Nm/L, respectively, which are significantly improved compared with the peak torque density of 27 Nm/L of Prototype 1.

4.4.3 Loss and Thermal Evaluations

Tab. 4.2 lists the powers and losses of the two new prototypes at 5 and 30 r/min. The currents are $i_d = 1$ A and $i_q = 1.5$ A, corresponding to the rated current density of 10 A/mm^2. The copper loss is dominant since the maximum speed of the prototypes is as low as 30 r/min. When the rotor speed increases, the torque decreases, and the mechanical and iron losses increase. Due to the higher transmission ratio, Prototype 3 has a higher current frequency at the same rotor speed. Thus, the iron loss of Prototype 3 is slightly higher. At 30 r/min and 10 A/mm^2, the actuator efficiencies of the two prototypes are 26.8% and 28.2%, respectively.

The thermal characteristics of the new prototypes are investigated by measuring the winding and PM temperatures using thermocouples. Since the electromagnetic parts of Prototype 2 and Prototype 3 are identical, only the thermal test of Prototype 2 is conducted. Tab. 4.3 lists the measured temperatures at 10, 20 and 40 A/mm^2. It is noteworthy that the prototype is air-cooled with a room temperature of 20 °C. After a 30-minute operation at the rated current density of 10 A/mm^2, the winding and PM temperatures reach the steady-state values of 70.8 °C and 45.1 °C, respectively. When the prototype is overloaded at 20 A/mm^2 for 1 minute, the maximum winding and PM temperatures are 74.1 °C and 34.5 °C, respectively. Furthermore, the maximum winding

Tab. 4.3: Measured temperatures of windings and PMs.

Current density [A/mm^2]	10	20	40
Operation time [s]	1800	60	10
Maximum winding temperature [°C]	70.8	74.1	76.5
Maximum PM temperature [°C]	45.1	34.5	36.3

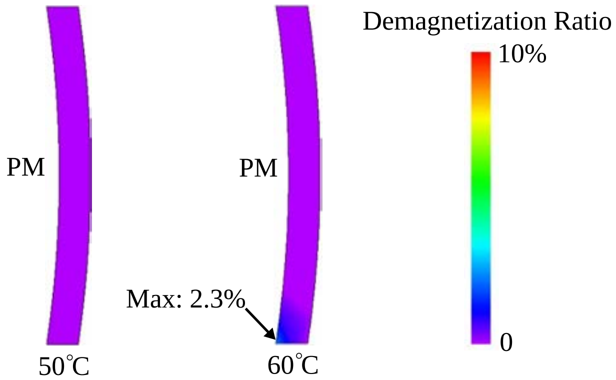

Fig. 4.18: FEA results of the irreversible demagnetization ratio of the PM at 40 A/mm^2.

and PM temperatures are 76.5 °C and 36.3 °C, respectively, after an operation of 10 seconds at the peak current density of 40 A/mm^2. The temperature limit of the AIW copper wires is 220 °C, which is high enough for the aforementioned operation conditions. Meanwhile, the temperature limit of the PMs depends on the demagnetization condition. In the two new prototypes, the PMs are made of N48H and have a thickness of 1 mm. Fig. 4.18 shows the FEA results of the irreversible demagnetization ratio on the PM at the current density of 40 A/mm^2. The demagnetization ratio is defined as the amount of variation in the residual flux density of the PM. The irreversible demagnetization occurs around one corner of the PM when the PM temperature is 60 °C. The operating conditions shown in Tab. 4.3 are permissible since the PM temperatures do not go beyond 60 °C. However, if the actuator needs to be periodically overloaded, the overloaded operation time should be limited.

4.5 Summary

This chapter presents the torque density improvement of the swirling actuator. The electromagnetic radial force is enhanced by reducing the effective air-gap length. As for the gears, the pressure angle is reduced and the transmission ratio is raised. The analyses of the gear efficiency and torque are presented. The effectiveness of the design improvements are verified by experiments. The peak torque density is significantly raised to 64 Nm/L.

Chapter 5

Conclusion

This thesis presents a study of a novel low-speed high-torque swirling actuator. It utilize the electromagnetic radial force to generate the output torque through integrated mechanical gears. The developed model has a 12-slot stator, a 12-pole SPM-structure swirler and involute-type gears. The electromagnetic radial force between the stator and swirler is analyzed and verified by 3-D FEA and experiments. A preliminary prototype with the transmission ratio of 113 was built and the peak torque density is 27 Nm/L.

To raise the torque density, first, the electromagnetic radial force is enhanced by using thin PMs and reducing the nominal air-gap length. Second, the performance of the gears is improved by reducing the pressure angle to 20° and increase the transmission ratio to 150. The efficiency and strength of the developed gears are analyzed. New prototypes were built and the peak torque density reach a notable value of 64 Nm/L.

The essential high-gear-ratio characteristic of the proposed swirling actuator make it suitable for robotic joints and other low-speed high-torque applications. The existing issue of the swirling actuator is that the mechanical power provided by the circular motion with a small eccentric radius is essentially low. Thus, the swirling actuator is not a good choice for high-power applications.

In the developed model, the mechanical gears are integrated in the radial direction, which lead to a flat structure. Meanwhile, if the gears are integrated in the axial direction, there will be more choices for the electromagnetic topology. For example, the spoke-type swirler will become feasible. The axial length of the gears can also be adjusted based on the strength requirement instead of the stack length of the electromagnetic part. Moreover, with the pins guiding the circular motion, the actual eccentric radius is shorter than the nominal value. The crankshaft structure introduced in other cycloidal machines can fix the eccentric radius to the nominal value, but the mechanical structure and assembly may become more complicated and cumbersome. Another possible topic of the proposed swirling actuator is to evaluate the performance criteria related to robotic applications, such as the backlash and the backdrivability.

Finally, the proposed swirling actuator is an example of the low-speed high-torque machine that integrates the electric machine and mechanical speed reducer. This research may motivate more novel proposals for this kind of integrated machine.

References

[1] J. W. Finch and D. Giaouris, “Controlled ac electrical drives,” *IEEE Transactions on Industrial Electronics*, vol. 55, no. 2, pp. 481–491, 2008.

[2] J. Z. Bird, “A review of electric aircraft drivetrain motor technology,” *IEEE Transactions on Magnetics*, vol. 58, no. 2, pp. 1–8, 2022.

[3] A. Penzkofer, G. Cooke, M. Odavic, and K. Atallah, “Coil excited pseudo direct drive electrical machines,” *IEEE Transactions on Magnetics*, vol. 53, no. 1, pp. 1–11, 2017.

[4] Magnomatics Ltd., “Pseudo Direct Drive Traction Motor,” 2021. [Online]. Available: https://www.magnomatics.com/pdd-traction-motor

[5] Y. E. Corporation, “MOTOMAN-HC10DTP,” 2021. [Online]. Available: https://www.e-mechatronics.com/product/robot/assembly/lineup/hc10dt/spec.html

[6] maxon, “maxon EC motor,” 2021. [Online]. Available: https://www.maxongroup.com/maxon/view/category

[7] M. Park, J.-H. Jeong, J.-H. Ryu, H.-W. Lee, and N. Park, “Development of speed reducer with planocentric involute gearing mechanism,” *Journal of Mechanical Science and Technology*, vol. 21, pp. 1172–1177, 08 2007.

[8] Nabtesco Corporation, “Introduction of RV reduction gear,” 2022. [Online]. Available: https://precision.nabtesco.com/en/products/introduction/

[9] Harmonic Drive LLC, “Strain Wave Gear Principle,” 2021. [Online]. Available: https://www.harmonicdrive.net/technology

[10] ——, "Reducer Catalog: CSF-mini," 2021. [Online]. Available: https://www.harmonicdrive.net/_hd/content/documents/CSF-Mini_GearUnits.pdf

[11] H. Matsuki, K. Nagano, and Y. Fujimoto, "Bilateral drive gear—a highly backdrivable reduction gearbox for robotic actuators," *IEEE/ASME Transactions on Mechatronics*, vol. 24, no. 6, pp. 2661–2673, 2019.

[12] K. Atallah and D. Howe, "A novel high-performance magnetic gear," *IEEE Transactions on Magnetics*, vol. 37, no. 4, pp. 2844–2846, 2001.

[13] Y. Wang, M. Filippini, N. Bianchi, and P. Alotto, "A review on magnetic gears: Topologies, computational models, and design aspects," *IEEE Transactions on Industry Applications*, vol. 55, no. 5, pp. 4557–4566, 2019.

[14] T. Ishida and A. Takanishi, "A robot actuator development with high backdrivability," in *2006 IEEE Conference on Robotics, Automation and Mechatronics*, 2006, pp. 1–6.

[15] A. M. EL-Refaie, "Fractional-slot concentrated-windings synchronous permanent magnet machines: Opportunities and challenges," *IEEE Transactions on Industrial Electronics*, vol. 57, no. 1, pp. 107–121, 2010.

[16] A. Toba and T. Lipo, "Generic torque-maximizing design methodology of surface permanent-magnet vernier machine," *IEEE Transactions on Industry Applications*, vol. 36, no. 6, pp. 1539–1546, 2000.

[17] K. Atallah, J. Rens, S. Mezani, and D. Howe, "A novel pseudo direct-drive brushless permanent magnet machine," *IEEE Transactions on Magnetics*, vol. 44, no. 11, pp. 4349–4352, 2008.

[18] A. Hughes and B. Drury, *Electric motors and drives: fundamentals, types and applications.* Newnes, 2019.

[19] A. Chiba, T. Fukao, O. Ichikawa, M. Oshima, M. Takemoto, and D. G. Dorrell, *Magnetic bearings and bearingless drives.* Elsevier, 2005.

[20] Z. Liu, A. Chiba, Y. Irino, and Y. Nakazawa, "Optimum pole number combination of a buried permanent magnet bearingless motor and test results at an output of 60 kw with a speed of 37000 r/min," *IEEE Open Journal of Industry Applications*, vol. 1, pp. 33–41, 2020.

[21] J. Amemiya, A. Chiba, D. Dorrell, and T. Fukao, "Basic characteristics of a consequent-pole-type bearingless motor," *IEEE Transactions on Magnetics*, vol. 41, no. 1, pp. 82–89, 2005.

[22] T. Srichiangsa, H. Sugimoto, Y. Fujii, and A. Chiba, "Design, development, and experimental results of a 30 000-r/min one-axis actively positioned single-drive bearingless motor," *IEEE Transactions on Industry Applications*, vol. 57, no. 6, pp. 6783–6791, 2021.

[23] L. Chen, R. Hoshi, A. Chiba, M. Nagano, and K. Nakamura, "Principle of a radial-foree-based electromagnetic swirling actuator for low-speed applications," in *2018 IEEE Energy Conversion Congress and Exposition (ECCE)*, 2018, pp. 736–743.

[24] S. O. Schrade, K. Dätwyler, M. Stücheli, K. Studer, D.-A. Türk, M. Meboldt, R. Gassert, and O. Lambercy, "Development of varileg, an exoskeleton with variable stiffness actuation: first results and user evaluation from the cybathlon 2016," *Journal of NeuroEngineering and Rehabilitation*, vol. 15, no. 18, 2018.

[25] Y. E. Corporation, "Sigma-7 ac servo drives and motors technical supplement," 2021. [Online]. Available: https://www.e-mechatronics.com/download/datas/catalog/kajps80000123/kajps80000123s_21_0.pdf

[26] A. Chiba, K. Kiyota, N. Hoshi, M. Takemoto, and S. Ogasawara, "Development of a rare-earth-free sr motor with high torque density for hybrid vehicles," *IEEE Transactions on Energy Conversion*, vol. 30, no. 1, pp. 175–182, 2015.

[27] D. Li, R. Qu, J. Li, L. Xiao, L. Wu, and W. Xu, "Analysis of torque capability and quality in vernier permanent-magnet machines," *IEEE Transactions on Industry Applications*, vol. 52, no. 1, pp. 125–135, 2016.

[28] K. Okada, N. Niguchi, and K. Hirata, “Analysis of a vernier motor with concentrated windings,” *IEEE Transactions on Magnetics*, vol. 49, no. 5, pp. 2241–2244, 2013.

[29] T. Zou, D. Li, R. Qu, D. Jiang, and J. Li, “Advanced high torque density pm vernier machine with multiple working harmonics,” *IEEE Transactions on Industry Applications*, vol. 53, no. 6, pp. 5295–5304, 2017.

[30] L. Fang, D. Li, X. Ren, and R. Qu, “A novel permanent magnet vernier machine with coding-shaped tooth,” *IEEE Transactions on Industrial Electronics*, vol. 69, no. 6, pp. 6058–6068, 2022.

[31] A. Parsapour, M. Moallem, I. Boldea, and B. Fahimi, “High torque density double stator permanent magnet electric machine,” in *2019 IEEE International Electric Machines & Drives Conference (IEMDC)*, 2019, pp. 664–670.

[32] B. Kim and T. A. Lipo, “Analysis of a pm vernier motor with spoke structure,” *IEEE Transactions on Industry Applications*, vol. 52, no. 1, pp. 217–225, 2016.

[33] D. Li, R. Qu, and T. A. Lipo, “High-power-factor vernier permanent-magnet machines,” *IEEE Transactions on Industry Applications*, vol. 50, no. 6, pp. 3664–3674, 2014.

[34] Z. S. Du and T. A. Lipo, “Torque performance comparison between a ferrite magnet vernier motor and an industrial interior permanent magnet machine,” *IEEE Transactions on Industry Applications*, vol. 53, no. 3, pp. 2088–2097, 2017.

[35] F. Zhao, T. A. Lipo, and B.-I. Kwon, “A novel dual-stator axial-flux spoke-type permanent magnet vernier machine for direct-drive applications,” *IEEE Transactions on Magnetics*, vol. 50, no. 11, pp. 1–4, 2014.

[36] R. Zhang, J. Li, R. Qu, and D. Li, “Analysis and design of triple-rotor axial-flux spoke-array vernier permanent magnet machines,” *IEEE Transactions on Industry Applications*, vol. 54, no. 1, pp. 244–253, 2018.

[37] L. Zhou, F. Guo, H. Wang, and B. Wang, “High-torque direct-drive machine with combined axial- and radial-flux out-runner vernier permanent magnet motor,” in

2021 IEEE International Electric Machines & Drives Conference (IEMDC), 2021, pp. 1–8.

[38] L. Xu, W. Zhao, G. Liu, and C. Song, "Design optimization of a spoke-type permanent-magnet vernier machine for torque density and power factor improvement," *IEEE Transactions on Vehicular Technology*, vol. 68, no. 4, pp. 3446–3456, 2019.

[39] D. Li, R. Qu, J. Li, and W. Xu, "Consequent-pole toroidal-winding outer-rotor vernier permanent-magnet machines," *IEEE Transactions on Industry Applications*, vol. 51, no. 6, pp. 4470–4481, 2015.

[40] Y. Zhang, D. Li, P. Yan, X. Ren, R. Qu, and J. Ma, "A high torque density claw-pole permanent-magnets vernier machine," *IEEE Journal of Emerging and Selected Topics in Power Electronics*, vol. 10, no. 2, pp. 1756–1765, 2022.

[41] K. Xie, D. Li, R. Qu, and Y. Gao, "A novel permanent magnet vernier machine with halbach array magnets in stator slot opening," *IEEE Transactions on Magnetics*, vol. 53, no. 6, pp. 1–5, 2017.

[42] A. Allahyari and H. Torkaman, "A novel high-performance consequent pole dual rotor permanent magnet vernier machine," *IEEE Transactions on Energy Conversion*, vol. 35, no. 3, pp. 1238–1246, 2020.

[43] S. Jia, K. Yan, D. Liang, R. Qu, J. Liu, and J. He, "A novel dc-biased current dual pm vernier machine," *IEEE Transactions on Industry Applications*, vol. 57, no. 5, pp. 4595–4605, 2021.

[44] Y. Gao, M. Doppelbauer, J. Ou, and R. Qu, "Design of a double-side flux modulation permanent magnet machine for servo application," *IEEE Journal of Emerging and Selected Topics in Power Electronics*, pp. 1–1, 2021.

[45] Y. Gao, M. Doppelbauer, R. Qu, D. Li, and H. Ding, "Synthesis of a flux modulation machine with permanent magnets on both stator and rotor," *IEEE Transactions on Industry Applications*, vol. 57, no. 1, pp. 294–305, 2021.

[46] Y. Gao, T. Kosaka, Y. Liu, M. Doppelbauer, and R. Qu, “Comparative analysis of double flux modulation permanent magnet machines with different stator pm arrangements,” *IEEE Transactions on Industry Applications*, vol. 58, no. 2, pp. 1941–1951, 2022.

[47] H. Yang, H. Lin, Z. Q. Zhu, K. Guo, D. Wang, S. Fang, and Y. Huang, “Flux-concentrated external-rotor switched flux memory machines for direct-drive applications,” *IEEE Transactions on Applied Superconductivity*, vol. 26, no. 7, pp. 1–6, 2016.

[48] H. Liu, H. Lin, S. Fang, and Z. Q. Zhu, “Permanent magnet demagnetization physics of a variable flux memory motor,” *IEEE Transactions on Magnetics*, vol. 45, no. 10, pp. 4736–4739, 2009.

[49] H. Liu, H. Lin, Z. Q. Zhu, M. Huang, and P. Jin, “Permanent magnet remagnetizing physics of a variable flux memory motor,” *IEEE Transactions on Magnetics*, vol. 46, no. 6, pp. 1679–1682, 2010.

[50] J. Liang, A. Parsapour, E. Cosoroaba, M. Wu, I. Boldea, and B. Fahimi, “A high torque density outer rotor claw pole stator permanent magnet synchronous motor,” in *2018 IEEE Transportation Electrification Conference and Expo (ITEC)*, 2018, pp. 389–393.

[51] M. Alibeik, O. N. M. Nezamuddin, R. M. Bagwe, M. J. Rubin, and E. Cipriano dos Santos, “Airgapless electric motors with an external rotor,” *IEEE Transactions on Industrial Electronics*, vol. 65, no. 9, pp. 6923–6935, 2018.

[52] A. Fatemi and D. Lahr, “A comparative study of cycloidal reluctance machine and switched reluctance machine,” *IEEE Transactions on Energy Conversion*, vol. 36, no. 3, pp. 1852–1860, 2021.

[53] K. Atallah, S. Calverley, and D. Howe, “Design, analysis and realisation of a high-performance magnetic gear,” *Electric Power Applications, IEE Proceedings -*, vol. 151, pp. 135 – 143, 04 2004.

[54] P. Rasmussen, T. Andersen, F. Jorgensen, and O. Nielsen, “Development of a high-performance magnetic gear,” *IEEE Transactions on Industry Applications*, vol. 41, no. 3, pp. 764–770, 2005.

[55] L. Jian, K. T. Chau, Y. Gong, J. Z. Jiang, C. Yu, and W. Li, “Comparison of coaxial magnetic gears with different topologies,” *IEEE Transactions on Magnetics*, vol. 45, no. 10, pp. 4526–4529, 2009.

[56] K. K. Uppalapati, M. D. Calvin, J. D. Wright, J. Pitchard, W. B. Williams, and J. Z. Bird, “A magnetic gearbox with an active region torque density of 239 n·m/l,” *IEEE Transactions on Industry Applications*, vol. 54, no. 2, pp. 1331–1338, 2018.

[57] L. Jing, T. Wang, Y. Pan, C. Tan, and R. Qu, “Optimization of dual-flux-modulator magnetic gear with hts bulks and uneven segment based on ga,” *IEEE Transactions on Applied Superconductivity*, vol. 32, no. 6, pp. 1–5, 2022.

[58] M. C. Gardner, M. Johnson, and H. A. Toliyat, “Comparison of surface permanent magnet axial and radial flux coaxial magnetic gears,” *IEEE Transactions on Energy Conversion*, vol. 33, no. 4, pp. 2250–2259, 2018.

[59] X. Yin, P.-D. Pfister, and Y. Fang, “A novel magnetic gear: Toward a higher torque density,” *IEEE Transactions on Magnetics*, vol. 51, no. 11, pp. 1–4, 2015.

[60] M. Johnson, M. C. Gardner, and H. A. Toliyat, “Design comparison of ndfeb and ferrite radial flux surface permanent magnet coaxial magnetic gears,” *IEEE Transactions on Industry Applications*, vol. 54, no. 2, pp. 1254–1263, 2018.

[61] K. Aiso, K. Akatsu, and Y. Aoyama, “A novel reluctance magnetic gear for high-speed motor,” *IEEE Transactions on Industry Applications*, vol. 55, no. 3, pp. 2690–2699, 2019.

[62] M. C. Gardner, M. Johnson, and H. A. Toliyat, “Comparison of surface permanent magnet coaxial and cycloidal radial flux magnetic gears,” in *2018 IEEE Energy Conversion Congress and Exposition (ECCE)*, 2018, pp. 5005–5012.

[63] ——, “Analysis of high gear ratio capabilities for single-stage, series multistage, and compound differential coaxial magnetic gears,” *IEEE Transactions on Energy Conversion*, vol. 34, no. 2, pp. 665–672, 2019.

[64] E. Lee, H. Song, J. Jeong, and S. Jeong, “Mechanical variable magnetic gear transmission: Concept and preliminary research,” *IEEE Robotics and Automation Letters*, vol. 7, no. 2, pp. 3357–3364, 2022.

[65] G. Jungmayr, E. Marth, and G. Segon, “Magnetic-geared motor in side-by-side arrangement - concept and design,” in *2019 IEEE International Electric Machines Drives Conference (IEMDC)*, 2019, pp. 847–853.

[66] E. Marth, G. Jungmayr, W. Amrhein, and F. Jeske, “Magnetic-geared motor in side-by-side arrangement - optimization,” in *2019 IEEE International Electric Machines Drives Conference (IEMDC)*, 2019, pp. 839–846.

[67] G. Cooke, R.-S. Dragan, R. Barrett, D. J. Powell, S. Graham, and K. Atallah, “Magnetically geared propulsion motor for subsea remote operated vehicle,” *IEEE Transactions on Magnetics*, vol. 58, no. 2, pp. 1–5, 2022.

[68] K. T. Chau, D. Zhang, J. Z. Jiang, C. Liu, and Y. Zhang, “Design of a magnetic-geared outer-rotor permanent-magnet brushless motor for electric vehicles,” *IEEE Transactions on Magnetics*, vol. 43, no. 6, pp. 2504–2506, 2007.

[69] L. Jing, W. Tang, T. Wang, T. Ben, and R. Qu, “Performance analysis of magnetically geared permanent magnet brushless motor for hybrid electric vehicles,” *IEEE Transactions on Transportation Electrification*, vol. 8, no. 2, pp. 2874–2883, 2022.

[70] K. Ito, T. Kadomatsu, and K. Nakamura, “Efficiency improvement of in-wheel magnetic geared motor and feasibility study for walking support machines,” in *2019 IEEE International Electric Machines & Drives Conference (IEMDC)*, 2019, pp. 1818–1823.

[71] K. Ito and K. Nakamura, “Investigation of magnetic interaction of ipm-type magnetic-geared motor,” *IEEE Transactions on Magnetics*, vol. 57, no. 2, pp. 1–5, 2021.

[72] M. Johnson, M. C. Gardner, and H. A. Toliyat, “Design and analysis of an axial flux magnetically geared generator,” *IEEE Transactions on Industry Applications*, vol. 53, no. 1, pp. 97–105, 2017.

[73] Magnomatics Ltd., “Pseudo Direct Drive Floating Tethered Marine Current (FTMC) Turbine,” 2021. [Online]. Available: https://www.magnomatics.com/pdd-marine-turbine

[74] ——, “Pseudo Direct Drive Aerospace Actuator,” 2021. [Online]. Available: https://www.magnomatics.com/pdd-aerospace-actuator

[75] H. Zhao, C. Liu, Z. Dong, R. Huang, and X. Li, “Design and optimization of a magnetic-geared direct-drive machine with v-shaped permanent magnets for ship propulsion,” *IEEE Transactions on Transportation Electrification*, vol. 8, no. 2, pp. 1619–1633, 2022.

[76] H. Huang, D. Li, W. Kong, and R. Qu, “Torque performance of pseudo direct-drive machine with halbach consequent pole,” in *2018 IEEE Energy Conversion Congress and Exposition (ECCE)*, 2018, pp. 3286–3293.

[77] X. Yin, Y. Fang, X. Huang, and P.-D. Pfister, “Analytical modeling of a novel vernier pseudo-direct-drive permanent-magnet machine,” *IEEE Transactions on Magnetics*, vol. 53, no. 6, pp. 1–4, 2017.

[78] Q. Gan, Y. Fang, and P.-D. Pfister, “A novel concentrated-winding vernier pseudo-direct-drive permanent-magnet machine,” *IEEE Transactions on Magnetics*, vol. 58, no. 2, pp. 1–5, 2022.

[79] F. T. Jorgensen, T. O. Andersen, and P. O. Rasmussen, “The cycloid permanent magnetic gear,” *IEEE Transactions on Industry Applications*, vol. 44, no. 6, pp. 1659–1665, 2008.

[80] K. Li, J. Bird, J. Kadel, and W. Williams, “A flux-focusing cycloidal magnetic gearbox,” *IEEE Transactions on Magnetics*, vol. 51, no. 11, pp. 1–4, 2015.

[81] K. Davey, L. McDonald, and T. Hutson, "Axial flux cycloidal magnetic gears," *IEEE Transactions on Magnetics*, vol. 50, no. 4, pp. 1–7, 2014.

[82] H. Huang, R. Qu, and J. Bird, "Performance of halbach cycloidal magnetic gears with respect to torque density and gear ratio," in *2019 IEEE International Electric Machines & Drives Conference (IEMDC)*, 2019, pp. 1977–1984.

[83] H. Huang, J. Z. Bird, A. L. Vera, and R. Qu, "An axial cycloidal magnetic gear that minimizes the unbalanced radial force," *IEEE Transactions on Magnetics*, vol. 56, no. 7, pp. 1–10, 2020.

[84] J. Rens, K. Atallah, S. D. Calverley, and D. Howe, "A novel magnetic harmonic gear," *IEEE Transactions on Industry Applications*, vol. 46, no. 1, pp. 206–212, 2010.

[85] O. Molokanov, P. Dergachev, S. Osipkin, E. Kuznetsova, and P. Kurbatov, "A novel double-rotor planetary magnetic gear," *IEEE Transactions on Magnetics*, vol. 54, no. 11, pp. 1–5, 2018.

[86] Harmonic Drive LLC, "FLA Rotary Actuator," 2021. [Online]. Available: https://www.harmonicdrive.net/products/rotary-actuators/solid-shaft-actuators/fla

[87] Nabtesco Corporation, "Actuator af," 2022. [Online]. Available: https://precision.nabtesco.com/ja/products/detail/AF-N

[88] D. Hwang and T. Higuchi, "A planar wobble motor with a xy compliant mechanism driven by shape memory alloy," *IEEE/ASME Transactions on Mechatronics*, vol. 21, no. 1, pp. 302–315, 2016.

[89] D. Hwang, Y. S. Ihn, and K. Kim, "Compact modular cycloidal motor with embedded shape memory alloy wires," *IEEE Transactions on Industrial Electronics*, vol. 65, no. 5, pp. 4028–4038, 2018.

[90] Y. Kadota, K. Inoue, K. Uzuka, H. Suenaga, and T. Morita, "Noncontact operation of a miniature cycloid motor by magnetic force," *IEEE/ASME Transactions on Mechatronics*, vol. 18, no. 5, pp. 1563–1571, 2013.

[91] Z. Q. Zhu, D. Ishak, D. Howe, and J. Chen, “Unbalanced magnetic forces in permanent-magnet brushless machines with diametrically asymmetric phase windings,” *IEEE Transactions on Industry Applications*, vol. 43, no. 6, pp. 1544–1553, 2007.

[92] J. Asama, A. Mouri, T. Oiwa, and A. Chiba, “Suspension force investigation for consequent-pole and surface-mounted permanent magnet bearingless motors with concentrated winding,” in *2015 IEEE International Electric Machines & Drives Conference (IEMDC)*, 2015, pp. 780–785.

[93] D. T. Jelaska, *Gears and gear drives.* John Wiley & Sons, 2012.

List of Publications

Journal Publications

1. L. Chen, A. Thabuis, Y. Fujii, A. Chiba, M. Nagano and K. Nakamura, ”Principle and Analysis of Radial-Force-Based Swirling Actuator for Low-Speed High-Torque Applications,” in *IEEE Transactions on Industry Applications*, vol. 58, no. 2, pp. 1963-1975, March-April 2022, doi: 10.1109/TIA.2022.3142118.
   (Chapter 3) Published.

2. L. Chen, Y. Fujii and A. Chiba, ”Torque Density Improvement of a Low-Speed High-Torque Swirling Actuator Driven by Electromagnetic Radial Force With Integrated Mechanical Gears,” in *IEEE Open Journal of Industry Applications*, vol. 4, pp. 11-22, 2023, doi: 10.1109/OJIA.2022.3232119.
   (Chapter 4) Published.

International Conference Publications

1. L. Chen, R. Hoshi, A. Chiba, M. Nagano and K. Nakamura, ”Principle of a Radial-Force-Based Electromagnetic Swirling Actuator for Low-Speed Applications,” 2018 IEEE Energy Conversion Congress and Exposition (ECCE), Portland, OR, USA, 2018, pp. 736-743, doi: 10.1109/ECCE.2018.8558086.

2. L. Chen, A. Thabuis, A. Chiba, M. Nagano and K. Nakamura, ”Radial- Force-Based Swirling Actuator with Surface-Permanent-Magnet Structure for Low-Speed High-Torque Applications,” 2019 IEEE Energy Conversion Congress and Exposition (ECCE), 2019, pp. 6106-6113, doi: 10.1109/ECCE.2019.8912163.

Domestic Conference Publications

1. L. Chen, A. Chiba, M. Nagano and K. Nakamura, “Principle of a Radial-force-based Swirling Actuator with SPM Structure,” 平成31年電気学会全国大会.
2. L. Chen, A. Chiba, M. Nagano and K. Nakamura, “Analysis of an Electromagnetic-Radial-force-based Swirling Actuator without Permanent Magnets,” 令和2年電気学会全国大会.
3. L. Chen and A. Chiba, “Measurement of Electromagnetic Radial Force of a Swirling Actuator with SPM Structure,” 令和3年電気学会全国大会.
4. L. Chen and Y. Fujii and A. Chiba, “Torque Improvement of a Low-Speed High-Torque Swirling Actuator with Integrated Mechanical Gears,” 令和4年電気学会全国大会.
   (優秀論文発表賞)